SOLAR IRRADIANCE FORECASTING FOR TROPICAL REGIONS USING NOVEL STATISTICAL ANALYSIS AND MACHINE LEARNING

DONG ZIBO

(B.Eng.(Hons.), NUS)

A THISIS SUBMITTED

FOR THE DEGREE OF DOCTOR OF PHILOSOPHY

DEPARTMENT OF ELECTRICAL AND COMPUTER ENGINEERING

NATIONAL UNIVERSITY OF SINGAPORE

2016

Declaration

I hereby declare that this thesis is my original work and it has been written by me in its entirety. I have duly acknowledged all the sources of information which have been used in the thesis.

This thesis has also not been submitted for any degree in any university previously.

Dong Zibo
13 May 2016

Acknowledgements

My sincere thanks go to Prof. Armin Aberle, Dr. Thomas Reindl and Dr. Wilfred Walsh for offering me the opportunity to study in the university and facilitating all administrative matters.

I would also like to thank my friends in the labs, Dr. Yang Dazhi, Dr. Ye Zhen, Dr. Gu Chaojun, Dr. Khoo Yong Sheng and Dr. Andre Nobre for their support; and Assist. Prof. Chen Nan and Assist. Prof. Panida Jirutitijaroen for their advice on specific topics.

Summary

Solar photovoltaics (PV) is set to become one of the major energy sources of the future, tapping into the virtually endless supply of energy from the sun. The actual power output of a solar PV system can vary substantially, depending on the local irradiation conditions and the system performance, making it a variable type of renewable energy with high variability. Since more than 90% of the installed PV systems worldwide are grid-connected, this in turn raises concerns among grid operators regarding the influence of photovoltaic power on the performance of their electricity grid.

To minimize the risk of destabilizing the electricity grid by a sizeable share of solar PV, it is indispensable to forecast the contribution of solar power ahead of time, by 5 minutes, 1 hour, or 1 day in advance depending on the needs of the grid operation. This would allow the grid operator to take suitable grid management measures, such as up- or downscaling of the power output of other, adjustable generation capacities, demand-side management, especially looking ahead into future smart-grids, or forward buying at the electricity exchange at lower rates. Solar power forecasting requires forecasting of irradiance at a spatial resolution customized for the relevant grid area as the major input parameter, and modelling of solar power systems in the same grid area, unless the actual locations of the PV units can be used to get reliable forecast values with high accuracy.

However, the forecasting is particularly challenging in the tropics due to high solar irradiance variability. The primary goal of this thesis therefore is to develop novel, robust irradiance forecasting models for application in the tropics. Several novel models based on statistical time series analysis and machine learning techniques are proposed and investigated, including a short-term exponential smoothing state space (ESSS) model, mid-term hybrid models (artificial neural network (ANN) with ESSS model, self-organising maps (SOM), support vector regression (SVR) with particle swarm optimization (PSO)) and a spatial-temporal analysis. Superior forecasting accuracy is achieved by the proposed models and forecasting at arbitrary locations can be performed with high spatial resolution data.

List of publications

Journal papers

- **Zibo Dong**, Dazhi Yang, Thomas Reindl and Wilfred M. Walsh. “Short-term solar irradiance forecasting using exponential smoothing state space model", Energy 2013; 55:1104–1113. (Impact factor: 4.844)

- **Zibo Dong**, Dazhi Yang, Thomas Reindl and Wilfred M. Walsh. “Satellite image analysis and a hybrid ESSS/ANN model to forecast solar irradiance in the tropics", Energy Conversion and Management 2014; 79:66–73. (Impact factor: 4.380)

- **Zibo Dong**, Dazhi Yang, Thomas Reindl and Wilfred M. Walsh. “A novel hybrid approach based on self-organizing maps, support vector regression and particle swarm optimization to forecast solar irradiance", Energy 2015; 82:570–577. (Impact factor: 4.844)

- Dazhi Yang, Chaojun Gu, **Zibo Dong**, Panida Jirutitijaroen, Chen Nan and Wilfred M. Walsh. “Solar irradiance forecasting using spatial-temporal covariance structures and time-forward kriging", Renewable Energy 2013; 60:235–245. (Impact factor: 3.476)

- Dazhi Yang, **Zibo Dong**, Andre Nobre, Khoo Yong Sheng, Panida Jirutitijaroen and Wilfred M. Walsh. “Evaluation of transposition and decomposition models for converting global solar irradiance from tilted surface to horizontal in tropical regions", Solar Energy 2013; 97:369–387. (Impact factor: 3.469)

- Dazhi Yang, **Zibo Dong**, Thomas Reindl, Panida Jirutitijaroen and Wilfred M. Walsh. “Solar irradiance forecasting using spatio-temporal empirical kriging and vector autoregressive models with parameter shrinkage", Solar Energy 2014; 103:550–562. (Impact factor: 3.469)
- Dazhi Yang, Zhen Ye, Lihong Idris Lim, and **Zibo Dong**.“Very short term irradiance forecasting using the lasso", Solar Energy 2015; 114:314–326. (Impact factor: 3.469)

Conference papers

- Yang Dazhi, Wilfred M. Walsh, **Dong Zibo**, Panida Jirutitijaroen and Thomas Reindl. “Block Matching Algorithms: Their Applications and Limitations in Solar Irradiance Forecasting", PV Asia Pacific Expo & Conference 2013, Energy Procedia 2013: 33:335–342.

Contents

List of Figures

List of Tables

Nomenclature

Roman Symbols

a, b, c	Model parameters	-
A_t, B_t, C_t, D_t, E_t	Component functions in the ESSS model	-
B	$B = (n-1)\frac{360}{365}$ in section 2.1.1; backward operator in section 2.2.1.3	-
b	Bias in section 5.2.2	-
b_i	Bias	-
b_t	Same as g_t in the ESSS model	-
C	Trade-off coefficient	-
c_1,c_2	Acceleration constants in section 5.2.3	-
D	Day number	-
d	Peak irradiance hour of the day (W/m^2); number of differencing passes in section 2.2.1.3	-
$d(n)$	Desired output value in section 4.2.2.1	-
$d_{i,j}^2$	Euclidean distance from i to j; spatial dispersion from i to j in chapter 6	-

D_p	Diameter of a particle	m
e_t	$e_t = k(x_{t-1})\epsilon_t$	-
E_0	Eccentricity of the Earth's orbit	-
E_Δ	Incident solar irradiance within the spectral band of the satellite radiometer	W/m^2
E_a	Solar radiation absorbed at the atmosphere	W/m^2
$E_{j,O(x)}(t)$	Measure of the effectiveness of the $O(x)$ on its neighbours	-
E_t	Solar radiation absorbed at the earth surface	W/m^2
$f(n)$	Function of n	-
f_i	Number i peak frequency	Hz
$f_i()$	Function at i's hidden neuron	-
$g()$	Function of present stress in chapter 6	-
$g(\mathbf{x}_i)$	Target function $g(\mathbf{x}_i) = \mathbf{w}^T\mathbf{x}_i + b$ in section 5.2.2	-
G_{on}	Radiation on a plane normal to the incidence outside the atmosphere on the nth day of a year from the 1st January	W/m^2
G_{SC}	Solar Constant	$1.367 \pm 1\%\, kW/m^2$
g_t	ESSS growth component at time t	-
H	$N \times n$ matrix in section 4.2.2.1	-
h	Time constant	s
$h(x), k(x), f(x), g(x)$	State space functions in the ESSS model	-

H_0	Null hypothesis	-
H_1	Alternative hypothesis	-
h_m	$h_m = [(h-1) \mod m] + 1$	-
h_{ij}	Euclidean distance from i to j in the D plane in chapter 6	-
h_{ki}	Output of the i's hidden neuron for each training sample input vector $x(k)$	-
i	Index number; neuron number for the current layer in section 4.2.2.1; location in chapter 6	-
I_t	Global irradiance on a tilted plane	W/m^2
I_{CS}	Clear sky global irradiance	W/m^2
I_{CS}	Global irradiance of clear sky	W/m^2
I_{Dif}	Diffuse horizontal irradiance	W/m^2
I_{Dir}	Direct normal irradiance	W/m^2
I_{Glo}	Global horizontal irradiance	W/m^2
I_G	Incident solar irradiation	W/m^2
$I_{measured}$	General notation for all the measured quantities	W/m^2
I_{oh}	Horizontal extraterrestrial irradiance	W/m^2
I_o	Extraterrestrial solar radiation; extraterrestrial direct normal irradiance in section 6.2	W/m^2
$I_{predicted}$	General notation for all the predicted quantities	W/m^2

I_r	Solar radiation reflected by the earth-atmosphere system	W/m^2
I_{SC}	Solar Constant	$1.367 \pm 1\% \, kW/m^2$
j	Output neuron in section 4.2.1.1 and section 5.2.1; neuron number for the previous layer in section 4.2.2.1; location in chapter 6	-
K	Number of equal sized sub-samples in section 5.2.3	-
k	Arbitrary positive integer; rank of matrix H in section 4.2.2.1; coverage factor in section 6.2	-
$K()$	Kernel function in section 5.2.2	-
k_c	Clear sky index	-
K_d	Diffuse horizontal transmittance	-
K_n	Direct normal transmittance	-
k_T/K_t	Clearness index	-
L	Maximum iteration number in section 5.2.3	-
l	Current iteration number in section 5.2.3	-
$L()$	Maximum likelihood function	-
$l()$	Loss function in section 5.2.2	-
L_Δ	Radiance within the spectral band of the satellite radiometer	$W/(sr * m^2)$
l_t	ESSS level component at time t	-
M	Arbitrary positive number	-

m	Number of seasons; number of sample data in section 5.2.3	-
N	Arbitrary positive integer	-
n	Day number of a year in section 2.1.1; cloud index in section 2.2.3; number of significant frequencies in section 3.2.1; arbitrary positive integer in section 4.2.2.1	-
$O(x)$	Best-matching neuron to input vector x	-
P	Number of parameters in θ; position points in G plan in chapter 6	-
p	Autoregressive parameter	-
q	Moving average parameter	-
r	Time series value; distance from Cartesian origin in section 6.1.3.3; arbitrary positive number in section 6.1.4.2	-
R^2	Coefficient of determination	-
R_d	Diffuse transposition factor	-
r_e	Reciprocal of the square of the Earth radius factor	-
R_r	Transposition factor for ground reflection	-
R_t	Forecasted time series for r_t	-
r_{ij}	Euclidean norm between two points in chapter 6	-
r_{t+h}	Time series value at future time $t+h$	-
r_t	Trend irradiance at irradiance t	W/m^2
S	Space in chapter 6	-

s	Layer number in section 4.2.2.1; tilt degrees in section 6.2	-
S_M	Present stress in chapter 6	-
s_t	ESSS seasonal component at time t	-
SC	Solar Constant	$1.367 \pm 1\% \, kW/m^2$
sl	Iteration step length in chapter 6	-
T	Time in chapter 6	-
t	Time	s
T_{clear}	Sky transmittance for clear condition	-
T_{cloud}	Sky transmittance for cloudy condition	-
T_d	Downward (sun to ground) transmittance of the clear atmosphere	-
T_u	Upward (ground to sun)transmittance of the clear atmosphere	-
U	Orthogonal matrix in section 4.2.2.1	-
U_{95}	Expanded uncertainty at 95% confidence interval	-
V	Orthogonal matrix in section 4.2.2.1	-
$v(n)$	Input of transfer function in section 4.2.2.1	-
w	Weight vector; inertia weight coefficient in section 5.2.3	-
w_{max}	Maximum inertia value in section 5.2.3	-
w_{min}	Minimum inertia value in section 5.2.3	-
x	Input vector in chapter 4	-

x_t	State vector at time t in the ESSS model	-
$x_{out}(n)$	Output of transfer function in section 4.2.2.1	-
Y	Actual value in section 5.2.3	-
y_i	Output value in section 5.2.2	-
y_n	Observed time series	-
Z	Zenith Angle (°); Random field in chapter 6	-

Greek Symbols

α	Size parameter; solar elevation angle (°) in section 2.2.3.3; smoothing parameter in ESSS model; model parameter in chapter 6	-
α_i/α_i^*	Lagrange multipliers in section 5.2.2	-
β	Smoothing parameter; model parameter in chapter 6	-
χ	Velocity magnitude factor	-
Δ	Brightness index	-
$\delta(n)$	Error function; monotone function in chapter 6	-
ϵ / ε	Error term; deviation in section 5.2.2; clearness index in section 6.2	-
ϵ_t / ε_t	Error term at time t	-
$\eta(t)$	Time-varying learning parameter	-
γ	Smoothing parameter	-
λ	Wavelength of incident radiation	m
μ	Constant	-

μ_t	$\mu_t = h(x_{t-1})$	-
ν	Model parameter	-
ϕ	Damping factor; fitting coefficient in section 2.2.1.3; constant in chapter 6	-
$\Phi()$	Mapping function to high dimensional feature space	-
$\psi()$	Positive function with a completely monotone derivative	-
ρ	Surface albedo; correlation in chapter 6	-
ρ_{atm}	Atmosphere albedo	-
ρ_c	Cloud albedo	-
ρ_{eff}	Effective cloud albedo	-
ρ_g	Ground albedo	-
σ	Standard deviation; width kernel parameter in chapter 5	-
$\sigma(t)$	Time-varying effective width of the topological neighbourhood	-
σ_0	Initial effective width of the topological neighbourhood	-
τ	Time constant; time separation in chapter 6	s
τ_1	Time constant to control the decay rate of the effective width	s
τ_2	Time constant to control the decay rate of the learning rate	s
θ	Fitting coefficient; In ESSS model, $\theta = (\alpha, \beta, \gamma, \phi)$; angle (°) of incident irradiance on the tilted plane in section 6.2	-
$\varphi(x)$	Transfer function; monotone function in section 6.1.4.2	-

φ_1,φ_2	Random weights in the range $[0,1]$ under normal distribution	-
ξ/ξ^*	Slack variable; eccentric anomaly of the Earth in the orbit around the Sun in section 6.2	-
ζ	Model parameter	-
X_0	ESSS model initial states $X_0 = (l_0, g_0, s_0, s_{-1}, \ldots, s_{-m+1})$	-

Other Symbols

$\angle z$	Zenith Angle	°
$\hat{\theta}$	Estimate of θ	-
$\hat{X_0}$	Estimate of X_0	-
$\hat{y}_{t+h}$	Forecast value at time $t+h$	-
$\mathbb{C}$	Covariance function	-
$\mathbb{R}/\mathbf{R}$	Real Numbers	-
$\mathbf{c_0}$	Spatial-temporal variance-covariance matrix	-
$\mathbf{C_S}$	Spatial variance-covariance matrix	-
$\mathbf{C_T}$	Temporal variance-covariance matrix	-
cov	Covariance	-
$\mathbf{C}$	Spatial-temporal variance-covariance matrix	-
$\mathbf{h}$	Spatial separation in chapter 6	-
$\mathbf{I}$	Binary indicator function in chapter 6	-
$\mathbf{K}$	Matrix in chapter 6	-

$\mathbf{L}$	Matrix in chapter 6	-
$\mathbf{O}$	3×3 matrix of zeros in chapter 6	-
$\mathbf{P}$	Matrix in chapter 6	-
$\mathbf{s}_i$	Location in chapter 6	-
$\mathbf{V}$	Matrix in chapter 6	-
$\mathbf{v}_i$	Velocity vector in section 5.2.3	-
$\mathbf{w}$	Weight vector	-
$\mathbf{x}$	Multidimensional vector	-
$\mathbf{Y}$	Matrix in chapter 6	-
$\mathbf{y}$	Global best position vector in section 5.2.3	-
$\mathbf{y}_i$	Individual best position vector in section 5.2.3	-
$\mathbf{z}$	Observed value in Kriging	-

Acronyms/Abbreviations

ACF	Autocorrelation Function
AIC	Akaike's Information Criterion
ANN	Artificial Neural Network
AOD	Aerosol Optical Depth
AR	Autoregressive
ARIMA	Autoregressive Integrated Moving Average

ARMA	Autoregressive Moving Average
ASRC	Atmospheric Sciences Research Centre
D plane	Dispersion space
DHI	Diffuse Horizontal Irradiance
DNI	Direct Normal Irradiance
ESSS	Exponential Smoothing State Space
FT	Fitness Threshold
G plane	Geographic space
GHI	Global Horizontal Irradiance
IMA	Integrated Moving Average
IR	Infrared
ISE	Fraunhofer Institute for Solar Energy Systems
JMA	Japan Meteorological Agency
kNN	k-Nearest-Neighbours
KPSS	Kwiatkowski–Phillips–Schmidt–Shin
LES	Linear Exponential Smoothing
LMA	Levenberg-Marquardt Algorithm
LOESS	Local Regression
MA	Moving Average

MAPE	Mean Average Percentage Error
MDS	Multidimensional Scaling
MLP	Multi-layer Perceptron
MSC	Meteorological Satellite Centre
MSE	Mean Squared Error
MSG/MGS	Meteosat Second Generation
MTSAT	Multifunctional Transport Satellites
NIR	Near Infrared
nMBE	Normalized Mean Bias Error
NREL	National Renewable Energy Laboratory
nRMSE	Normalized Root Mean Square Error
OKS	Ord, Koehler and Snyder
PSO	Particle Swarm Optimization
PV	Photovoltaics
RBF	Radial Basis Functions
RW	Random Walk
SARIMA	Seasonal Autoregressive Integrated Moving Average
SERIS	Solar Energy Research Institute of Singapore
SES	Simple Exponential Smoothing

SOM	Self-organising Maps
SPA	Solar Position Algorithm
SVD	Singular Value Decomposition
SVR	Support Vector Regression
WV	Water Vapour

Chapter 1

Introduction

1.1 Background

With rapid reduction in the cost of solar photovoltaic (PV) electricity over the last ten years, and grid parity occurring in many locations, PV is set to become one of the major energy sources of the future. However, the instantaneous power output of a PV system can vary substantially, depending on local irradiance conditions and the system performance, making PV a variable form of renewable energy. Since more than 90% of the installed PV systems worldwide are grid-connected, this in turn raises concerns among grid operators regarding the influence of PV power on the stability of their electricity grids (SPE, 2015).

Considering the power rather than the energy contribution of PV in a typical electricity grid, a $5-10\%$ share of the total annual electric energy generation, as seen today in Germany, can easily correspond to more than 49% instantaneous share of the total power in the middle of the day(SPE, 2015). This may occur for example on a bright, sunny weekend day when large industrial consumers are closed.

In Singapore, future PV generation could theoretically contribute up to 20% of annual electric energy generation (National Climate Change Strategy (NCCS), 2014). To avoid the risk of destabilising the electricity grid, it will be necessary to forecast the contribution of solar power on short (minutes), medium (hours) and long (days) time scales. Forecasts allow the grid operator to implement on-the-fly grid management measures, such as up- or downscaling of the power output of other adjustable generation capacities, demand-side management, or forward buying at the electricity exchange at lower rates.

Even though there are other factors affecting the performance of PV systems, solar irradiance is the dominating factor in the forecasting of the overall PV output in grid integration.

Accurate solar irradiance forecasting is essential for many PV system level and electricity power grid level applications. Three categories of forecasting horizons are usually used: short term, medium term and long term. Short-term forecasting is defined as intra-hour forecasting. Medium-term forecasting is defined as one to six hours ahead forecasting. Long-term forecasting is defined as above six hours ahead forecasting.

The focus of this thesis is short-term forecasting and medium-term forecasting. They have very different statistical characteristics. Short-term forecasting demonstrates high time sequential correlation while medium-term forecasting does not. Five-minute forecasting is selected to represent the short-term forecasting characteristic and the result can be extended to other short-term interval forecasting. One hour interval is also typical in power scheduling and hence selected to represent the medium-term forecasting characteristics. The result can be extended to other medium-term interval forecasting.

1.2 Thesis statement

The primary goal of this thesis is to develop more accurate irradiance forecasting models for application in tropical Singapore. Novel models involving statistical time series analysis and machine learning techniques are investigated and developed to meet the specific spatial and temporal requirements of solar irradiance forecasting in the tropics.

1.3 Motivation

Solar irradiance is defined as the power per unit area of solar radiation at a surface. We are only interested in solar irradiance reaching the ground surface. The nature of solar irradiance forecasting is to make predictions of the future irradiance value based on past and present relevant data. The past relevant data are usually in the form of time series. The most widely applied method to determine patterns in the past time series data and deduce predictions for the future is the statistical time series analysis. There is a great number of models in statistical time series analysis which have been applied to various fields of studies such as economic forecasting, financial forecasting, climate forecasting, utility forecasting, census forecasting and so on. Since solar irradiance time series have specific characteristics, the traditional statistical models must be carefully modified and improved to accommodate these properties.

In Chapter 3, a novel statistical time series analysis model for solar irradiance forecasting is proposed. We forecast 5-minute solar irradiance time series based on a novel exponential smoothing state space (ESSS) model. To stationarize the irradiance data before applying linear time series models, we propose a novel Fourier trend model and compare the performance with other popular trend models using residual analysis and the Kwiatkowski-

Phillips-Schmidt-Shin (KPSS) stationarity test. Using the optimized Fourier trend, an ESSS model is implemented to forecast the stationary residual series of datasets from Singapore and Colorado, USA. To compare the performance with other time series models, autoregressive integrated moving average (ARIMA), linear exponential smoothing (LES), simple exponential smoothing (SES) and random walk (RW) models are tested using the same data. The simulation results show that the ESSS model has generally better performance than other time series forecasting models. To assess the reliability of the forecasting model in real-time applications, a complementary study of the forecasting 95% confidence interval and forecasting horizon of the ESSS model has been conducted.

In terms of analysing patterns in the past relevant data, machine learning is a powerful technique in general. The concept of machine learning is to enable computers to learn without being programmed explicitly. It has been proved to be effective in regression, classification, clustering, structured prediction and so on (Yann LeCun and Hinton, 2015). Specifically in solar irradiance forecasting, machine learning models are designed and optimized to achieve better accuracy.

In Chapter 4, a novel hybrid model including both statistical time series analysis and machine learning is proposed. We forecast hourly solar irradiance time series using satellite image analysis and a hybrid exponential smoothing state space (ESSS) model together with artificial neural networks (ANN). Since cloud cover is the major factor affecting solar irradiance, cloud detection and classification are crucial to forecast solar irradiance. Geostationary satellite images provide cloud information, allowing a cloud cover index to be derived and analysed using self-organizing maps (SOM). Owing to the stochastic nature of cloud generation in tropical regions, the ESSS model is used to forecast cloud cover index. Among different models applied in the ANN, we favour the multi-layer perceptron (MLP) to derive solar irradiance based on the cloud cover index. This hybrid model has been used to forecast hourly solar irradiance in Singapore and the technique is found to outperform traditional forecasting models.

In Chapter 5, a novel hybrid model based on machine learning is proposed. We forecast hourly solar irradiance time series using a novel hybrid model based on self-organizing maps (SOM), support vector regression (SVR) and particle swarm optimization (PSO). In order to solve the noise and stationarity problems in the statistical time series forecasting modelling process, SOM is applied to partition the whole input space into several disjointed regions with different characteristic information on the correlation between the input and the output. Then SVR is used to model each disjointed region to identify the characteristic correlation. In order to reduce the performance volatility of SVM with different parameters, PSO is implemented to automatically perform the parameter selection in SVR modelling. This hybrid model has been used to forecast hourly solar irradiance in Colorado, USA and Singapore. The technique is found to outperform traditional forecasting models.

From Chapter 3 to Chapter 5, single station solar irradiance forecasts using novel statistical analysis and machine learning have been proposed and studied. Although the accuracies of these forecasting methods can be adequate, we are also interested in the spatial irradiance information where there are no monitoring stations. In order to plan the electricity generation at the power grid level, a large number of monitoring stations over the power grid area is required. However, the number of sensors is generally limited and their distribution is irregular. Thus, spatial-temporal estimation for solar irradiance is an important step towards the forecast required by renewable energy driven cities.

In Chapter 6, a novel statistical spatial-temporal analysis is proposed. Spatial-temporal datasets that enjoy the properties of stationarity, full symmetry and separability are in general more amenable to statistical forecasting algorithms. Usually, none of these properties obtain in meteorological data such as wind velocity fields and solar irradiance distributions. In this analysis, we construct a statistical analysis system to mitigate this problem. We first achieve temporal stationarity by detrending solar irradiance time series at individual monitoring stations. We then approximate spatial stationarity through deformations of the geographic coordinates. Various spatial-temporal variance-covariance structures are formed to explore full symmetry and separability.

It is also important to know how we pre-process the solar irradiance data from all the stations to obtain the spatial-temporal datasets. Irradiance at differing geographical locations is frequently measured using sensors which are installed in the plane of existing PV arrays, whose tilt is optimized to the location. One is therefore often compelled to convert the irradiance from an arbitrary tilt to global horizontal irradiance (GHI) as would be measured on a horizontal surface. The existing literature, however, focuses on using transposition and decomposition models to predict solar irradiance on a tilted surface from solar irradiance data on a horizontal plane. In this part of the chapter, we discuss the reverse process. We use Singapore data collected at various tilts and azimuths to perform the analysis. We first evaluate the performance of various transposition and decomposition models in tropical regions. Then we further analyse constraints on each decomposition model and select an optimal model using measured GHI data as a benchmark.

Finally, Chapter 7 presents the conclusions from this work and proposed future works.

1.4 Novel contributions

In Chapter 3, the novel contribution is the proposed ESSS model with Fourier trend preprocessing to forecast short-term solar irradiance. Compared with other popular statistical time series models, the ESSS model has better forecasting accuracy in general for the forecasting horizon from 5 to 20 minutes. This timescale is one of great interest to power grid operators. Even a marginal improvement in forecasting accuracy on this timescale can represent huge cost savings in grid operation. Moreover, our novel formulation of the Fourier trend model also outperforms other similar trend models.

In Chapter 4, the novel contribution is the proposed SOM+ESSS+MLP hybrid model with satellite image preprocessing to forecast medium-term solar irradiance. Compared with other popular statistical time series models, the proposed model has superior forecasting accuracy for hourly solar irradiance.

In Chapter 5, the novel contribution is the proposed SOM+SVR+PSO hybrid model to forecast medium-term solar irradiance without satellite images. To compare the performance with other time series forecasting models, the hybrid model has generally better performance than other statistical models in hourly solar irradiance forecasting.

In Chapter 6, the novel contribution is the proposed spatial-temporal solar irradiance analysis. This analysis provides a scientific way to predict solar irradiance at locations without monitoring stations. The methodology presented here was useful when high spatial resolution irradiance data are available.

Chapter 2

Literature Review

2.1 Solar forecasting needs, market connection and stakeholders

If the world is to avoid catastrophic climate change, massive uptake of renewable energy (RE) is essential. Some RE deployment will be at the utility scale and some will take the form of 'distributed' small scale systems, for example rooftop PV. One example of this phenomenon at present is Australia, where a small number of on- and off- grid MW scale PV systems have been deployed, along with over one million kW scale systems (Simpson and Clifton, 2016). Together, these PV systems can represent a significant fraction of total energy generation in some areas. In these areas, grid management issues have already arisen, leading to occasional PV curtailment (Bahadori and Nwaoha, 2013). The Australian example shows that to mitigate grid problems caused by the inherently variable nature of most RE, modern grids must be more flexible than traditional power grids, deploying technologies including, but not limited to, monitoring, information management, storage and advanced demand and supply forecasting on a variety of time scales.

For power system operators, it is therefore important to understand the value of accurate solar energy forecasting on all time scales. The benefits of forecasting were ignored previously mainly because the RE penetration level is generally too low. With the rapid expansion of RE, particularly solar power installations, the value of forecasting must be examined by addressing the challenges in power system integration. Here we only consider solar PV forecasts.

In the middle of the day, large instantaneous solar power generation is expected to correspond a large portion of the electricity demand. Depending on local irradiance conditions and the grid topology, it is challenging, and potentially possible, for power system operators to adjust power generation to meet the downward and upward net load ramping to compensate the solar power generation. Without proper power system management, solar power must be curtailed or the power system reliability is at risk, as already seen in Australia. The curtailment is an avoidable inefficiency in the grid. Accurate solar power forecasting can effectively reduce the inefficiencies through unit commitment and economic dispatch decisions (Martinez-Anido et al., 2016).

Different power plants have various unit commitment schedules according to their start-up and shut-down timings. Some power plants like gas and oil fast turbines and internal combustion engines can be re-committed one hour ahead or less. Some power plants like gas combined cycle and gas and oil steam turbines can only be re-committed a few hours ahead. Several other power plants like nuclear and coal must be re-committed one day ahead. Solar power forecasting is essential for the commitment decisions in different time scales, with significant portion of solar power present in the system.

Economic dispatch decisions are the cost optimization of various power system operations including the unit commitment decisions. Solar power forecasting can reduce the uncertainty of solar power generation in dispatch decisions to facilitate economic and reliable power dispatch, given that other constraints in generation, transmission and load have been considered.

In California USA, the solar forecasting is primarily used by California Independent System Operators (CAISO). With greater distributed PV penetration level, utilities are also using solar forecasting for local automated response to voltage fluctuations caused by solar production (Lentz et al., 2014).

The market need for better solar power forecasting and grid integration planning tools has been widely recognized. Different time interval forecasts are used by CAISO:

- The day ahead (DA) forecast is submitted to the CAISO at 5:30 AM prior to the operating day. The forecast covers each of the 24 hours of that operating day beginning from midnight, which means the day ahead forecast provides 18.5 to 42.5 hours ahead forecast for the operating day. Most of the conventional generation is scheduled in the DA market.

- The hour ahead (HA) forecast is submitted 105 minutes prior to each operating hour. Under the CAISO Participating Intermittent Resources Program (PIRP), a participating intermittent resource can receive special settlement treatment if HA forecast is submitted by the resource's scheduling coordinator.

- The minute ahead (MA) forecast is submitted every 5 minutes according to the market period in CAISO. The Federal Energy Regulatory Commission (FERC) has issued a Notice of Proposed Rulemaking requiring public utility transmission providers to offer all customers the opportunity to schedule transmission service every 15 minutes, and requiring providers with variable renewables on their systems to use power production forecasting.

In the future, increasing solar penetration level requires solar energy generators to participate in parts of the regular DA and HA markets. In this case, the marketplace for renewable forecasting would change dramatically, since the economic benefit and interest in forecasting would shift to the owner-operators of solar power plants.

For example in Spain, there is premium tariff for the regulation of renewable energy which allows operators of power plants to participate directly on the electricity market instead of reverting to flat-rate prices. With the incentive, operators of renewable energy plants would act like operators of conventional plants to sell electricity at the liberalized market. The operators bids in advance on the market and is obliged to fulfil the biddings. It is necessary for the renewable energy plant operators to provide high accuracy forecast on the energy to enjoy the profitable premium tariff.

Currently in Singapore, SERIS has provided both minute ahead and hour ahead forecasting for Energy Market Authority (EMA). With increasing share of solar energy generation, EMA will release similar guidelines like CAISO to facilitate the grid integration of solar energy.

2.1.1 Cost saving on energy buffers using forecasting

The variability of short-term PV output is well understood but remains a major concern to the grid operators and utilities, who have to manage the variable source appropriately. From the grid operator's point of view, the cost of keeping the variable source's ramp rates below specific thresholds must be carefully examined. This cost can be quantified by the shock-absorbing hardware like energy buffers, which receives the variable PV output and deliver an output with specific maximum ramp rate requirements (Lentz et al., 2014).

The cost can be evaluated using a function of four components:

- The time scale of the ramp rate requirement;
- The spatial distribution of the generating resources: from a single point to a PV resource distributed over 200 km× 200 km;
- The climate environment including tropical, semi-arid and temperate locations;
- The availability of solar forecasts.

In this study (Lentz et al., 2014), to determine the cost of the buffers, one-year PV output time series for horizontally-mounted PV systems operating are used, in three climatically distinct locations: Hanford, in Central California, Goodwin Creek in the southeastern US, and Kalaeloa in Hawaii. For each of the location, 13 spatial resolutions (from single point to 200 km× 200 km) and 6 temporal resolutions (from one minute to two hours) are analysed, using a total of 78 PV output time series.

The impact of the ramp mitigation objective on buffer cost for two temporal resolution (1 minute and 15 minute) and two spatial resolution (1 km× 1 km and 30 km× 30 km) is shown in Figure 2.1. This example shows that buffer cost decreases significantly with the ramp mitigation target. The solar forecast availability systematically leads to lower costs by an average of $50-300 per kW of PV across this illustrative example.

The study has been extended to operational scenarios by setting real operational ramp mitigation targets: 5% of installed PV capacity at one-minute, 10% at 5 minutes, 15% at 15 minutes and 25% at one hour. For a single point, the operational cost is of the order of $300-350 per kW of PV with solar energy forecasts and would be about 40% higher without. Dispersed at the

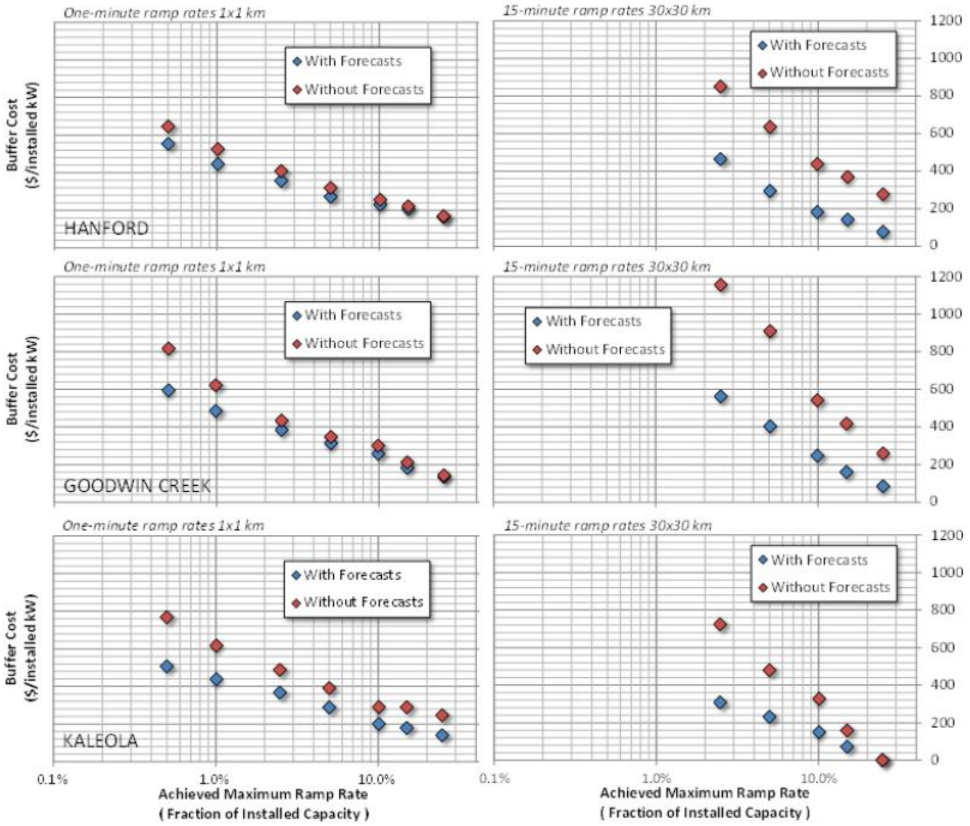

Figure 2.1: Influence of ramp mitigation objective on buffer cost for selected spatial and temporal resolutions

level of a large substation covering 20 km× 20 km, PV generation could be operationally mitigated for $150-250 per kW, but this cost would be nearly twice as much without forecasts.

2.2 Solar forecasting fundamentals

2.2.1 Solar Radiation

The amount of solar electromagnetic radiation per unit area per unit time received outside the earth's atmosphere is defined as solar constant G_{SC}. G_{SC} is a measure of flux estimated at the mean distance of the earth from the sun.

The power of the solar radiation is $1.367 \pm 1\%$ kW/m^2, which is measured by satellite and recognised by the World Radiation Centre (World Radiation Centre (WRC), 2014). The changing distance between the sun and the earth varies the solar radiation by up to ±3.3%. This can be estimated by the following equation:

$$\begin{aligned} G_{on} &= G_{SC}(1.00011 + 0.034221\cos B + 0.00128 \sin B \\ &\qquad + 0.000719\cos 2B + 0.000077\sin 2B) \end{aligned} \tag{2.1}$$

where $B = (n-1)\frac{360}{365}$ and G_{on} is the radiation on a plane normal to the incidence outside the atmosphere on the nth day of a year from the 1st January (Duffie and Beckman, 2006).

Considering the solar radiation at the earth's solid surface, "direct" radiation is the part that has not been scattered by the atmosphere and "diffuse" radiation is the part that has been scattered by the atmosphere. The details will be discussed in the later part of this section.

2.2.1.1 Solar irradiance

For the power per unit area of electromagnetic radiation at a surface, the radiometry term "irradiance" is usually used when the radiation is incident on the surface. The SI unit for irradiance is watts per square meter (W/m^2).

For the incident energy per unit area on a surface, “radiant exposure” is used to represent the sum of energy arriving over a specific time period and the SI unit is J/m^2. Specifically for solar energy radiant exposure, "insolation" is often used instead of “radiant exposure”.

When a surface is directly facing the sun, the insolation into the surface is largest. The insolation is reduced as the angle increases between the direction of the rays of sunlight and the direction at a right angle to the surface.

Direct insolation is calculated by subtracting atmospheric losses due to scattering and absorption from the solar constant. The atmospheric loss depends mainly on cloud cover condition, the time of day, impurities and moisture content. On a clear sky day, the insolation is reduced to approximately 1000 W/m^2 for a surface perpendicular to the sun at sea level, due to the attenuation passing through the atmosphere (Newport, 2014).

2.2.1.2 Atmospheric considerations

When radiation passes through a medium, non-uniformities may force it to deviate from a straight trajectory. This physical process is called scattering. There are many types of non-uniformities causing scattering, including bubbles, droplets, fluids with density fluctuations, various particles, etc. In the earth’s atmosphere specifically, all atoms and molecules scatter sunlight. The scattering due to water and particulates can be significant.

Light scattering is important because most objects’ visible appearance relies on it. When a surface almost completely scatters the light, it appears to be white to human eyes. Three categories are usually defined in light scattering. Defining a dimensionless size parameter α:

$$\alpha = \frac{\pi D_p}{\lambda} \tag{2.2}$$

where πD_p is the circumference of a particle and λ is the wavelength of incident radiation. The three categories are defined according to α:

- $[\alpha \ll 1]$ Rayleigh scattering
- $[\alpha \sim 1]$ Mie scattering
- $[\alpha \gg 1]$ Geometric scattering

Small spherical matters like bubbles, droplets and particles can cause Rayleigh scattering. Additionally, there exist microscopic density fluctuations within pure gases which also lead to Rayleigh scattering. This is the reason why the Earth's sky is blue, since the blue wavelengths of sunlight are scattered more strongly than other wavelengths. Rayleigh scattering is the main attenuation phenomenon of radiation by the atmosphere.

Absorption is when the energy of a photon is taken by the electrons of an atom or molecule of matter. The energy taken by the matter may be transformed to another form or re-emitted. Absorption is the other main attenuation of radiation by the atmosphere, besides Rayleigh scattering.

In practice, to quantify the attenuation of solar radiation by the atmosphere, aerosol optical depth (AOD) is defined. AOD measures the extinction of solar radiation contributed by an atmosphere-long column of aerosols. To determine AOD, radiometers point directly at the sun measuring the spectral transmission of solar radiation. The validation and calibration of AOD modelling is based on ground based AOD measurements and satellite data.

Direct normal irradiance (DNI), diffuse horizontal irradiance (DHI) and global horizontal irradiance (GHI) are the three fundamental components of solar radiation at the Earth's surface relating closely to solar irradiance forecasting. DNI is the direct solar radiation available from a planar surface normal to the Sun. It is usually measured by a pyrheliometer. DHI is the solar radiation from the sky dome excluding DNI. This part of solar radiation is scattered by atmospheric constituents like particles and clouds. DHI is usually measured by a shaded pyranometer. GHI is the total hemispheric solar radiation on a horizontal surface. It is usually measured by an unshaded pyranometer.

For any surface, GHI equals DNI plus DHI. For a horizontal surface:

$$GHI = DNI \times \cos(Z) + DHI \tag{2.3}$$

where Z is the zenith angle (Lorenz, Kühnert, and Heinemann, 2014).

2.2.2 Solar irradiance instrumentation

DNI is measured by a pyrheliometer. Pyrheliometers track the Sun throughout the day and typically employ a 5° to 6° aperture allowing only the direct solar radiation to the sensor so that diffuse radiation from the sky is excluded from by the equipment. The circumsolar radiation is also counted as DNI since up to 40% of the DNI comes from it (Blanc et al., 2014).

The DHI and GHI are measured by a pyranometer. Pyranometers can receive total hemispheric solar radiation on a horizontal surface. In order to measure DHI, a disk or ball is placed in the path of the direct sunlight beam to the sensor. This blocking part tracks the Sun throughout the day. For a research level equipment, the tracking-shade device must be implemented.

Fundamentally, the thermopile detectors absorb incident solar radiation and output a signal relating the temperature of the detector. Within thermopile detectors, there is a black absorbing surface absorbing solar radiation. 20 to 40 thermojunctions are in contact with the surface enabling thermal flux to flow to “cold junctions”. The thermal flux then produces a voltage proportional to the temperature difference. The temperature difference are typically 5 °C for a 1000 Wm^{-2} optical input, resulting in a 4 mV to

8 mV signal. However, the output of thermocouples is not perfectly linear and the absorbing surface of the detector is not perfectly isotropic, which lead to uncertainty in the measurement.

Another type of sensor is solid-state silicon photodiodes. It generates photovoltaic current proportional to the incident solar radiation flux. This type of sensor is much cheaper than the radiometers mentioned above. However, it sacrifices the measurement accuracy since silicon photodiodes have smaller spectral response ranges and cannot produce a signal proportional to the whole radiation spectrum. With the atmosphere changing composition during the day, varying infrared spectral content of the solar radiation cannot be captured by silicon photodiodes.

2.3 Review of solar irradiance forecasting models

2.3.1 Statistical time series models

With an increasing share of solar energy in power grid operations, many applications require short-term forecasts, for example operational planning, short-term power purchase, reserve usage planning, peak load matching, source switching, backup programming, etc. Statistical time series models are well suited for short-term solar irradiance forecasting. Several statistical time series models are introduced in this section.

2.3.1.1 The persistence model

The persistence model is the most basic forecasting model. Persistence indicates that the future predicted value is unchanged from the current observed value. In this time series, the value at future time $t+h$ is the same as the value at current time t. The implementation of this model is straightforward:

$$r_{t+h} = r_t \tag{2.4}$$

under the assumption that the time series is stationary. A stationary time series means the variance and mean of the series do not change over time. However, it is well known that the solar irradiance received at the ground is not stationary due to the influences from all atmospheric factors, and diurnal and seasonal cycles. To overcome this limitation, detrend models are implemented to decompose the solar irradiance time series into a trend component and a random component.

2.3.1.2 Detrend model

Many detrend models have been proposed in the literature. The high order polynomial model was first published by Al-Sadah et al. (Al-Sadah, Ragab, and Arshad, 1990b) and claimed by them to be a good fit to the daily GHI trend:

$$r_t = a + bt + ct^2 \tag{2.5}$$

where a, b and c are the regression parameters.

The cosine function model was first used by (Kaplanis, 2006):

$$r_t = a + b\cos(\frac{2\pi(t-d)}{24}) \tag{2.6}$$

where a and b are the regression parameters and d is the peak irradiance hour of the day.

The Gaussian function model (Baig, Akhter, and Mufti, 1991) tries to fit the GHI series with a Gaussian function:

$$r_t = \frac{1}{\sigma\sqrt{2\pi}} \exp^{-(t-d)^2/2\sigma^2} \tag{2.7}$$

where σ is the standard deviation of the Gaussian curve (the regression parameter that should be decided by the actual data) and d is the peak irradiance hour of the day which corresponds to the expected mean of the Gaussian distribution.

2.3.1.3 ARIMA model

Every time series is fundamentally a realization of a stochastic process. Based on the nature of time series, autoregressive (AR) models and moving average (MA) models have been developed by many authors. The AR model formulates the linear dependence between the forecast value and the previous observed values with the consideration of stochastic difference. The MA model formulates the linear regression of the current time series against white noise (Box, Jenkins, and Reinsel, 1970). The autoregressive integrated moving average (ARIMA) model combines AR model, MA model and a differencing component. The ARIMA model can be expressed as:

$$R_t = (1-B)^d r_t \tag{2.8}$$

$$(1-\Sigma_{i=1}^{p}\phi_i B^i)R_t = (1+\Sigma_{i=1}^{q}\theta_i B^i)\epsilon_t \tag{2.9}$$

where p is the autoregressive parameter, d is the number of differencing passes, q is the moving average parameter, B is the backward operator, ϵ is a Gaussian white noise error term and ϕ and θ are fitting coefficients. Parameters p, d and q are determined using model identification tools (Box, Jenkins, and Reinsel, 1970) and the coefficients ϕ and θ are determined using minimization procedures.

ARIMA prediction can be seen as a constant or weighted sum of one or more recent values in the time series, or a weighted sum of one or more recent errors. The constant or weighted sum of one or more recent values in the time series is the AR part. The weighted sum of one or more recent errors is the MA part. The "integrated" part is the differenced time series in order to make it stationary.

The ARIMA model has been widely deployed in many forecasting fields and is often used as a comparison benchmark for new models developed (Voyant et al., 2014). The performance of the ARIMA model for solar irradiance forecasting has been evaluated at various short-term intervals (Reikard, 2009b). Additional variables including cloud cover information and humidity level are also introduced into the autoregressive model family (Bacher, Madsen, and Nielsen, 2009).

2.3.2 Machine learning models

Machine learning is the study of building algorithms that learn, adapt and predict based on available data. It involves computational statistics, pattern recognition and mathematical optimization. Machining learning is widely applied in the field of solar irradiance forecasting. Different machine learning models are discussed in this section.

2.3.2.1 kNN model

As one of the simplest machine learning models, the k-Nearest-Neighbours (kNN) algorithm has been widely implemented in pattern recognition, classification as well as forecasting. For solar irradiance time series forecasting, the kNN model processes the historical time series data and identifies the best candidate that is similar to the current situation. Then the forecast value is determined by the subsequent time stamp of the best candidate. Fundamentally, the kNN model identifies the past patterns and uses the most resembling pattern to predict subsequent values.

2.3.2.2 ANN model

Artificial neural network (ANN) model is one of the most widely applied machine learning algorithms in solar irradiance forecasting. Resembling the biological processing neurons, the ANN model constructs an interconnected network structure of computational nodes to adapt and process a certain problem. To optimize the adaptive capability of the ANN model, the network architecture, the connection between nodes and network parameters must be carefully designed. The ANN model has proven to be effective in data classification, non-linear function approximation and system simulation.

Back in the 1990s, researchers started to estimate and forecast solar irradiance using environmental and weather parameters. A large number of ANN models with various architectures and parameters were built and investigated. Several specific areas of research are discussed in the rest of this section in order to provide a comprehensive understanding of relevant ANN model applications.

In order to generate hourly solar irradiance, atmospheric transmittance has been used as the input of an ANN model (Hontoria, Aguilera, and Zufiria, 2002). The atmospheric transmittance is decomposed into two parts: trend component and random component. The Multi-layer perceptron (MLP) model with feed-forward feedback architecture is used on the trend component as well as the autocorrelation coefficient and standard deviation of the random component. Eight years of data from seven stations in Spain are used to verify the model: seven years of data for training the ANN model and one year of data for validation. Both the trend and random components are shown to be reproduced by the model proposed.

Another ANN model using hourly values of the input climatic parameters has been proposed to estimate hourly values of global solar irradiance (M. Santamouris and Asimakopoulos, 1999). Air temperature, sunshine duration, humidity and calculated extraterrestrial radiation are used as input parameters. This model makes use of a deterministic atmospheric model, and a backpropagation procedure with a fuzzy logic method. The network architecture of this model consists of one hidden layer of fifteen log-sigmoid neurons and a single output layer of one linear neuron. Eleven years of data are used to train this model and one year of data is used as validation. The results show that backpropagation ANN model is effective in predicting hourly solar irradiance values. Additionally, the authors also conclude that the larger architecture of this ANN model has a longer converging time without significantly improving the forecasting accuracy, based on their experiments using more hidden layers and hidden nodes architectures. Similar approaches have also been applied in recent years (Renno, Petito, and Gatto, 2015).

Other ANN models like recurrent neural networks and radial basis neural networks are also proposed in estimating hourly solar irradiance (Sfetsos and Coonick, 2000). Raw solar irradiance values, temperature, air pressure, wind speed and direction are used as input parameters. After comparing several ANN models with adaptive neurofuzzy inference scheme, a feed-forward model with the Levenberg-Marquardt algorithm is found to outperform other models to be the optimal irradiance forecasting model.

MLP models with Radial Basis Functions (RBF) model are used to predict solar irradiance from a clearness index (Dorvlo, Jervase, and Al-Lawati, 2002). The clearness index in this model is defined as the ratio of the measured solar irradiance to the maximum solar irradiance measured in a clear day. In this approach, three MLP models with one, two and three hidden layers together with one RBF model are implemented to train and validate with ten years of data from eight meteorological stations. The input parameters are time, sunshine ratio, altitude, latitude and longitude. The models produce the clearness index as the output, which is then multiplied by the maximum solar irradiance to get the estimation of the solar irradiance. The result shows that the performance of the applied models are similar but the computational speed is optimized by RBF. The RBF model and its variations have also been discussed in recent applications (Jiang et al., 2015).

A backpropagation ANN model is adopted to predict solar irradiance as wells as infra-red and ultra-violet components (Elminir, Areed, and Elsayed, 2005). The input parameters are cloudiness, wind velocity, wind direction, humidity and ambient temperature. One year of data is used in training and the subsequent year of data is used in validation.

The ANN model has been used to predict daily solar irradiance for many years. A backpropagation ANN model has been applied using various input weather and environmental parameters including ambient temperature, daily precipitation, humidity, sunshine duration, clear sky irradiance and others (Elizondo, Hoogenboom, and McClendon, 1994). Twenty-three years of data from four meteorological stations are used in this study. Half of the data is used as training set and the other half is used as testing set. The predicted daily solar irradiance values from output of the model is compared with the measured solar irradiance values. The result shows that the performance of the model is excellent.

A multi-stage ANN model is designed to forecast the next day total solar irradiance (KEMMOKU et al., 1999). Six years of weather data are used in this approach. The input parameters include clearness index, temperature, local maxima and minima of atmospheric pressure, the average atmospheric pressure, etc. In the first stage of the ANN model, the average atmospheric pressure is predicted from the historical data, since the solar irradiance depends on weather conditions which can be reflected by the atmospheric pressure. In the second stage, the predicted solar irradiance is classified into one of three levels, namely high, middle and low, using the result of the first stage and other meteorological data. Each level corresponds to a specifically designed neural network. In the final stage, the result from last stage is refined to produce a final result. The result of this study shows the multi-stage ANN model is effective in forecasting daily solar irradiance. There are similar applications in more recent research (Amrouche and Pivert, 2014).

A wavelet architecture ANN model has also been proposed to predict daily solar irradiance (Mellit, Benghanem, and Kalogirou, 2006). In this architecture, wavelets are used as activation functions in feedforward neural networks. The benefit of using wavelets is to improve learning performance by constructing a double local structure. This technique has been widely applied in data classification problems. Five different structures are proposed in this study to predict daily total solar irradiance from various input combinations. Twenty years of data from a meteorological station have been used to train and test the different structures of the model. Variations of wavelet neural network have also been discussed in recent years (Sharma et al., 2016).

2.3.2.3 Time Series Prediction Models

The ANN model can be used to forecast solar irradiance from times series irradiance data (Mihalakakou, Santamouris, and Asimakopoulos, 2000). Twelve years of time series data are used for the training and testing of this model. The data with the value of zero at night time are removed from the data sets. Two versions of the ANN models are proposed in the study. The first version implements a one-lag scheme to predict one time step in the future. The prediction is based on actual past measured values only. The second version implements a multi-lag scheme to forecast several time steps in the future. The forecast is based on both past measured values and predicted output which is fed back to the model.

A multilayer feedforward network based on a backpropagation learning algorithm is used for both versions. The optimized structure contains one hidden layer with sixteen log-sigmoid neurons and one output layer with one linear neuron. The result shows that one-lag scheme outperforms the multi-lag scheme. The authors also conclude that the variability of the solar irradiance has significant influence in time series prediction models.

2.3.2.4 Genetic algorithms

In order to create an ANN forecasting model, several architecture components must be chosen carefully. First of all, the overall structure is determined by the number of layers and the number of neurons per layer. Secondly, the preprocessing scheme needs to be chosen among smoothing, differencing and spectral decomposition. Thirdly, the training and testing data must be distributed appropriately.

After analysing various ANN forecasting models, it is shown that the input parameters have huge influence in the performance of the models. With the advance of meteorological monitoring stations and satellite technologies, there are many parameters available for the ANN model. Considering various locations and climate conditions, it can be difficult to decide which variables have the most direct impact on the irradiance forecasting. Moreover, data preprocessing may also lead to new variables increasing the overall parameter space. Conventionally, researchers apply trial-and-error approaches which are inefficient and have little chance to obtain the optimal input selection and ANN structure. To overcome this limitation, genetic algorithms are proposed to be the optimization methods.

Genetic algorithms make use of genetic operators to implement an artificial survival-of-the-fittest scheme. Genetic evolution begins with various individual samples in the solution space. These samples carry genetic features which are encoded from certain parameters defining the sample identity in the population. In ANN optimization, crucial parameters like number of layers, number of neurons and input parameters, are encoded into individual samples in the solution space. The genetic algorithms will find the fittest solution through selection, crossover and mutation in the evolution of the entire solution space. With the fitness measure defined as the minimization of forecasting error, the fittest solution presents the ANN parameters with minimal forecasting error.

2.3.3 Satellite analysis models

Even though measuring solar irradiance from the ground is the most accurate method to evaluate solar resource in a certain site, satellite-derived solar irradiance is still valuable in those area with a low spatial density of monitoring stations. It is as effective as interpolation from ground stations at a distance of 25 km (Beyer, Costanzo, and Heinemann, 1996).

Many models have been proposed to estimate solar irradiance at ground level using satellite image analysis. They are usually classified into two groups: statistical models and physical models. The statistical models perform statistical regression between satellite information and ground observations. The physical models requires precise information on the atmospheric conditions. These atmospheric parameters are used to model solar radiation attenuation through the atmosphere.

There are two kinds of satellites orbiting around the earth: polar orbiting satellites and geostationary satellites. The polar orbiting satellites have high spatial resolution since their orbit height is only around 800 km. However the temporal coverage is limited for this kind. For the geostationary satellites, they are orbiting at around 36000 km from the ground. They are able to provide a temporal resolution up to 15 minutes and a spatial resolution up to 1 km. Generally, information from geostationary satellites is used in satellite analysis models.

2.3.3.1 Fundamentals

Before the solar radiation reaches the surface of the Earth, it travels through the atmosphere interacting with the atmospheric constituents. The radiation is partly reflected to the space, partly absorbed, with the rest reaching the ground. The ground absorbs part of the radiation and reflects the rest back to space through the atmosphere. The information received by the sensor of a satellite is the radiation emerging from the atmosphere, which consists of two parts: solar radiation reflected by the atmosphere and the radiation reflected by the ground.

The following equation is expressed based on the conservation of energy:

$$I_o = I_r + E_a + E_t \tag{2.10}$$

Here I_o is the extraterrestrial solar radiation, I_r is the solar radiation reflected by the earth-atmosphere system, , E_a is the solar radiation absorbed at the atmosphere , and E_t is the solar radiation absorbed at the earth surface.

The relationship among E_t and the surface albedo (ρ) and incident solar irradiation (I_G) can be expressed as:

$$E_t = I_G(1 - \rho) \tag{2.11}$$

Then I_G can be derived as:

$$I_G = \frac{1}{1 - \rho}[I_o - I_r - E_a] \tag{2.12}$$

This equation (2.12) is the most fundamental equation to derive solar radiation from satellite images, and is widely used in most of the models.

There are many advantages to make use of satellite images to estimate and forecast solar irradiance. First of all, satellite images enable solar resource analysis without ground measurements. Second, a series of satellite images can be used to forecast the solar irradiance in a specific location (a pixel of an image). Third, satellite images also show solar irradiance information for a large ground area which is convenient for spatial analysis of solar irradiance on the ground.

The satellite images used to estimate solar irradiance come from the visible channel of a satellite. The image shows the ground and atmospheric state at a certain time and a specific spatial resolution. The varying factor is mainly contributed by the state of atmosphere and the reflectance of the ground. The information on cloudiness at a certain time and location can be derived from the satellite image. It is convenient to define a parameter, namely cloud index, describing the cloudiness derived from radiance measurements of the satellite radiometer. One way to define cloud index is shown in equation 2.13,

$$n = \frac{\rho - \rho_g}{\rho_c - \rho_g} \tag{2.13}$$

where ρ is the reflectance viewed by the satellite radiometer, ρ_c is the reflectance of the clouds (cloud albedo) and ρ_g is the reflectance of the ground (ground albedo) (Diagne et al., 2013).

The reflectance can be derived from the radiance measured by the satellite.

$$\rho = \frac{\pi L_\Delta}{E_\Delta} \tag{2.14}$$

where L_Δ is the radiance and E_Δ is the incident solar irradiance within the spectral band of the satellite radiometer.

The ground albedo represents the clear sky situation and the cloud albedo represents the maximum overcast sky condition. According to equation (2.13), it can be seen that the cloud index tends towards zero under the clear sky situation and tends towards unity under complete overcast sky situation.

The cloud index may be defined differently but the importance of this concept is that solar irradiance can be derived from the cloud cover information captured by the satellite. It is usually assumed that there is a linear relationship between the cloud index and the atmospheric transmission (Diagne et al., 2013).

2.3.3.2 Geostationary meteorological satellite images

Geostationary satellites rotate around the earth axis at the same speed of the earth self rotation and at a fixed hight above the Earth. Therefore they appear stationary from the ground. The satellites can only collect images from the same part of the earth disc. Since the geostationary satellites are located above the equator, the spatial resolution decreases when the latitude becomes higher. Usually above 70 degree south or north, the low spatial resolution limits the application (Lorenz et al., 2009).

The satellite images are scanned by the radiometers on the geostationary meteorological satellites. There are generally four kinds of resolution stated in a certain set of satellite images: spatial resolution, time resolution, spectral resolution and radiometric resolution (Perez et al., 2004).

The spatial resolution represents the geographical size of each pixel in the satellite image. The resolution depends mainly on the angular section detected by the sensor. The time resolution is the time interval between two consecutive images. The spectral resolution depends on the number of spectral bands and the spectral range of the sensor. The radiometric resolution indicates the sensitivity of the radiometer.

There are three main channels for most of the geostationary satellites: a visible channel, a thermal infrared channel and a water vapour channel. More spectral channels are currently adding to the new generations of geostationary satellites (Rigollier, Lefvre, and Wald, 2004).

2.3.3.3 Satellite-based models

During the last three decades, several well-known models for deriving solar irradiance from satellite information have been developed and improved in different aspects. In the evolution process of these models, pure empirical models and pure physical models tend to combine with each other to form more accurate modelling. This also represents the trend of hybridization in various solar irradiance modelling applications.

Cano was one of the pioneers in satellite-based modelling and proposed the famous Heliosat model using Meteosat satellite images (Cano et al., 1986). Many researchers have made modifications and improvements based on this model to develop various versions (Diabat, Moussu, and Wald, 1989; Beyer, Costanzo, and Heinemann, 1996; Rigollier, Lefvre, and Wald, 2004). The original Heliosat 1 model was a pure empirical model. After considering physical atmospheric parameters (Linke turbidity factor[1]), Heliosat 2 model was proposed. In the Second Generation Meteosat (MSG), Heliosat 3 model was proposed incorporating aerosol and other atmospheric absorber parameters.

Heliosat 1 model proposed a linear relationship between the cloud index (2.13) and the clearness index (k_T) which is defined as the hourly global solar irradiance normalised by the extraterrestrial irradiance,

$$k_T \;=\; an \;+\; b \tag{2.15}$$

where a and b are parameters derived from fitting the ground data.

In addition to cloud cover radiation extinction, Heliosat 2 model also takes atmospheric radiation extinction into consideration. Firstly the irradiance under clear skies is estimated using a clear sky model with Linke turbidity

---

[1] The Linke turbidity factor is the full spectrum radiation attenuation unit that is produced in a cloudless atmosphere containing neither aerosols nor water vapour.

factor as the only atmospheric parameter (Rigollier, Bauer, and Wald, 2000). The Linke turbidity factor is defined as the number of days with solar radiation extinction under clear and dry atmosphere. Then the estimation of ground and cloud reflectance can be derived from,

$$\rho_g = \frac{\rho - \rho_{atm}}{T_u T_d} \tag{2.16}$$

$$\rho_c = \frac{\rho_{eff} - \rho_{atm}}{T_u T_d} \tag{2.17}$$

T_d is the downward (sun to ground) transmittance and T_u is the upward transmittance of the clear atmosphere. ρ_{atm} is the intrinsic reflectance of the atmosphere which can be derived from the diffuse irradiance under clear sky. ρ_{eff} is the effective cloud albedo which is defined by

$$\rho_{eff} = 0.78 - 0.13[1 - exp(-4\sin^4\alpha)] \tag{2.18}$$

where α the solar elevation angle (Rigollier, Bauer, and Wald, 2000).

The last step is to find the relationship between the clear sky index, k_c, defined as the global irradiance normalised to the clear sky global irradiance, and the cloud index by the following set of equations (Rigollier, Bauer, and Wald, 2000),

$$n < -0.2\ ,\ k_c = 1.2 \tag{2.19}$$

$$-0.2 \leq n < 0.8\ ,\ k_c = 1 - n \tag{2.20}$$

$$0.8 \leq n < 1.1\ ,\ k_c = 2.0667 - 3.6667n + 1.6667n^2 \tag{2.21}$$

$$1.1 \leq n\ ,\ k_c = 0.05 \tag{2.22}$$

The Heliosat 3 model is further improved based on the enhanced information from multiple channels of MSG. Linke turbidity is on longer the only atmospheric parameter involved in the calculation scheme. Many other atmospheric parameters are available from the MSG to make radiative transfer modelling possible, which can calculate the solar radiation attenuation through the atmosphere more accurately.

The Perez model is another variation of the original Cano model (Cano et al., 1986), which is developed by the Atmospheric Sciences Research Centre (ASRC) of the University of Albany. It has been mainly applied to the GOES satellite images.

In Perez model, global hourly irradiance is derived from the cloud index and the global irradiance of clear sky,

$$I_G = I_{CS} f(n)[0.00011 I_{CS} f(n) + 0.9] \tag{2.23}$$

$$f(n) = 2.36n^5 - 6.2n^4 + 6.22n^3 - 2.36n^2 - 0.58n + 1 \tag{2.24}$$

where I_G is the global hourly irradiance, n is the cloud index and I_{CS} is the global irradiance of clear sky (Perez et al., 2004).

The global irradiance of clear sky is determined by the Kasten model with some modifications incorporating a improved formulation of the Linke turbidity coefficient eliminating the dependence on solar geometry (Perez et al., 2004).

Another external datum used by the model is the snow cover data provided by National Operational Hydrologic Remote Sensing Center. The algorithm of the model can be dynamically modified based on snow cover data to determine the cloud index.

The author also developed new methodologies to retrieve solar irradiance more accurately at complex terrain with high reflectance surface(Perez et al., 2004).

The BRASIL-SR model can generate solar irradiance maps using the GOES satellite images, surface albedo, ground data on temperature, relative humidity and visibility, to solve the radiative transfer function (Pereira et al., 2000; Martins, Pereira, and Abreu, 2007). The global irradiance can be derived from

$$I_G = I_0[nT_{cloud} + (1-n)T_{clear}] \tag{2.25}$$

where n is the cloud index, T_{clear} is the sky transmittance for clear condition and T_{cloud} is the sky transmittance for cloudy condition.

The radiative transfer function is used to estimate the boundary conditions for the sky transmittances. The climate data including surface albedo, temperature, relative humidity, visibility and cloud conditions are the input to simulate the real atmosphere with absorption and scattering by gases and aerosols.

2.3.4 Total sky imager

Total sky imager (TSI) is another popular method to forecast short-term solar irradiance (Chow et al., 2011). TSI takes sky images sequentially in time. The cloud information then can be derived from the sky images through image processing.

There are commercially available TSIs in the market. The Yankee Environmental Systems' model TSI-800 is commonly used by some research groups (Chu, Pedro, and Coimbra, 2013). Many other groups are also developing their own TSIs to meet different research requirements (Yang et al., 2014).

Analysing the cloud motion sky images is challenging. Different approaches have been proposed. Cloud motion vector analysis are usually conducted to describe the movement of the clouds on time sequential sky images (Bernecker et al., 2014). The forecasting of cloud motion can calculated using motion vector persistence or advection-diffusion analysis (West et al., 2014). Even though the physical nature of the analysis has good potential, the current accuracy for short-term forecasting still improves little from persistence (Chu et al., 2015).

2.3.5 Numerical weather prediction

Numerical weather prediction (NWP) is the most commonly used long-term solar irradiance forecasting method. NWP models have the capability to analyse the initial state of the atmosphere and predict the change of atmosphere through physical laws which are the fundamentals of the evolution of the atmosphere (Lorenz, Kühnert, and Heinemann, 2014).

Many famous NWP models are available for weather forecasting, including Weather Research and Forecasting (WRF), Global Forecast System (GFS) and North American Mesoscale (NAM). These models have different underlying physical models, input parameters and spatial resolutions. To forecast solar irradiance, the choice of NWP model and the post-processing techniques are very important (Inman, Pedro, and Coimbra, 2013).

Among all the output parameters form NWP models, solar irradiance is only one of them. NWP is not specially designed to forecast solar irradiance. Therefore statistical post-processing is even more important for irradiance forecasting. Model output statistics (MOS) and Kalman filters are used widely in the post-processing (Diagne et al., 2014).

Chapter 3

Solar irradiance forecasting using novel statistical analysis

Statistical time series forecasting has been the most popular technique for short time scales. Statistical time series analyses such random walk (RW), autoregressive (AR), moving average (MA), simple exponential smoothing (SES) and autoregressive integrated moving average (ARIMA) method (Yang, Jirutitijaroen, and Walsh, 2012a; Reikard, 2009b), are widely used for modelling and prediction solar irradiance data.

Recently, the exponential smoothing method has attracted attention.

Table 3.1: 15 Exponential Smoothing Methods

		Seasonal		
		N (None)	A (Additive)	M (Multiplicative)
Trend	N (None)	NN	NA	NM
	A (Additive)	AN	AA	AM
	A_d (Additive damped)	A_dN	A_dA	A_dM
	M (Multiplicative)	MN	MA	MM
	M_d (Multiplicative damped)	M_dN	M_dA	M_dM

This method was developed by Robert G. Brown in a tracking model of military fire-control equipment in the USA Navy (Gass and Harris, 2000). Brown's simple exponential smoothing models have been extended to exponential smoothing with trends and seasonality. Brown's two books, *Statistical Forecasting for Inventory Control* (Brown, 1959), and *Smoothing, Forecasting, and Prediction of Discrete Time Series* (Brown, 1963), describe the fundamental methodology of exponential smoothing. In the 1950s, Charles C. Holt independently developed a similar exponential smoothing method with a different approach to smooth seasonal data, but this was not published until 2004 (Holt, 2004). Winters (Winters, 1960) further developed Holt's method and their work is known as the Holt-Winters forecasting system.

Muth was the first to demonstrate that exponential smoothing can forecast an optimal random walk with noise (Muth, 1960). Since then, many authors have worked to develop exponential smoothing within a statistical framework. Among them, (Box, Jenkins, and Reinsel, 1970), (Roberts, 1982), and (Abraham and Ledolter, 1983) pointed out that some linear exponential smoothing methods are special cases of ARIMA models.

Although substantial research had been done on the exponential smoothing method (Gardner, 1985), the method was considered an ad hoc forecasting approach since there was no appropriate underlying stochastic formulation until 2002 when (Hyndman et al., 2002) proposed the state space framework for exponential smoothing.

Exponential smoothing consists of a total of fifteen methods, which are summarized in Table 3.1 (adapted from (Hyndman et al., 2002)). Some of these methods were first published with different names: cell NN is simple exponential smoothing (SES) and cell AN is linear exponential smoothing (LES). This table will be expanded into Table 3.3 and explained into details in the next section.

3.1 Solar irradiance time series data

The first irradiance time series dataset we have used is from the rooftop station of the Solar Energy Research Institute of Singapore (SERIS) located at $(1.30°N, 103.77°E)$. The pyranometer used in this station is a meteorological class Delta-T SPN1 Sunshine Pyranometer[1]. Located just 1.0 degrees north of the equator on an island, Singapore enjoys a tropical climate with a daily temperature between 25 degrees Celsius and 31 degrees Celsius, and relative humidity of $70\% - 80\%$. Rainfall occurs almost every day but usually only for a short period of time. The high temperature and warm ocean leads to high evaporation, which causes fast cloud formation and dense cloud cover. Therefore the solar irradiance variability is high in Singapore.

The second set of irradiance time series data is from a rooftop station in South Park, Colorado, USA located at $(39.16°N, 105.37°W)$ (Measurement and Instrumentation Data Center (MIDC), NREL, 2012). The pyranometer used in this station is a LI-200 LI-COR Pyranometer which compares favourably with first class thermopile-type pyranometers [2]. The climate of Colorado South Park is semi-arid with low humidity and low precipitation. The solar irradiance variability is moderate and typical for the temperate zone. We would like to compare the performance of the forecasting models in this climate with the tropical climate in Singapore. This comparison will demonstrate the challenge in tropical climate forecasting.

---

[1] `http:\delta-t.co.uk`

[2] `http:\www.licor.com/pyranometer`

3.2 Forecasting methodology

This section details the steps in implementing our prediction model. First, our Fourier trend model is introduced and compared with other trend models. Second, the exponential smoothing forecasting equations are elaborated. In order to generate 95 percent confidence interval, the state space models of the exponential smoothing technique are then introduced. Finally, the model selection method is presented to identify the best model in each step forecast.

3.2.1 Trend model

The foundation of time series analysis is stationarity. A time series $\{r_t\}$ is said to be strictly stationary if the joint distribution of $(r_{t_1}, \ldots, r_{t_k})$ is identical to that of $(r_{t_1+t}, \ldots, r_{t_k+t})$ for all t, where k is an arbitrary positive integer and $(r_{t_1}, \ldots, r_{t_k})$ is a collection of k positive integers (Box, Jenkins, and Reinsel, 1970). This simply means the joint distribution of the time series remains unchanged under time shift. However, this condition is hard to verify empirically: thus a weaker version of stationarity is usually applied. A time series $\{r_t\}$ is considered weakly stationary if both the mean of r_t and the covariance between r_t and r_{t-l} are time invariant, where l is an arbitrary integer. In real applications, with N observed data points, weak stationarity implies that the time plot of the data would show that these N values fluctuate with constant variation around a fixed level. Weak stationarity is generally sufficient to predict future observations (Brown, 1963).

Since our global horizontal irradiance (GHI) data is non-stationary with a clear daily trend, this daily trend must be removed to obtain stationarity. The most commonly-used trend models include high order polynomials (Al-Sadah, Ragab, and Arshad, 1990b), cosine functions (Kaplanis, 2006) and the

Gaussian function model (Baig, Akhter, and Mufti, 1991). However, we have found that the performance of these models is not satisfactory and thus we have developed our own Fourier trend model.

By observing the weekly mean GHI data, we note that the diurnal cycle is not the only cycle existing in the trend. Several other cycles at higher frequency are also associated with the trend. After carrying out the spectral analysis of the GHI time series, these higher frequency cycles are clearly identified. The spectral density of the GHI time series of the year 2010 is shown in Figure 3.1, using the Singapore station's 5.0 minutes data.

The highest peak in the figure appears at the frequency of 1.16×10^{-5} Hz, which corresponds to the 24-hour daily cycle. Other peaks in the figure are also indicated. After obtaining these significant frequency peaks, the Fourier trend is generated based on these peak frequencies:

$$r_t = \mu + \sum_{i=1}^{n} [a_i \cos(2\pi f_i t) + b_i \sin(2\pi f_i t)] \tag{3.1}$$

where t is time, r_t is the fitted trend at different time, n is the number of significant frequencies and a_i, b_i are the regression coefficients. By fitting the sinusoids, we eliminate the significant cyclic behaviours (trend) from the GHI time series.

In order to test the performance of our Fourier trend model, three other popular trend models (namely a high order polynomials model, a cosine function model and a Gaussian function model) are built for comparison.

The high order polynomial model was first published by (Al-Sadah, Ragab, and Arshad, 1990b) and claimed to be a good fit to the daily GHI trend:

$$r_t = a + bt + ct^2 \tag{3.2}$$

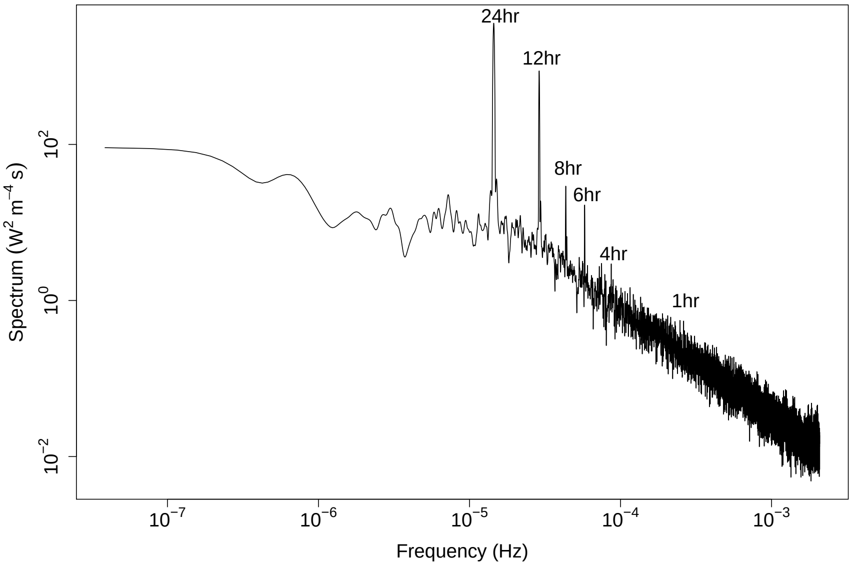

Figure 3.1: Solar irradiance spectral density of Singapore for 2010, using 5 minutes data

where a, b and c are the regression parameters.

The cosine function model was first used by (Kaplanis, 2006):

$$r_t = a + b\cos(\frac{2\pi(t-d)}{24}) \tag{3.3}$$

where a and b are the regression parameters and d is the peak irradiance hour of the day.

The Gaussian function model (Baig, Akhter, and Mufti, 1991) tries to fit the trend of GHI series with a Gaussian function:

$$r_t = \frac{1}{\sigma\sqrt{2\pi}} \exp^{-(t-d)^2/2\sigma^2} \tag{3.4}$$

where σ is the standard deviation of the Gaussian curve (the regression parameter that should be decided by the actual data) and d is the peak irradiance hour of the day which corresponds to the expected mean of the Gaussian distribution.

We take a random week's data (the first week of December 2010) to evaluate the performance of these trend models. After subtracting these trends from the weekly average of the daily GHI, the series of residual of the four trends are displayed in Figure 3.2. It is clear that unlike the Fourier trend model, the other three models fit poorly at the beginning and the end of the day.

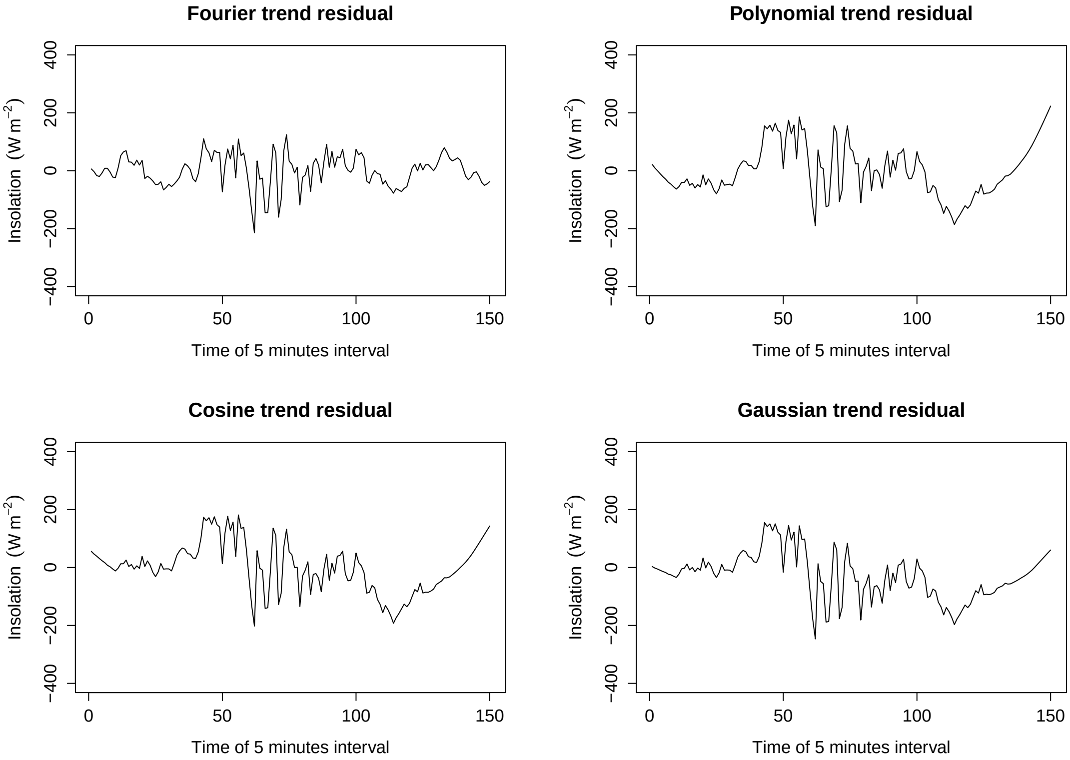

Figure 3.2: Plot of the four series of trend residual

The autocorrelation function (ACF) of the four series of residuals are shown in Figure 3.3. Autocorrelation is the linear dependence between observations as a function of time separation between them. Compared with the other three series of trend residual series, the series of Fourier trend residual has the smallest serial correlation, indicating that it is more stationary than the others.

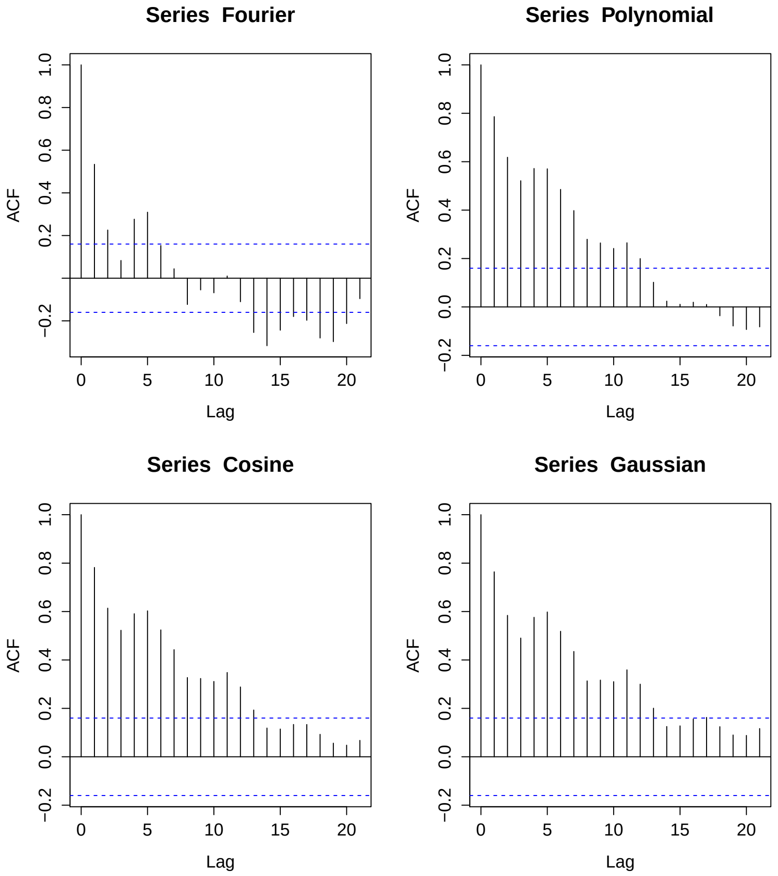

Figure 3.3: Autocorrelation function (ACF) of the four series of trend residual

To statistically evaluate the stationarity of these series of residuals, the Kwiatkowski-Phillips-Schmidt-Shin (KPSS) stationary test (Kwiatkowski et al., 1992) is used. The KPSS test is used to test a null hypothesis that an observable time series is not stationary. In our case, the test is carried out on the series of residuals under the null hypothesis that the underlying process is not stationary. If the test result (KPSS value) is larger than the

Table 3.2: KPSS test for the four trend methods

Detrend Method	Critical level	Critical value	KPSS value
Fourier trend	0.01	0.739	**0.1211**
Polynomial trend	0.01	0.739	**0.6973**
Cosine trend	0.01	0.739	**1.0772**
Gaussian trend	0.01	0.739	**1.3425**

critical value, the null hypothesis is accepted and the series of residual is not stationary; otherwise the null hypothesis is rejected and the series of residual is stationary. The lower the KPSS value, the higher the probability of obtaining stationarity. In order to compare the results, the critical level is fixed at 0.01[3] and the corresponding critical value is 0.739.

The KPSS test results are shown in Table 3.2. The KPSS values of the residual series of cosine trend and Gaussian trend are higher than the critical value, indicating that the two series are not stationary. The residual series of Fourier trend and high order polynomial trend are stationary since their KPSS values are smaller than the critical value. However, the KPSS value of the residual series of Fourier trend is much smaller than that of high order polynomial trend, which proves that the residual series of Fourier trend has much higher probability of obtaining stationarity. Hence we use the Fourier trend model for our further forecasting.

3.2.2 Forecast equations

There are fifteen sets of forecast equations in this forecast model. The observed time series is denoted by $y_1, y_2, \ldots, y_n$. The forecast for h steps ahead based on all the training data up to time t is denoted by $\hat{y}_{t+h}$.

---

[3] The numerical value of critical level is set to calculate the corresponding critical value, which is the threshold to reject null hypothesis in the KPSS test.

$$
\begin{aligned}
\text{Level:} \quad l_t &= \alpha A_t + (1-\alpha)B_t && (3.5)\\
\text{Growth:} \quad g_t &= \beta C_t + (1-\beta)D_t && (3.6)\\
\text{Seasonal:} \quad s_t &= \gamma E_t + (1-\gamma)s_{t-m} && (3.7)\\
\text{Forecast:} \quad \hat{y}_{t+h} &= f(l_t, g_t, s_{t-m+h_m}) && (3.8)
\end{aligned}
$$

where l_t is the level component at time t, g_t is the growth component at time t, s_t is the seasonal component at time t and $h_m = [(h-1) \mod m] + 1$ where m denotes the number of seasons in the data. In order to apply this method, the initial states l_0, g_0 and $s_{1-m}, \dots, s_0$, and the smoothing parameters α, β and γ, will be estimated from the training data. The values of A_t, B_t, C_t, D_t and E_t vary according to the cell which the method belongs to. Table 3.3 shows the values of A_t, B_t, C_t, D_t, E_t and the forecast equation (adapted from (Hyndman et al., 2002)).

It should be noted that there is an additive damped trend and a multiplicative damped trend in the table. The damped trend acts to dampen the trend with increasing length of the forecast horizon. The damped trend is applied because it is unrealistic to invariantly use the final estimate of the growth rate at the end of the training data to forecast different horizon. To forecast h periods ahead, the trend is damped by a factor of $\phi_h = \phi + \phi^2 + \cdots + \phi^h$.

3.2.3 State space model

The state space model is a more sophisticated stochastic concept than the exponential smoothing method. The exponential smoothing method can only produce a point forecast but the state space model provides the framework for computing prediction interval and other properties. Every exponential smoothing method corresponds to two possible state space models, one with

Table 3.3: Formulae for recursive calculations and point forecast equations

		Seasonal		
		N (None)	A (Additive)	M (Multiplicative)
Trend	N (None)	$A_t = y_t$	$A_t = y_t - s_{t-m}$	$A_t = y_t / s_{t-m}$
		$B_t = l_{t-1}$	$B_t = l_{t-1}$	$B_t = l_{t-1}$
			$E_t = y_t - B_t$	$E_t = y_t / B_t$
		$\hat{y}_{t+h} = l_t$	$\hat{y}_{t+h} = l_t + s_{t-m+h_m}$	$\hat{y}_{t+h} = l_t s_{t-m+h_m}$
	A (Additive)	$A_t = y_t$	$A_t = y_t - s_{t-m}$	$A_t = y_t / s_{t-m}$
		$B_t = l_{t-1} + g_{t-1}$	$B_t = l_{t-1} + g_{t-1}$	$B_t = l_{t-1} + g_{t-1}$
		$C_t = l_t - l_{t-1}$	$C_t = l_t - l_{t-1}$	$C_t = l_t - l_{t-1}$
		$D_t = g_{t-1}$	$D_t = g_{t-1}$	$D_t = g_{t-1}$
			$E_t = y_t - B_t$	$E_t = y_t / B_t$
		$\hat{y}_{t+h} = l_t + hg_t$	$\hat{y}_{t+h} = l_t + hg_t + s_{t-m+h_m}$	$\hat{y}_{t+h} = (l_t + hg_t) s_{t-m+h_m}$
	A_d (Additive damped)	$A_t = y_t$	$A_t = y_t - s_{t-m}$	$A_t = y_t / s_{t-m}$
		$B_t = l_{t-1} + \phi g_{t-1}$	$B_t = l_{t-1} + \phi g_{t-1}$	$B_t = l_{t-1} + \phi g_{t-1}$
		$C_t = l_t - l_{t-1}$	$C_t = l_t - l_{t-1}$	$C_t = l_t - l_{t-1}$
		$D_t = \phi g_{t-1}$	$D_t = \phi g_{t-1}$	$D_t = \phi g_{t-1}$
			$E_t = y_t - l_{t-1} - \phi g_{t-1}$	$E_t = y_t / (l_{t-1} + \phi g_{t-1})$
		$\hat{y}_{t+h} = l_t + \phi_h g_t$	$\hat{y}_{t+h} = l_t + \phi_h g_t + s_{t-m+h_m}$	$\hat{y}_{t+h} = (l_t + \phi_h g_t) s_{t-m+h_m}$
	M (Multiplicative)	$A_t = y_t$	$A_t = y_t - s_{t-m}$	$A_t = y_t / s_{t-m}$
		$B_t = l_{t-1} g_{t-1}$	$B_t = l_{t-1} g_{t-1}$	$B_t = l_{t-1} g_{t-1}$
		$C_t = l_t / l_{t-1}$	$C_t = l_t / l_{t-1}$	$C_t = l_t / l_{t-1}$
		$D_t = g_{t-1}$	$D_t = g_{t-1}$	$D_t = g_{t-1}$
			$E_t = y_t - l_{t-1} \phi g_{t-1}$	$E_t = y_t / (l_{t-1} \phi g_{t-1})$
		$\hat{y}_{t+h} = l_t h g_t^h$	$\hat{y}_{t+h} = l_t h g_t^h + s_{t-m+h_m}$	$\hat{y}_{t+h} = l_t h g_t^h s_{t-m+h_m}$
	M_d (Multiplicative damped)	$A_t = y_t$	$A_t = y_t - s_{t-m}$	$A_t = y_t / s_{t-m}$
		$B_t = l_{t-1} g_{t-1}^{\phi}$	$B_t = l_{t-1} g_{t-1}^{\phi}$	$B_t = l_{t-1} g_{t-1}^{\phi}$
		$C_t = l_t / l_{t-1}$	$C_t = l_t / l_{t-1}$	$C_t = l_t / l_{t-1}$
		$D_t = g_{t-1}^{\phi}$	$D_t = g_{t-1}^{\phi}$	$D_t = g_{t-1}^{\phi}$
			$E_t = y_t - l_{t-1} g_{t-1}^{\phi}$	$E_t = y_t / (l_{t-1} g_{t-1}^{\phi})$
		$\hat{y}_{t+h} = l_t h g_t^{\phi_h}$	$\hat{y}_{t+h} = l_t h g_t^{\phi_h} + s_{t-m+h_m}$	$\hat{y}_{t+h} = l_t h g_t^{\phi_h} s_{t-m+h_m}$

additive errors and the other with multiplicative errors. Additive errors and multiplicative errors provide different prediction intervals with the same parameter values. Since there are 15 exponential smoothing methods, 30 state space models are deduced accordingly. The state space model for exponential smoothing here is expanded from the general OKS framework (Ord, Koehler, and Snyder, 1997):

$$y_t = h(x_{t-1}) + k(x_{t-1})\epsilon_t \tag{3.9}$$

$$x_t = f(x_{t-1}) + g(x_{t-1})\epsilon_t \tag{3.10}$$

where the first equation is called observation equation and the second is called state equation. x_t is the state vector which in this case defined as $x_t = (l_t, g_t, s_t, s_{t-1}, \ldots, s_{t-(m-1)})$. We also define $e_t = k(x_{t-1})\epsilon_t$ and $\mu_t = h(x_{t-1})$ so that $y_t = \mu_t + e_t$. The additive error form can be expressed as $y_t = \mu_t + \epsilon_t$ where $\mu_t = y_{(t-1)+1}$ stands for the one-step point forecast at time $t-1$ and $k(x_{t-1}) = 1$. The multiplicative error form can be expressed as $y_t = \mu_t(1+\epsilon_t)$ where $k(x_{t-1}) = \mu_t$. All of the 15 exponential smoothing methods can be written in the state space model forms which is illustrated in Table 3.4.

3.2.4 Model selection criterion

Akaike's Information Criterion (AIC) is used to select the model to be used to perform the point forecasting. The AIC is specified by the following equations:

$$\begin{aligned} AIC &= L(\hat{\theta}, \hat{X}_0) + 2P & (3.11) \\ L(\theta, X_0) &= nlog(\sum_{t=1}^{n} e_t^2 / k^2(x_{t-1})) & \\ &\quad +2\sum_{t=1}^{n} log|k(x_{t-1})| & (3.12) \end{aligned}$$

Table 3.4: State space equations for additive error models. Multiplicative error models can be obtained by replacing ϵ_t by $\mu_t\epsilon_t$ in the equations

		Seasonal		
		N (None)	A (Additive)	M (Multiplicative)
Trend	N (None)	$\mu_t = l_{t-1}$ $l_t = l_{t-1} + \alpha\epsilon_t$	$\mu_t = l_{t-1} + s_{t-m}$ $l_t = l_{t-1} + \alpha\epsilon_t$ $s_t = s_{t-m} + \beta\epsilon_t$	$\mu_t = l_{t-1}s_{t-m}$ $l_t = l_{t-1} + \alpha\epsilon_t/s_{t-m}$ $s_t = s_{t-m} + \beta\epsilon_t/l_{t-1}$
	A (Additive)	$\mu_t = l_{t-1} + g_{t-1}$ $l_t = l_{t-1} + g_{t-1} + \alpha\epsilon_t$ $g_t = g_{t-1} + \alpha\beta\epsilon_t$	$\mu_t = l_{t-1} + g_{t-1} + s_{t-m}$ $l_t = l_{t-1} + g_{t-1} + \alpha\epsilon_t$ $g_t = g_{t-1} + \alpha\beta\epsilon_t$ $s_t = s_{t-m} + \beta\epsilon_t$	$\mu_t = (l_{t-1} + g_{t-1})s_{t-m}$ $l_t = l_{t-1} + g_{t-1} + \alpha\epsilon_t/s_{t-m}$ $g_t = g_{t-1} + \alpha\beta\epsilon_t/s_{t-m}$ $s_t = s_{t-m} + \beta\epsilon_t/(l_{t-1} + g_{t-1})$
	A_d (Additive damped)	$\mu_t = l_{t-1} + g_{t-1}$ $l_t = l_{t-1} + g_{t-1} + \alpha\epsilon_t$ $g_t = \phi g_{t-1} + \alpha\beta\epsilon_t$	$\mu_t = l_{t-1} + g_{t-1} + s_{t-m}$ $l_t = l_{t-1} + g_{t-1} + \alpha\epsilon_t$ $g_t = \phi g_{t-1} + \alpha\beta\epsilon_t$ $s_t = s_{t-m} + \beta\epsilon_t$	$\mu_t = (l_{t-1} + g_{t-1})s_{t-m}$ $l_t = l_{t-1} + g_{t-1} + \alpha\epsilon_t/s_{t-m}$ $g_t = \phi g_{t-1} + \alpha\beta\epsilon_t/s_{t-m}$ $s_t = s_{t-m} + \beta\epsilon_t/(l_{t-1} + g_{t-1})$
	M (Multiplicative)	$\mu_t = l_{t-1}g_{t-1}$ $l_t = l_{t-1}g_{t-1} + \alpha\epsilon_t$ $g_t = g_{t-1} + \alpha\beta\epsilon_t/l_{t-1}$	$\mu_t = l_{t-1}g_{t-1} + s_{t-m}$ $l_t = l_{t-1}g_{t-1} + \alpha\epsilon_t$ $g_t = g_{t-1} + \alpha\beta\epsilon_t/l_{t-1}$ $s_t = s_{t-m} + \beta\epsilon_t$	$\mu_t = (l_{t-1}g_{t-1})s_{t-m}$ $l_t = l_{t-1}g_{t-1} + \alpha\epsilon_t/s_{t-m}$ $b_t = g_{t-1} + \alpha\beta\epsilon_t/(s_{t-m}l_{t-1})$ $s_t = s_{t-m} + \beta\epsilon_t/(l_{t-1}g_{t-1})$
	M_d (Multiplicative damped)	$\mu_t = l_{t-1}g_{t-1}$ $l_t = l_{t-1}g_{t-1} + \alpha\epsilon_t$ $g_t = g_{t-1}^{\phi} + \alpha\beta\epsilon_t/l_{t-1}$	$\mu_t = l_{t-1}g_{t-1} + s_{t-m}$ $l_t = l_{t-1}g_{t-1} + \alpha\epsilon_t$ $g_t = g_{t-1}^{\phi} + \alpha\beta\epsilon_t/l_{t-1}$ $s_t = s_{t-m} + \beta\epsilon_t$	$\mu_t = (l_{t-1}g_{t-1})s_{t-m}$ $l_t = l_{t-1}g_{t-1} + \alpha\epsilon_t/s_{t-m}$ $g_t = g_{t-1}^{\phi} + \alpha\beta\epsilon_t/(s_{t-m}l_{t-1})$ $s_t = s_{t-m} + \beta\epsilon_t/(l_{t-1}g_{t-1})$

where L is the maximum likelihood function, P is the number of parameters in θ, $\hat{\theta}$ and $\hat{X}_0$ are the estimated of θ and X_0 where $\theta = (\alpha, \beta, \gamma, \phi)$ and initial states $X_0 = (l_0, g_0, s_0, s_{-1}, \ldots, s_{-m+1})$. The reason why the AIC is used instead of mean squared error (MSE) or mean average percentage error (MAPE) is that AIC can select between additive error and multiplicative error models. Since the two kinds of error models produce the same point forecast, MSE or MAPE cannot differentiate between them. However AIC is based on likelihood which meets our requirement. The model which minimizes the AIC will be chosen from among all the 30 models.

3.3 Experiments, results and discussion

The first set of experiments is based on the solar irradiance time series data from Singapore and the comparison set of experiments is based on the solar irradiance time series data from Colorado. Since it is meaningless to forecast solar irradiance after sunset, we only investigate samples from 07:00 to 19:30. The error type used is the normalized root mean square error (nRMSE) which is described by the following equation.

$$nRMSE = \frac{\sqrt{E[(X - \widehat{X})^2]}}{\sqrt{E[X^2]}} \tag{3.13}$$

where E is the expected value.

All the predicted values are true out-of-sample forecasts, in that they use only data prior to the start of the forecast horizon. The models are estimated over the data prior to the start of the forecast, the points of the next time step is forecast, and the forecast values are compared with the actual ones. The procedure is iterative until forecasts have been run over the daily data set. The SERIS data consists of twelve months from September 2010 to August

2011. Data from September 2010 is used to generate an average daily residual to fit in as the initialization of our prediction model, in order to forecast the time series of the next month, i.e. October 2010. In the forecasting test after October 2012, the data from the previous month is used to form average daily residual initially fitting in the prediction model.

3.3.1 Forecasting accuracy

To test the accuracy of our exponential smoothing state space (ESSS) model, 5.0 minute average solar irradiance data is used. There are 150 samples from 07:00 to 19:30 for each day. Every 5.0 minute step is predicted and compared with the actual irradiance data to calculate the nRMSE. The test is repeated over the whole month and then the average nRMSE of that month is calculated. For comparison purposes, four other well-established forecasting methods, namely Autoregressive integrated moving average (ARIMA) model, linear exponential smoothing model (LES), simple exponential smoothing (SES) model and random walk (RW), are also tested in the same way. The benchmark RW model is persistence with white noise. Even though the performances of RW and persistence are similar, using RW model instead of persistence is to address the randomness in high variability solar irradiance. All the test results are listed in Table 3.5 and Table 3.6.

The ARIMA is implemented using forecast package in R. The specific ARIMA model is chosen automatically. The parameters used are: max.p=5, max.q=5, max.d=2, max.P=2, max.Q=2, max.order=5, ic=AIC, test=KPSS. The LES model parameters are: $\alpha = 0.5$, $\beta = 0.5$. The SES model $\alpha = 0.5$.

Table 3.5 shows that the ESSS model has generally better prediction accuracy than other time series models in Singapore. Although the SES model performs better in January and March 2011, the ESSS model is behind by less

Table 3.5: nRMSE (%) comparison among 5 forecasting methods for SERIS data

Forecast Period	**ESSS**	**ARIMA**	**LES**	**SES**	**RW**
2010 October	**17.40**	20.95	20.47	20.98	23.52
2010 November	**21.59**	24.00	23.31	23.69	26.07
2010 December	**27.77**	29.77	28.72	29.26	32.20
2011 January	33.71	33.62	33.89	**33.49**	37.55
2011 February	**29.15**	30.37	30.44	31.00	35.23
2011 March	33.03	33.60	34.43	**32.84**	34.85
2011 April	**29.84**	31.36	30.55	30.14	35.95
2011 May	**18.55**	22.78	22.48	22.37	25.59
2011 June	**19.64**	23.44	22.73	22.42	26.00
2011 July	**20.80**	23.46	23.05	22.56	27.22
2011 August	**21.31**	24.90	24.32	24.27	28.33

than 0.5%. By comparing with the benchmark RW model, we infer that the solar irradiance variability is high from December 2010 to April 2011, since the RW nRMSEs are all above 30%. The performance of the ESSS model may decrease in these months. In other months, however, the ESSS model outperforms other forecasting models.

Table 3.6 shows that the ESSS model performs well compared with other time series models in Colorado, US. The solar irradiance variability in this area is generally smaller than that in Singapore due to the difference in latitude. The peak variability occurs in summer months like July and August 2011, when the ESSS model accuracy is slightly less accurate than the other models.

In general, the ESSS model has better forecasting accuracy over other time series forecasting models in both Singapore and Colorado, US. The performance of different models can be influenced by the solar irradiance variability

Table 3.6: nRMSE (%) comparison among 5 forecasting methods for Colorado data

Forecast Period	**ESSS**	**ARIMA**	**LES**	**SES**	**RW**
2010 October	**16.86**	18.86	18.97	19.98	20.22
2010 November	**12.76**	13.80	13.85	13.47	15.49
2010 December	**15.37**	17.96	17.64	17.00	19.14
2011 January	**11.51**	13.58	13.67	13.17	14.11
2011 February	**9.75**	11.04	10.78	10.46	11.38
2011 March	**15.17**	17.24	17.50	16.08	17.08
2011 April	**15.12**	17.21	17.10	16.98	17.86
2011 May	**18.10**	19.22	19.16	19.02	20.22
2011 June	**19.86**	20.90	20.91	20.72	21.91
2011 July	29.04	**28.93**	29.14	29.02	29.19
2011 August	24.25	24.40	24.24	24.06	**24.00**

in the region.

The performances of the short-term forecasting models are also compared using 5-minute solar irradiance data in Singapore for the whole year of 2015. The nRMSE comparison is shown in Figure 3.4. The nMBE comparison is shown in Figure 3.5. Among all the statistical models available for short-term forecasting, ESSS model has the lowest error in most of the months. It is also obvious that ESSS is not consistently biased to either positive or negative values.

3.3.2 Forecasting interval

The state space model of exponential smoothing provides the framework for computing prediction intervals. Since the prediction confidence interval is useful for power station managers and grid operators, the accuracy of the forecasting confidence interval is tested. The forecasting confidence interval

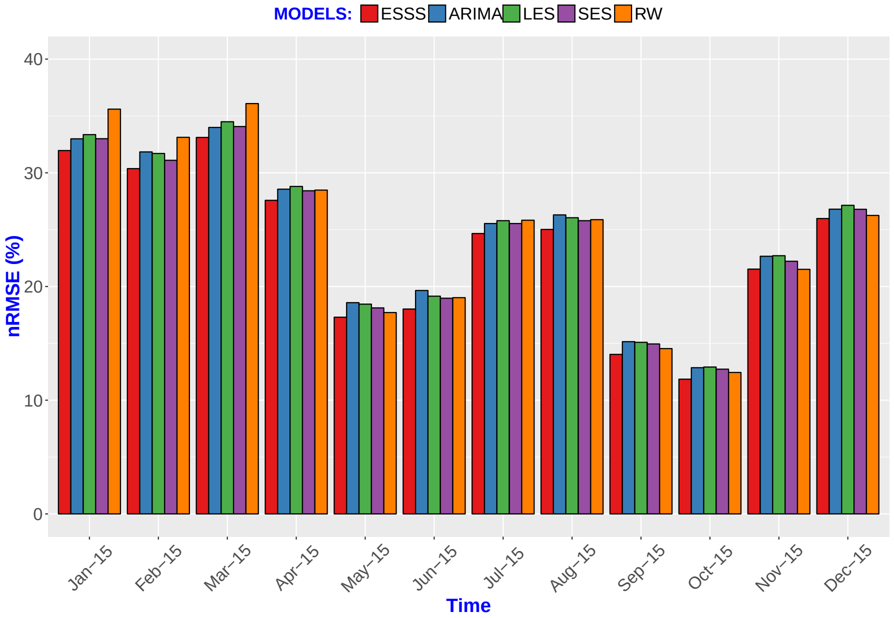

Figure 3.4: nRMSE (%) comparison of 5 forecasting methods for 5-minute Singapore data in 2015

is an estimate of an interval in which the future forecasting values will fall with a certain probability. In this test, accuracy is calculated by the ratio of forecasting points fall within the confidence interval, to the total number of forecasting points. The result is shown in Table 3.7. The theoretical 95% confidence interval usually gives us forecasting accuracy around 90%, which is an acceptable forecasting range for industrial application.

Figure 3.6 and Figure 3.7 illustrate the forecasting interval examples for a day with relatively smooth irradiance and a relatively spiky day. It is seen that large variations of the solar irradiance would expand the confidence interval which is expected.

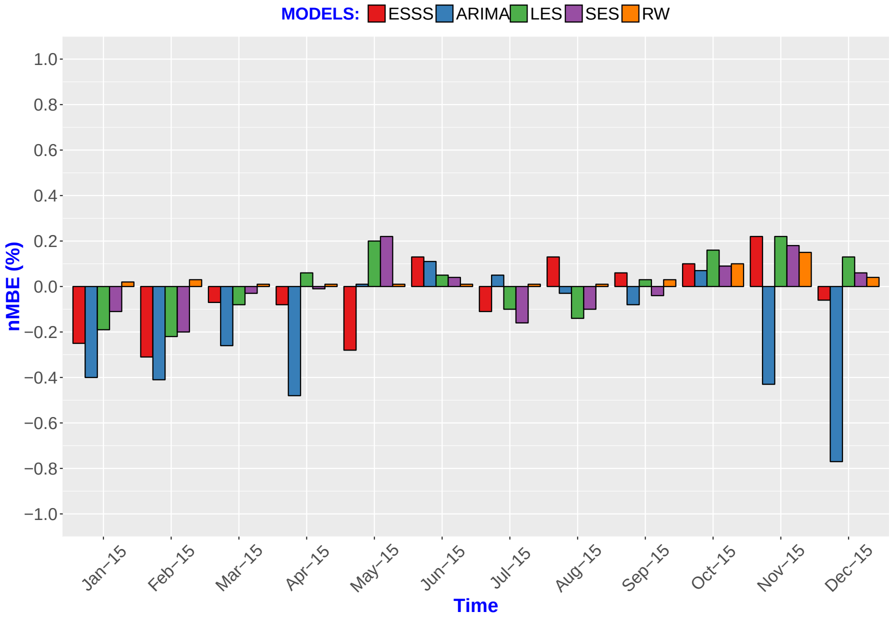

Figure 3.5: nMBE (%) comparison of 5 forecasting methods for 5-minute Singapore data in 2015

3.3.3 Forecasting horizon

In the previous sections, 5.0 minute average solar irradiance data is used to test the performance of different time series forecasting models. In real applications, different time series forecast horizons must be tested in order to meet various forecasting requirements from the power grid managers. It is also useful to determine the best measurement dataset to be used at a certain forecast horizon. We have made use of the SERIS data ranging from 5.0 minute averages to 60 minute averages, to forecast from 5.0 minutes up to 60 minutes. The nRMSE maps of four different time series models are shown in Figure 3.8. The nRMSE value is displayed using colours. Clearly, the ESSS model exhibits the best performance when using less than 20 minute average data to predict less than 20 minutes ahead.

Table 3.7: ESSS 95% confidence interval accuracy(%)

Forecast Period	**Singapore**	**Colorado**
2010 October	92.67	91.45
2010 November	93.33	94.67
2010 December	94.00	86.67
2011 January	91.67	89.00
2011 February	87.33	88.00
2011 March	86.67	91.87
2011 April	91.67	89.80
2011 May	89.02	96.00
2011 June	89.72	87.25
2011 July	91.02	87.33
2011 August	92.25	91.33

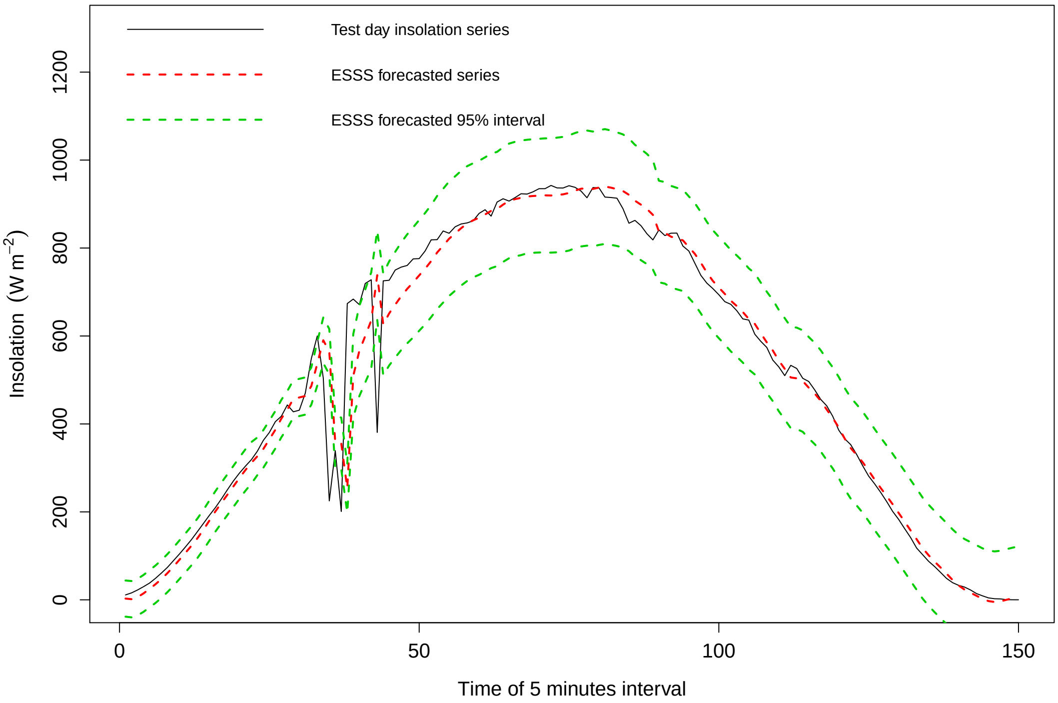

Figure 3.6: The ESSS forecast plot for relatively smooth day.

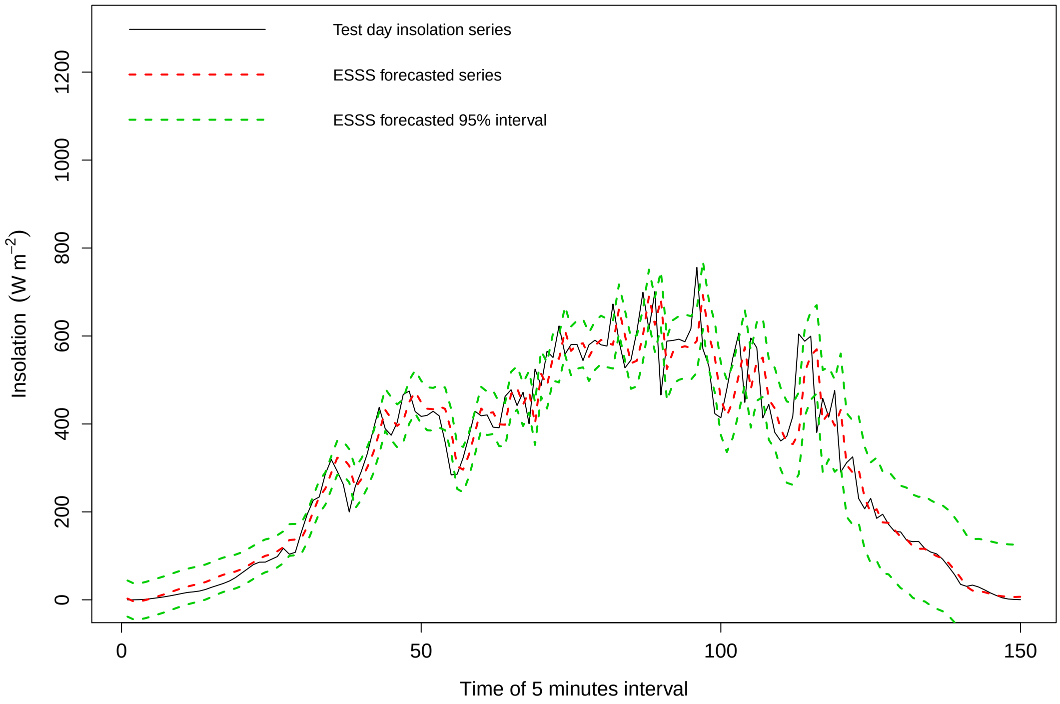

Figure 3.7: The ESSS forecast plot for relatively spiky day.

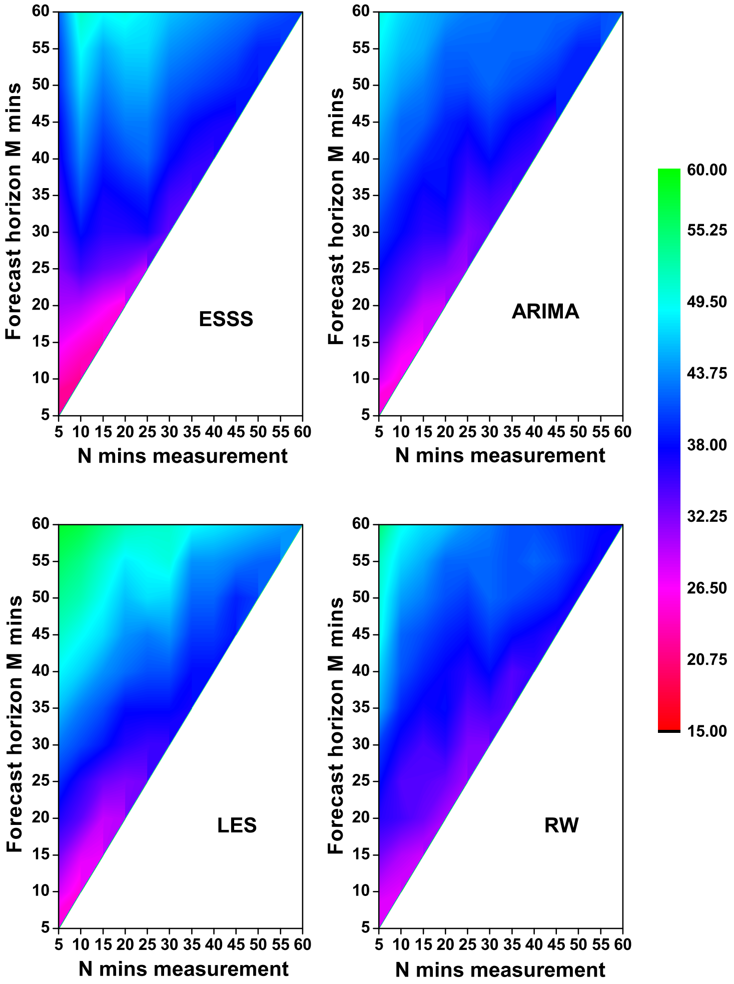

Figure 3.8: The forecast horizon nRMSE map

Chapter 4

Solar irradiance forecasting using novel hybrid statistical analysis and machine learning

Cloud cover is the most attenuating factor of solar irradiance. Solar irradiance forecasting would be improved by predicting the cloud cover. Some researchers study the cloud cover by observing the portion of the cloud covering the sky and classifying them into cloud cover index (Robaa, 2008; Yang, Jirutitijaroen, and Walsh, 2012a). Cloud cover has also been studied using satellite images. Researchers have developed methods to estimate solar irradiance from satellite images (Yang et al., 2013).

4.1 Data

The satellite images we have used are from the geostationary weather satellites of Japan Meteorological Agency (JMA). The current satellite in operation is called Multifunctional Transport Satellites (MTSAT) 2, also known as

Himawari-7, which operates at 35,800 km above the equator at 145 degrees East longitude, from 2010 to 2015. This satellite carries an imaging telescope of five channels: one visible ($550 - 880$ nm), 2 IR ($10,300 - 12,500$ nm), one IR/WV ($6,500 - 7,000$ nm) and one NIR ($3,500 - 4,000$ nm).

The solar irradiance time series dataset we have used is from the meteorological station of the Solar Energy Research Institute of Singapore (SERIS) located at ($1.30°N$, $103.77°E$) and the elevation is about 50 meters above sea level. The pyranometer used in this station is a meteorological class Delta-T SPN1 Sunshine Pyranometer[1]. Located just 1.0 degrees north of the equator, Singapore enjoys a tropical climate with an average daily temperature between 25 degrees Celsius and 31 degrees Celsius, and relative humidity of $70\% - 80\%$. Rainfall occurs almost every day but usually only for a short period of time. The high temperature and high humidity levels lead to high evaporation which causes frequent cloud formation and dense cloud cover. Therefore the solar irradiance variability is high in Singapore.

4.2 Forecasting methodology

This section details the steps in implementing our prediction model. First, satellite images are analysed and cloud cover index is derived using self-organising map. Second, the exponential state space model is introduced. Finally, the back propagation multilayer perceptron model is discussed.

4.2.1 Satellite image analysis

Before detecting cloudy pixels from satellite images, the grey levels of the raster image are converted into reflectance and temperature using MTSAT

---

[1] `http:\delta-t.co.uk`

calibration algorithm provided by the Meteorological Satellite Centre (MSC) of JMA (Meteorological Satellite Center (MSC), Japan Meteorological Agency (JMA), 2013). After the pixel values are converted to physical value, multiple threshold tests are applied to the images. Reflectance and temperature pixel values as well as the algebraic combination of them can be compared with different thresholds to identify the cloud cover index. A land-sea-coast raster image mask is also generated to modify the thresholds according to the underlying surface.

Two main threshold tests are used in this analysis, namely the visible reflectance threshold test and infra-red temperature threshold test. For the visible reflectance threshold test, one year of image data has been used to generate monthly synthetic raster image of surface albedo. Every pixel reflectance from the whole image has been recorded and the most repeated value should be the surface albedo, assuming the clouds have wide spectrum of reflectance values and the surface albedo has a rather constant reflectance. Finally the values within the reasonable albedo interval, which defines as [0.1,0.4] for land and [0.0,0.3] for sea, are taken as the surface albedo. For the infra-red temperature threshold test, the monthly synthetic raster images of surface temperature are generated using two temperature sources, namely the monthly mean minimum sea surface temperature and monthly mean minimum land temperature from National Environment Agency of Singapore. Linear interpolation and nearest neighbour extrapolation has been implemented to fill the pixel without values. The infra-red channel temperature values are then compared with the monthly mean minimum surface temperature for each pixel. If temperature is lower than the minimum values minus an offset, pixel is marked as cloudy.

The derivation of cloud cover index is based on the quantitative determination of pixel opaqueness, which indicates the level of solar irradiance obstruction. In the visible channel satellite image, opaque clouds reflect more solar irradiance than thin clouds. Thus the reflectance of opaque clouds have high values. However, the exact degree of opaqueness is hard to determine. Therefore we make use of a neural network pattern classification technique, namely the self-organising maps (SOM), to automatically classify the cloud coverage over Singapore into 20 levels $(0-19)$ of cloud cover index.

4.2.1.1 Self-organising maps

Neural network learning is a process by which the free parameters of a neural network are adapted through a process of stimulation by the environment in which the network is embedded. The type of learning is determined by the manner in which the parameter changes take place. There are three steps in the process of learning. First the neural network is stimulated by an environment. Second the neural network undergoes changes in its free parameters as a result of this stimulation. Finally the neural network responds in a new way to the environment because of the changes that have occurred in its internal structure.

SOM is one of the most effective neural network learning techniques. The self-organising process of SOM is derived from human brain cortex's local ordering of feature-sensitive cortical cells. The principle of topographic map formation behind SOM is that the spatial location of an output neuron in a topographic map corresponds to a particular domain or feature of data drawn from the input space. To achieve this topology-conserving mapping, SOM is constructed using two layers: input layer and output (map) layer. The two layers are fully connected. A topology is thus defined on the output layer. The principle goal of the SOM is to transform an incoming signal pattern of arbitrary dimension into a two dimensional discrete feature map, and to perform this transformation adaptively in a topologically ordered fashion.

To implement the SOM, the weights connecting all the input neurons and the output neurons are randomly initialised. The input vector is then selected from the training set. The next step is the competitive process, which a continuous input space of activation patterns is mapped onto a discrete output space of neurons by a process of competition among the neurons in the network. The best-matching neuron is the one whose weight vector has smallest Euclidean distance from the input vector.

$$O(x) = \arg\min_j ||x - w_j|| \tag{4.1}$$

where $O(x)$ is the best-matching neuron to input vector x and w_j is a weight vector for any output neuron j associated with input vector x. After the best-matching neuron is determined, it is located at the centre of a topological neighbourhood of cooperating neurons. From neurobiology, a firing neuron tends to excite the neuron in its immediate neighbourhood more than those farther away from it. This topological neighbourhood is symmetric about the maximum point and the amplitude of the topological neighbourhood decreases monotonically with increasing lateral distance. The topological function used in this model is shown below.

$$\begin{aligned} E_{j,O(x)}(t) &= \exp(-\frac{d_{j,O}^2}{2\sigma(t)^2}) \qquad t = 0, 1, 2, ... && (4.2) \\ \sigma(t) &= \sigma_0 \exp(-\frac{t}{\tau_1}) && (4.3) \end{aligned}$$

where $E_{j,O(x)}(t)$ is a measure of the effectiveness of the $O(x)$ on its neighbours and $d_{j,O}^2$ is the Euclidean distance from the neuron j to the $O(x)$ at time t. $\sigma(t)$ is the time-varying effective width of the topological neighbourhood. σ_0 is the initial effective width and τ_1 is the time constant. The final step is the adaptive process. The adaptation function is defined in the following equation.

$$w_j(t+1) = w_j(t) + \eta(t) E_{j,O(x)}(t)(x - w_j(t)) \qquad t = 0, 1, 2, ... \tag{4.4}$$

$$\eta(t) = \eta_0 \exp(-\frac{t}{\tau_2}) \tag{4.5}$$

where $\eta(t)$ is the learning-rate parameter decreasing with time. τ_2 is another time constant to control the decay rate of the learning rate. Upon repeated presentations of the training data, the synaptic weight vector tend to follow the distribution of the input vectors due to the neighbourhood updating. The algorithm leads to a topological ordering of the feature map in the sense that neurons that are adjacent in the lattice will tend to have similar synaptic weight vectors. By using SOM, cloud cover index is effectively classified into 20 levels.

4.2.2 Hybrid forecasting model

After analysing the satellite images, the derived cloud cover index is predicted using the ESSS model and the solar irradiance is estimated based on the predicted cloud cover index using back propagation multi-layer perceptron. The overall structure of the hybrid model is shown in Figure 4.1.

4.2.2.1 Back propagation multi-layer perceptron

The multi-layer perceptron used in this model consists of an input layer, a hidden layer of computational nodes and an output of computational nodes. For each neuron in the hidden layer, hyperbolic tangent sigmoid transfer function is used as activation function.

$$\varphi(x) = \tanh(x) = \frac{e^x - e^{-x}}{e^x + e^{-x}} \tag{4.6}$$

where $\varphi(x)$ is the transfer function. For the output neuron, linear transfer function is used as activation function.

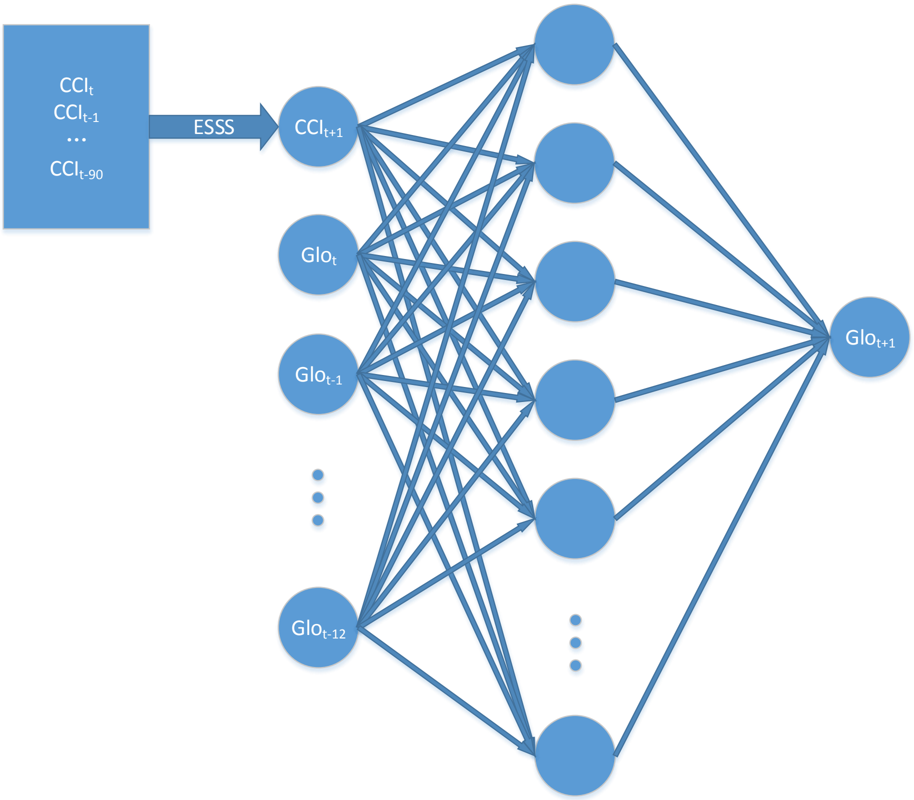

Figure 4.1: The overall structure of the hybrid model

Back propagation algorithm is used as the training algorithm. There are two passes of computation for the back propagation algorithm, namely forward pass and backward pass. The forward pass is the computation of transfer function signals for each neuron. For the backward pass, the process starts at the output layer, recursively compute the error function for each neuron from output layer towards the first hidden layer. At each layer, the synaptic weights are changed accordingly to the weight updating rule. The weight updating rule is shown in the following equations:

$$\begin{aligned} w_{ji}^{(s)}(n+1) &= w_{ji}^{(s)}(n)+\eta\delta_j^{(s)}(n)x_{out,i}^{(s-1)}(n) && (4.7)\\ \delta_j^{(s)}(n) &= (d(n)-x_{out,j}^{(s)}(n))\varphi^{(s)\prime}(v_j^{(s)}(n)) \text{ (output layer)} && (4.8)\\ &\text{or} \\ \delta_j^{(s)}(n) &= (\sum_{k=1}^{n_{s+1}}\delta_k^{(s+1)}(n)w_{kj}^{(s+1)}(n))\varphi^{(s)\prime}(v_j^{(s)}(n)) \text{ (hidden layer)} && (4.9)\end{aligned}$$

where s is the layer number, i is the neuron number for the current layer, j is the neuron number for the previous layer, η is the learning rate, $\delta(n)$ is the error function, $v(n)$ is the input of transfer function, $x_{out}(n)$ is the output of transfer function and $d(n)$ is the desired output value. For the training mode, batch training with Levenberg-Marquardt algorithm (LMA) is used in the model. LMA is one of the stabilized Newton and Gauss-Newton algorithms, which interpolates between the Gauss-Newton algorithm and the method of gradient descent. The LMA is a robust second order method for non-linear optimization, which is capable of finding a solution with starting point far off the minimum value.

To minimize the neural network structure, singular value decomposition (SVD) is used to estimate the number of hidden neurons. Singular value decomposition is commonly found in statistical signal processing approaches and subspace modelling. For an $N \times n$ matrix H, matrix factorization is performed.

$$H_{N\times n} = U_{N\times N}\Sigma_{N\times n}V_{n\times n}^T \tag{4.10}$$

$$\Sigma = \begin{bmatrix} \sigma_1 & 0 & \cdots & 0 \\ 0 & \sigma_2 & \cdots & 0 \\ \vdots & \vdots & \ddots & \vdots \\ 0 & 0 & \cdots & \sigma_k \end{bmatrix} \tag{4.11}$$

where U and V are orthogonal matrices and $\sigma_1 \geq \sigma_2 \geq \cdots \geq \sigma_k > 0$ are the singular values of the matrix H. The SVD can be used to determine the effective rank of the matrix H.

$$Rank(H_{m\times n}) = k \tag{4.12}$$

For the training set, there are N training samples and each sample is an M-dimensional vector. Then the outputs of the hidden neurons for each training sample input vector $x(k)$ can be calculated.

$$h_{ki} = f_i(\sum_{j=1}^{M} w_{ij}x_j(k) + b_i) \in H \tag{4.13}$$

where b_i is the bias. Then the matrix $H_{N\times n}$ consists of N training samples and n hidden neurons, which describes the outputs of the hidden neurons for all the training samples. If the MLP is too large, there must be some redundant information in the matrix H, which indicates that some columns are almost linearly independent. To reduce these redundant hidden neurons, a pruning criterion is selected to obtain the effective rank of the H

$$min_k(\frac{\sum_{i=1}^{k}\sigma_i}{\sum_{i=1}^{n}\sigma_i}) \geq 99\% \tag{4.14}$$

where k is the new number of hidden neurons. This is procedure is repeated until k is converged.

The multi-layer neural network is trained using previous one-year data including solar irradiance and ESSS forecasted cloud cover index. Once the model is trained, the neural network structure is kept the same to make all the hourly forecasts in the test year.

4.3 Application of the proposed model

The first application is based on the satellite images and solar irradiance time series data from Singapore. Since it is meaningless to forecast solar irradiance after sunset, we only investigate samples from 07:00 to 19:00.

4.3.1 Evaluation of errors

To evaluate the quality of the proposed model, three different types of error measurement are used, namely the normalized root mean square error (nRMSE), coefficient of determination (R^2) and the normalized mean bias error (nMBE)(Marquez and Coimbra, 2011). The three error types are calculated using the following equations:

$$nRMSE = \frac{\sqrt{E[(\widehat{X} - X)^2]}}{\sqrt{E[X^2]}} \tag{4.15}$$

$$R^2 = 1 - \frac{E[(\widehat{X} - X)^2]}{E[(X - \sqrt{E[X^2]})^2]} \tag{4.16}$$

$$nMBE = \frac{E[\widehat{X} - X]}{\sqrt{E[X^2]}} \tag{4.17}$$

where $\widehat{X}$ is the prediction from the forecasting model and X is the measured value of GHI in the training or test set. All the predicted values are true out-of-sample forecasts, in that they use only data prior to the start of the forecast horizon. The models are estimated over the data prior to the start of the forecast, the points of the next time step is forecast, and the forecast values are compared with the actual ones. The procedure is iterative until forecasts have been run over the daily data set. The satellite data and the SERIS data consists of twelve months from September 2010 to July 2011. For the satellite data, all the months except the month to be predicted are used as training set to derive the cloud cover index. Data from September 2010 is used to generate an average daily residual to fit in the initialization of our prediction model, in order to forecast the time series of the next month, i.e. October 2010. In the forecasting test after October 2010, the data from the previous month is used to form average daily residual initially fitting in the prediction model.

Table 4.1: nRMSE (%) comparison among 5 forecasting methods for SERIS data

Forecast Period	**Hybrid**	**ARIMA**	**LES**	**SES**	**RW**
2010 October	**28.19**	40.36	43.85	37.06	41.52
2010 November	**36.09**	43.66	48.00	42.28	50.00
2010 December	**29.16**	35.81	38.03	34.45	42.84
2011 January	**43.69**	50.62	51.35	49.72	58.28
2011 February	**20.65**	28.98	31.34	26.57	36.90
2011 March	**32.78**	43.60	44.10	36.38	40.56
2011 April	**29.65**	41.44	42.32	35.50	44.22
2011 May	**33.12**	42.29	44.87	39.29	48.22
2011 June	**36.41**	43.75	44.87	42.36	51.21
2011 July	28.57	28.15	31.52	**25.56**	35.20

4.3.2 Forecasting accuracy

To test the accuracy of our hybrid forecasting model, one hour average solar irradiance data is used. Every one hour step is predicted and compared with the actual irradiance data to calculate the errors. The test is repeated over the whole month and then the average errors of that month is calculated. For comparison purposes, four other well-established forecasting methods, namely Autoregressive integrated moving average (ARIMA) model, linear exponential smoothing model (LES), simple exponential smoothing (SES) model and random walk (RW), are also tested in the same way. All the test results are listed in Table 4.1 to Table 4.3.

Table 4.1 shows the normalized root mean square error comparison of the hourly solar irradiance forecasting accuracy of all the models. The best forecasting accuracy is shown in bold. It is clear that the hybrid model has better prediction accuracy than the other time series models in Singapore based

Table 4.2: R^2 comparison among 5 forecasting methods for SERIS data

Forecast Period	**Hybrid**	**ARIMA**	**LES**	**SES**	**RW**
2010 October	**0.845**	0.684	0.613	0.772	0.754
2010 November	**0.764**	0.596	0.492	0.607	0.467
2010 December	**0.811**	0.810	0.802	0.798	0.783
2011 January	**0.616**	0.432	0.479	0.485	0.349
2011 February	**0.908**	0.820	0.835	0.816	0.809
2011 March	**0.834**	0.681	0.627	0.815	0.776
2011 April	**0.863**	0.732	0.758	0.787	0.660
2011 May	**0.825**	0.595	0.576	0.632	0.503
2011 June	**0.792**	0.699	0.710	0.694	0.447
2011 July	0.874	0.857	0.801	**0.894**	0.775

Table 4.3: nMBE (%) comparison among 5 forecasting methods for SERIS data

Forecast Period	**Hybrid**	**ARIMA**	**LES**	**SES**	**RW**
2010 October	-1.81	-2.13	-0.96	-1.86	**0.17**
2010 November	-1.75	-2.48	-3.40	-2.84	**-0.09**
2010 December	-2.31	-1.21	-0.96	-1.61	**0.14**
2011 January	1.45	-3.59	-1.00	**-0.23**	0.39
2011 February	-0.68	-0.97	-5.17	**-0.01**	0.39
2011 March	1.38	-1.44	-2.67	-3.09	**-1.22**
2011 April	0.97	-2.71	-0.86	**-0.32**	-0.34
2011 May	-0.21	-0.81	-0.79	-1.43	**-0.13**
2011 June	-0.54	-1.47	-0.67	-0.31	**-0.16**
2011 July	-0.25	-0.85	-0.96	**-0.18**	-0.42

on nRMSE. From October 2010 to June 2011, the hybrid model consistently outperforms all other comparison models. In October 2010, the proposed model improves at least 9% from other models. On average the forecasting accuracy of the proposed model is 6% better than the best prediction accuracy of all other statistical time series models. It is important to note that from November 2010 to January 2011, Singapore faces north-east monsoon. The rainfall is very often in these months and intermittent rainfall leads to high variability in the cloud formation. The fast winds during the season cause the fast pace in cloud movements. All these factors will lead to high variability in short-term solar irradiance. In these months, it is very difficult to achieve a satisfying forecasting accuracy.

Only in July 2011, the SES model and ARIMA model perform better than the proposed model. The main reason for the worse performance in July 2011 is that there were quite a few missing satellite images in this month. Even though linear interpolation is implemented to deal with the missing data, the accuracy to derive the cloud cover index is still affected. With inaccurate cloud cover index, the prediction accuracy is decreased as expected.

Table 4.2 shows the R^2 comparison of the hourly solar irradiance forecasting accuracy of all the models. By comparing Table 4.1 and Table 4.2 we can observe that the results of coefficient of determination matches the result of normalized root mean squared error, which substantiate our analysis.

Table 4.3 shows the normalized mean bias error comparison of the hourly solar irradiance forecasting accuracy of all the models. The bias errors for all the models are generally less than 3% with a few exceptions. The small bias errors indicate that there is no particular bias in all the forecasting models. It is expected that the benchmark RW model has the smallest bias error for most of the times since it is based on persistence.

4.3.3 Computational complexity

The hybrid model is implemented based on Theano library in Python. Theano is designed to define, optimize, and evaluate mathematical expressions involving multi-dimensional arrays efficiently. The parallel computational structure of Theano allows us to have fast training time even with a quad-core 3.5GHz personal computer. For one year hourly training data, the hybrid model training can be finished within 15 minutes. The major part of the training time (about 10 minutes) is consumed in the satellite image processing (SOM) part. The forecasting stage (ESSS+MLP) can be finished within 5 minutes.

Chapter 5

Solar irradiance forecasting using novel machine learning

For the statistical time series methods, there are two major issues in the modelling process, namely noise and stationarity. In the context of time series modelling, noise is characterized by the absence of complete characteristic information from the historical data of the time series to appropriately identify the correlation between historical data and predicted data (Box, Jenkins, and Reinsel, 1970). Problems like over-fitting or under-fitting are the possible consequences of noise existing in the time series. As a result, the performance of the trained model is poor when applied to test data. A time series $\{r_t\}$ is said to be strictly stationary if the joint distribution of $(r_{t_1}, \ldots, r_{t_k})$ is identical to that of $(r_{t_1+t}, \ldots, r_{t_k+t})$ for all t, where k is an arbitrary positive integer and $(r_{t_1}, \ldots, r_{t_k})$ is a collection of k positive integers (Box, Jenkins, and Reinsel, 1970). This simply means the joint distribution of the time series remains unchanged under time shift. However, this condition is hard to verify empirically: thus a weaker version of stationarity is usually applied. A time series $\{r_t\}$ is considered weakly stationary if both the mean of r_t and the covariance between r_t and r_{t-l} are time invariant, where l is an arbitrary integer. In real applications, with N observed data points, weak stationarity implies that the time plot of the data would show that these N values fluctuate with constant variation around a fixed level. Weak stationarity is generally sufficient to predict future observations (Brown, 1963). However, even weak stationarity is difficult to obtain in solar irradiance forecasting since the trend in the daily solar irradiance is hard to capture when there is large variability. The non-stationarity characteristic in the solar irradiance implies the dynamics between different time series regions varies, which changes the correlation between past and future. This dynamic changing process is hard for a single time series model to capture. Moreover, the noise level varies in different time series input regions. A single time series model could encounter local under-fitting or over-fitting problems extracting features from regions with various noise levels.

In order to resolve these complex problems, we propose a hybrid approach based on self-organizing map (SOM), support vector regression (SVR) and particle swarm optimization (PSO). SOM is applied to partition the whole input space into several disjointed regions with different characteristic information on the correlation between the input and the output. Then SVR is used to model each disjointed regions to identify the characteristic correlation. In order to reduce the performance volatility of SVM with different parameters, PSO is implemented to automatically perform the parameter selection in SVR modelling. Figure 5.1 shows the overall structure of the hybrid model.

5.1 Data

The first set of solar irradiance time series data is from a rooftop station in South Park, Colorado, USA located at ($9.16°N$, $105.37°W$) and the elevation is about 3000 meters above sea level (Measurement and Instrumentation

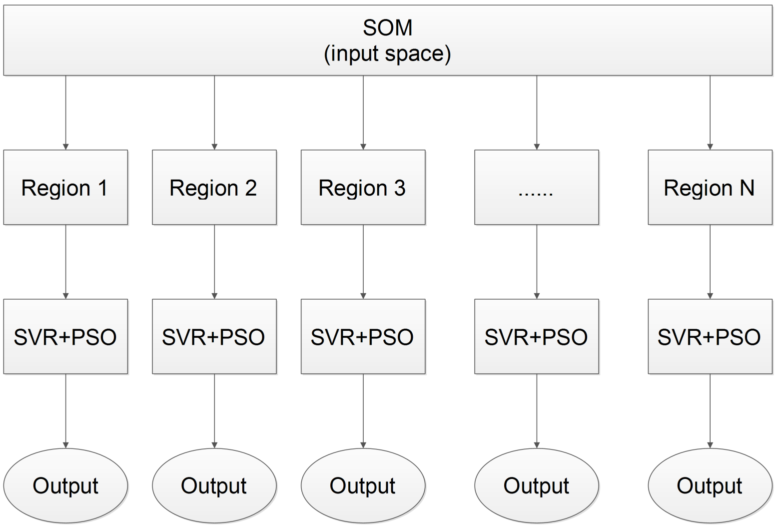

Figure 5.1: The overall structure of the hybrid model

Data Center (MIDC), NREL, 2012). The pyranometer used in this station is a LI-200 LI-COR Pyranometer which compares favorably with first class thermopile-type pyranometers[1]. The climate of South Park is semi-arid with low humidity and low precipitation. The solar irradiance variability is moderate and typical for the temperate zone.

The second set of solar irradiance time series data we have used is from the meteorological station of the Solar Energy Research Institute of Singapore (SERIS) located at ($1.30°N$, $103.77°E$) and the elevation is approximately 50 meters above sea level. The pyranometer used in this station is a meteorological class Delta-T SPN1 Sunshine Pyranometer[2]. Located just 1.0 degrees north of the equator, Singapore enjoys a tropical climate with an average daily temperature between 25 degrees Celsius and 31 degrees Celsius, and relative

---

[1] `http://www.licor.com/pyranometer`

[2] `http://delta-t.co.uk`

humidity of $70\% - 80\%$. Rainfall occurs almost every day but usually only for a short period of time. The high temperature and high humidity levels lead to high evaporation which causes frequent cloud formation and dense cloud cover. Therefore the solar irradiance variability is high in Singapore.

5.2 Forecasting methodology

This section details the steps in implementing our prediction model. First, self-organizing map is applied to partition the whole input space into several disjointed regions with different characteristic information on the correlation between the input and the output. Second, support vector regression is used to model each disjointed regions to identify the characteristic correlation. Finally, the implementation of particle swarm optimization in SVR parameter selection is discussed.

5.2.1 Self-organising maps (SOM)

Neural network learning is a process by which the free parameters of a neural network are adapted through a process of stimulation by the environment in which the network is embedded. The type of learning is determined by the manner in which the parameter changes take place. There are three steps in the process of learning. First the neural network is stimulated by an environment. Second the neural network undergoes changes in its free parameters as a result of this stimulation. Finally the neural network responds in a new way to the environment because of the changes that have occurred in its internal structure.

SOM is one of the most effective neural network learning techniques (Kohonen, 2013). The self-organising process of SOM is deliberately analogous to the form human brain cortex's local ordering of feature-sensitive cortical cells. The principle of topographic map formation behind SOM is that the spatial location of an output neuron in a topographic map corresponds to a particular domain or feature of data drawn from the input space. To achieve this topology-conserving mapping, SOM is constructed using two layers: an input layer and an output (map) layer. The two layers are fully connected. A topology is thus defined on the output layer. The principle goal of the SOM is to transform an incoming signal pattern of arbitrary dimension into a two dimensional discrete feature map, and to perform this transformation adaptively in a topologically ordered fashion.

To implement the SOM, the weights connecting all the input neurons and the output neurons are randomly initialised. The input vector is then selected from the training set. The next step is the competitive process, in which a continuous input space of activation patterns is mapped onto a discrete output space of neurons by a process of competition among the neurons in the network. The best-matching neuron is the one whose weight vector has smallest Euclidean distance from the input vector.

$$O(x) = \arg\min_{j} \|x - w_j\| \tag{5.1}$$

where $O(x)$ is the best-matching neuron to input vector x and w_j is a weight vector for any output neuron j associated with input vector x. After the best-matching neuron is determined, it is located at the centre of a topological neighbourhood of cooperating neurons. From neurobiology, a firing neuron tends to excite the neuron in its immediate neighbourhood more than those farther away from it. This topological neighbourhood is symmetric about the maximum point and the amplitude of the topological neighbourhood decreases monotonically with increasing lateral distance. The topological function used in this model is shown below.

$$\begin{aligned} E_{j,O(x)}(t) &= \exp\left(-\frac{d_{j,O}^2}{2\sigma(t)^2}\right) \qquad t = 0, 1, 2, ... &(5.2)\\ \sigma(t) &= \sigma_0 \exp\left(-\frac{t}{\tau_1}\right) &(5.3)\end{aligned}$$

where $E_{j,O(x)}(t)$ is a measure of the effectiveness of $O(x)$ on its neighbours and $d_{j,O}^2$ is the Euclidean distance from the neuron j to the $O(x)$ at time t. $\sigma(t)$ is the time-varying effective width of the topological neighbourhood. σ_0 is the initial effective width and τ_1 is the time constant. The final step is the adaptive process. The adaptation function is defined in the following equation.

$$\begin{aligned} w_j(t+1) &= w_j(t) + \eta(t)E_{j,O(x)}(t)\,(x - w_j(t)) \qquad t = 0, 1, 2, ... &(5.4)\\ \eta(t) &= \eta_0 \exp\left(-\frac{t}{\tau_2}\right) &(5.5)\end{aligned}$$

where $\eta(t)$ is the learning-rate parameter decreasing with time. τ_2 is another time constant to control the decay rate of the learning rate. Upon repeated presentations of the training data, the synaptic weight vector tends to follow the distribution of the input vectors due to the neighbourhood updating. The algorithm leads to a topological ordering of the feature map in the sense that neurons that are adjacent in the lattice will tend to have similar synaptic weight vectors.

As an unsupervised clustering algorithm based on competitive learning, SOM can effectively classify the input data with similar characteristic into the same region. Within each region, the distribution becomes more uniform than the whole input data space. Therefore the classification facilitates SVR to obtain the more stationary characteristic correlation between input and output.

Since the exact number of regions cannot be determined before the training procedure, a tree-structured architecture is adopted from (Abdel Hady, Schwenker, and Palm, 2010) to partition the input space. This structure partitions the input space into two regions recursively until a certain terminal condition is met. Without predetermine the total number of classification regions, a suitable size and structure for partitioning the input space can be determined automatically by specifying a terminal condition.

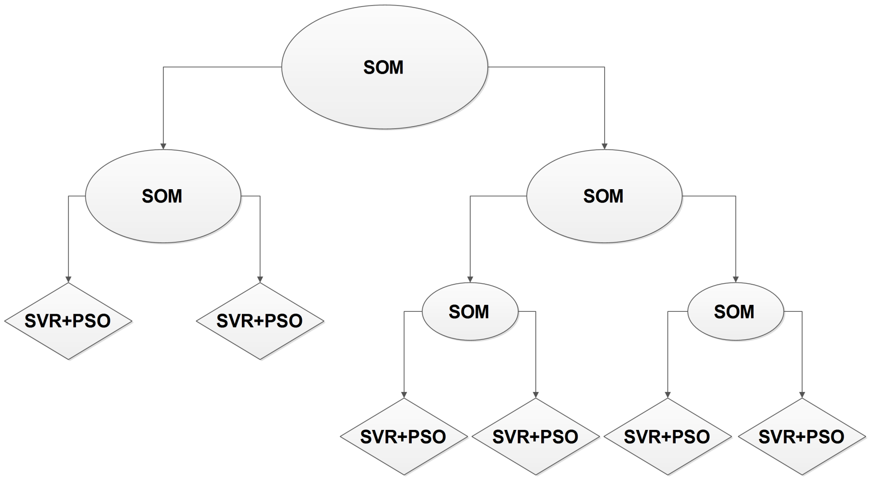

Figure 5.2: The tree-structured architecture of the training procedure

As an example shown in Figure 5.2, SOM is applied in each node to partition the input sample space into two smaller regions recursively until the terminal condition is met. At end-nodes or leaves, SVR and PSO are used to solve each partitioned region. The detailed description of the tree-structured learning algorithm is listed as follows.

1. Set the training data set as an end-node and determine a threshold number N as the minimum number of data points in each end-node.
2. Input the data set at the end-node to SOM which will classify the data

set into two non-overlapping subsets.

3. Count the number of data points in each subset and compare with N. If the number of data points is larger than N in both subsets, the former end-node is converted to a normal node and the two subsets are indicated as end-nodes. Otherwise, merge the two subsets back to the former end-note and stop.
4. Repeat step 2 to 3 until the classification stops in all the nodes.
5. Train SVR with PSO using the data set in each end-node.

5.2.2 Support vector regression (SVR)

The SVR model makes use of support vector classifiers to apply in regression and time series prediction (Smola and Scholkopf, 2004). The basic principle of SVR can be described in a linear formulation and then generalized to a non-linear algorithm which is applied in this chapter.

Given a set of training data $\{(\mathbf{x}_i, y_i)\}_{i=1}^{N} \in \mathbb{R}^n \times \mathbb{R}$, where $\mathbf{x}_i$ is the n-dimensional vector, y_i is the output value and N is the number of the training data. Then a linear relation is defined as:

$$y = g(\mathbf{x}_i) = \mathbf{w}^T\mathbf{x}_i + b \quad \text{with} \quad \mathbf{w} \in \mathbb{R}^n, b \in \mathbb{R} \tag{5.6}$$

where $\mathbf{w}$ is the weight vector and b is the threshold coefficient. The goal is to find $g(\mathbf{x}_i)$ which has less than ε deviation from y_i and is as flat as possible. This leads to a minimization problem:

$$\min \quad \frac{1}{2}\|\mathbf{w}\| + C\sum_{i=1}^{N}[l(\xi_i) + l(\xi_i^*)] \tag{5.7}$$

$$\text{s.t.} \quad \begin{cases} y_i - g(\mathbf{x}_i) \leq \varepsilon + \xi_i \\ g(\mathbf{x}_i) - y_i \leq \varepsilon + \xi_i^* \\ \xi_i, \xi_i^* \geq 0 \end{cases} \tag{5.8}$$

where C is the trade-off coefficient which is always positive, ξ_i and ξ_i^* are slack variables and l is the loss function which is defined as:

$$l(\xi) = \begin{cases} 0 & \text{if } |\xi| \leq \varepsilon \\ |\xi| - \varepsilon & \text{otherwise} \end{cases} \tag{5.9}$$

After applying standard Lagrange multiplier techniques, we can get the support vector expansion:

$$w = \sum_{i=1}^{N} (\alpha_i - \alpha_i^*) \mathbf{x}_i \tag{5.10}$$

$$g(x) = \sum_{i=1}^{N} (\alpha_i - \alpha_i^*) \mathbf{x}_i^T \mathbf{x} + b \tag{5.11}$$

where α_i and α_i^* are Lagrange multipliers.

In order to achieve non-linearity, the training data pattern $\mathbf{x}_i$ can be mapped to a higher dimensional feature space:

$$\Phi : \mathbb{R}^n \rightarrow \mathbb{R}^{n+h}, \mathbf{x} \rightarrow \Phi(\mathbf{x}) \tag{5.12}$$

and we define the kernel as:

$$K(\mathbf{x}_i, \mathbf{x}_j) = \Phi(\mathbf{x}_i)^T \Phi(\mathbf{x}_j) \tag{5.13}$$

therefore we have:

$$g(x) = \sum_{i=1}^{N} (\alpha_i - \alpha_i^*) K(\mathbf{x}_i, \mathbf{x}) + b \tag{5.14}$$

The expression of the kernel can be chosen directly without knowing $\Phi()$ explicitly, on the condition that the chosen expression satisfies the Mercer's Condition (Mercer, 1909). In this study, the most widely used Gaussian kernel function is applied:

$$K(\mathbf{x}_i, \mathbf{x}) = exp\left(\frac{-\|\mathbf{x}_i - \mathbf{x}\|^2}{2\sigma^2}\right) \tag{5.15}$$

where σ is the kernel parameter which defines the structure of the high dimensional feature space.

The determination of the user-defined parameters (C, ε, σ) is crucial to the performance of the SVR. In order to improve the forecasting accuracy of the SVR, particle swarm optimization is applied to automatically and effectively choose these parameters.

5.2.3 Particle swarm optimization (PSO)

The PSO is selected as the parameter optimization algorithm due to the non-differentiable target function and no gradient information.

The PSO is a population based method for stochastic optimization of continuous non-linear functions. The development of the PSO algorithm was inspired by the social behaviours of bird flocking and fish schooling (Eberhart and Kennedy, 1995). The population of particles in the PSO is analogous to the birds and fish. Each particle is a potential solution in the searching space. By the end of the searching procedure, the optimal solution is defined by the particle with the smallest error.

In the searching procedure, a particle i ($i = 1, 2, ..., N$) is defined by a position vector $\mathbf{x}_i \in \mathbb{R}^n$, a velocity vector $\mathbf{v}_i \in \mathbb{R}^n$ and individual's best position $\mathbf{y}_i \in \mathbb{R}^n$ in an n-dimensional searching space. The initial positions and velocities are random for the N particles. Each particle's best position $\mathbf{y}_i$ can be determined by calculating the error in the objective function f. The position with the smallest error is the current best position for the particle i. The global best position $\mathbf{y}$ is the position with the smallest error of all $\mathbf{y}_i$. In each step of the searching procedure, each particle's position and velocity is adjusted based on the particle's best position and the global best position. By the end of the search, either a minimum error or a maximum number of iterations is achieved. The updating rules of the particle velocity and position are showing below:

$$\begin{aligned} \mathbf{v}_i^{l+1} &= \chi\left\{w\mathbf{v}_i^l + c_1\varphi_{1i}^l\left(\mathbf{y}_i^l - \mathbf{x}_i^l\right) + c_2\varphi_{2i}^l\left(\mathbf{y}^l - \mathbf{x}_i^l\right)\right\} && (5.16) \\ \mathbf{x}_i^{l+1} &= \mathbf{v}_i^{l+1} + \mathbf{x}_i^l && (5.17) \end{aligned}$$

where l denotes the lth iteration, χ is the velocity magnitude factor, w is the inertia weight coefficient, c_1 and c_2 are acceleration constants, φ_1 and φ_2 are random weights in the range $[0, 1]$ under normal distribution generated at each step for each particle component. The velocity magnitude factor χ is adopted to improve the convergence speed. The inertia weight coefficient w can determine the impact of previous velocity on the current velocity. Therefore a large w value can facilitate global exploration while a small w value leads to local exploration. To balance both exploration, a linearly decreasing inertia weight is applied here:

$$w(l) = w_{max} - l \times \frac{w_{max} - w_{min}}{L} \tag{5.18}$$

where l is the current iteration number, L is the maximum iteration number, w_{max} is the maximum inertia value and w_{min} is the minimum inertia value.

In our application, PSO is used to determine three parameters in the SVR model, namely the trade-off coefficient C, the deviation ε and the width parameter σ of the Gaussian kernel function. The PSO optimization process is shown in Figure 5.3 and the detailed description is listed as follows.

1. Initialize all the PSO parameters including particle dimension n, the position vector $\mathbf{x}_i$ and the velocity vector $\mathbf{v}_i$ of each particle, the velocity magnitude factor χ, the acceleration constants c_1 and c_2, the maximum number of iteration L and a fitness threshold FT.

2. Set the initialized position as the particle's best position $\mathbf{y}_i$ and the optimal individual position in the space as the global best position $\mathbf{y}$.

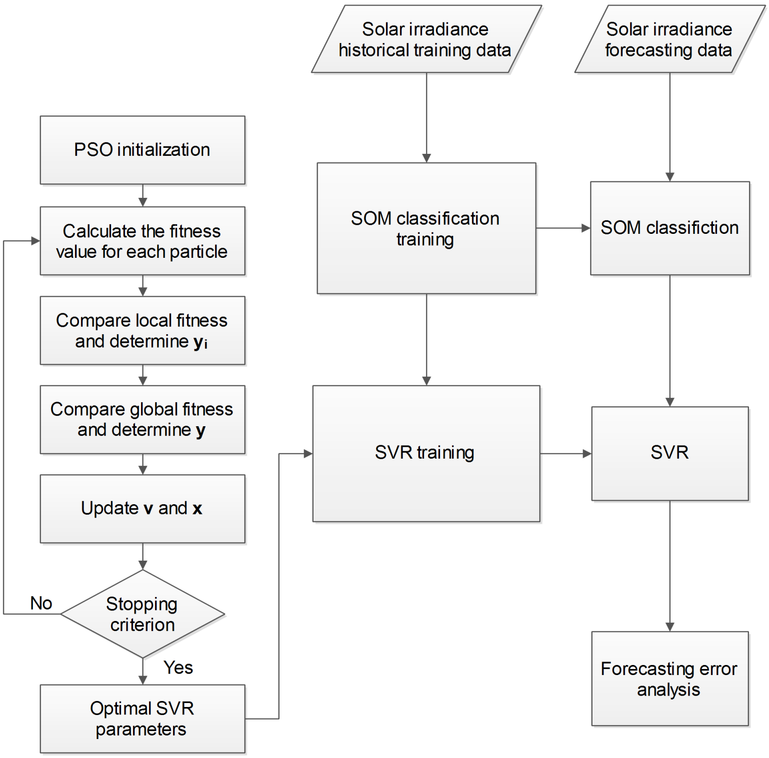

Figure 5.3: The overall flowchart of the hybrid forecasting model

3. Use K-fold cross validation method to evaluate fitness and adopt mean absolute percentage error (MAPE) as the fitness function:

$$\text{MAPE} = \frac{1}{m}\sum_{i=1}^{m}|\frac{Y - f(x)}{Y}| \tag{5.19}$$

where Y is the actual value, $f(x)$ is the output value and m is the number of the sample data.

4. Calculate the current fitness function value for each particle. Compare the current fitness function value with the particle's best position $\mathbf{y}_i$ to

determine the current local best position and then compare all the $\mathbf{y}_i$ to determine the current global best position $\mathbf{y}$.

5. Update position and velocity of each particle according to function 5.16-5.18 to search for a better solution.
6. Increase iteration number l by 1.
7. Stop the iteration if $l > L$ or fitness function value is less than FT and $\mathbf{y}$ is the optimal solution for the SVR parameters. Otherwise go to step 3.

The choice of PSO parameters are: $w_{max} = 0.8$, $w_{min} = 0.3$, $c_1 = 2.5$, $c_2 = 1.3$, $\chi = 1.1$, $n = 2$, $L = 400$, $N = 25$, $FT = 0.2$. The parallel computational time for optimizing a set of parameters is less than 30 seconds.

5.3 Application of the proposed model

Our application is based on the hourly solar irradiance time series data from South Park, Colorado, USA and Singapore. Since it is meaningless to forecast solar irradiance after sunset, we only investigate daytime samples from 04:00 to 20:00 in Colorado and 07:00 to 19:00 in Singapore.

5.3.1 Evaluation of errors

To evaluate the quality of the proposed model, two different types of error measurement are used, namely the normalized root mean square error (nRMSE) and the normalized mean bias error (nMBE)(Marquez and Coimbra, 2011). The two error types are calculated using the following equations.

$$nRMSE = \frac{\sqrt{E[(\widehat{X} - X)^2]}}{\sqrt{E[X^2]}} \tag{5.20}$$

$$nMBE = \frac{E[\widehat{X} - X]}{\sqrt{E[X^2]}} \tag{5.21}$$

where $\widehat{X}$ is the prediction from the forecasting model and X is the measured value of GHI in the training or test set.

All the predicted values are true out-of-sample forecasts, in that they use only data prior to the start of the forecast horizon. The models are estimated over the data prior to the start of the forecast, the points of the next time step are forecast, and the forecast values are compared with the actual ones. The procedure is iterative until forecasts have been run over the daily data set.

The Colorado data consist of 17 years from 1997 to 2013 and the SERIS data consist of 3 years from 2010 to 2013. All the months except the month to be predicted are used as the training set. During the training and testing procedure, past 8 hours' data are used as the input for the hour to be predicted.

5.3.2 Forecasting accuracy

To test the accuracy of our hybrid forecasting model, 1 h average solar irradiance data is used. Every 1 h step is predicted and compared with the actual irradiance data to calculate the errors. The test is repeated over the whole month and then the average errors of that month are calculated. For comparison purposes, four other well-established forecasting methods, namely Autoregressive integrated moving average (ARIMA) model, linear exponential smoothing model (LES), simple exponential smoothing (SES) model and random walk (RW), are also tested in the same way. All the test results are listed in Table 5.1 to Table 5.6. The column and bar charts of the test results are shown in Figure 5.4 to Figure 5.9.

Table 5.1 and Figure 5.4 show the normalized root mean square error comparison of the hourly solar irradiance forecasting accuracy of all the mod-

Table 5.1: nRMSE (%) comparison among 5 forecasting methods for Colorado data. The lowest values are indicated in bold.

Forecast Period	**Hybrid**	**ARIMA**	**LES**	**SES**	**RW**
2013 Jan	**23.44**	25.61	26.53	25.03	28.36
2013 Feb	**23.41**	26.39	26.17	26.01	30.18
2013 Mar	**24.03**	27.59	28.64	30.44	32.69
2013 Apr	**24.96**	29.11	33.49	30.89	35.10
2013 May	**23.11**	29.96	28.32	27.01	35.23
2013 Jun	**22.65**	28.64	28.63	29.17	34.84
2013 Jul	**24.84**	31.21	32.00	33.92	37.94
2013 Aug	**23.33**	30.49	30.97	29.96	34.90
2013 Sep	**23.98**	27.45	29.85	28.73	31.97
2013 Oct	**22.77**	26.13	29.10	28.42	30.20

Table 5.2: R^2 comparison among 5 forecasting methods for Colorado data. The highest values are indicated in bold.

Forecast Period	**Hybrid**	**ARIMA**	**LES**	**SES**	**RW**
2013 Jan	**0.863**	0.841	0.834	0.849	0.827
2013 Feb	**0.865**	0.836	0.838	0.847	0.820
2013 Mar	**0.858**	0.827	0.825	0.818	0.807
2013 Apr	**0.850**	0.821	0.803	0.817	0.796
2013 May	**0.867**	0.819	0.828	0.830	0.794
2013 Jun	**0.877**	0.825	0.825	0.815	0.800
2013 Jul	**0.851**	0.817	0.814	0.801	0.785
2013 Aug	**0.864**	0.816	0.811	0.809	0.803
2013 Sep	**0.861**	0.826	0.810	0.818	0.811
2013 Oct	**0.876**	0.829	0.816	0.820	0.813

Table 5.3: nMBE (%) comparison among 5 forecasting methods for Colorado data. The lowest absolute values are indicated in bold.

Forecast Period	**Hybrid**	**ARIMA**	**LES**	**SES**	**RW**
2013 Jan	-1.41	-1.25	-1.68	-1.22	**0.31**
2013 Feb	-1.52	-3.11	-2.94	-1.61	**-0.16**
2013 Mar	-1.01	-0.98	-0.54	-1.33	**-0.25**
2013 Apr	1.20	-2.17	-1.32	-1.95	**0.53**
2013 May	0.52	-1.63	-1.69	**-0.26**	0.64
2013 Jun	**0.12**	-1.22	-3.21	-1.93	0.49
2013 Jul	-0.63	**-0.58**	-0.85	-1.54	-0.74
2013 Aug	0.60	-1.49	-0.39	**-0.25**	0.36
2013 Sep	-0.96	-1.33	**-0.75**	-0.76	-0.86
2013 Oct	-1.24	-2.98	-1.64	-0.66	**-0.09**

Table 5.4: nRMSE (%) comparison among 5 forecasting methods for SERIS data. The lowest values are indicated in bold.

Forecast Period	**Hybrid**	**ARIMA**	**LES**	**SES**	**RW**
2013 Jan	**45.28**	47.65	48.12	47.64	54.22
2013 Feb	**29.33**	31.47	34.93	33.10	36.03
2013 Mar	37.99	39.55	38.91	**37.80**	41.06
2013 Apr	**37.06**	38.00	39.41	39.45	42.02
2013 May	**35.92**	39.26	40.17	37.62	43.61
2013 Jun	41.14	42.32	41.08	**39.46**	45.93
2013 Jul	**29.16**	33.24	33.17	32.95	39.74
2013 Aug	**33.82**	35.51	34.44	35.73	39.70
2013 Sep	**35.10**	39.11	37.02	37.85	43.12
2013 Oct	38.97	**38.76**	38.92	40.27	44.19

Table 5.5: R^2 comparison among 5 forecasting methods for SERIS data. The highest values are indicated in bold.

Forecast Period	**Hybrid**	**ARIMA**	**LES**	**SES**	**RW**
2013 Jan	**0.606**	0.542	0.510	0.544	0.376
2013 Feb	**0.807**	0.799	0.778	0.783	0.761
2013 Mar	0.749	0.738	0.744	**0.752**	0.733
2013 Apr	**0.772**	0.767	0.742	0.739	0.659
2013 May	**0.764**	0.743	0.732	0.768	0.624
2013 Jun	0.735	0.712	0.738	**0.746**	0.575
2013 Jul	**0.811**	0.768	0.772	0.789	0.744
2013 Aug	**0.797**	0.763	0.770	0.761	0.749
2013 Sep	**0.780**	0.739	0.752	0.750	0.623
2013 Oct	0.741	**0.752**	0.743	0.727	0.601

Table 5.6: nMBE (%) comparison among 5 forecasting methods for SERIS data. The lowest absolute values are indicated in bold.

Forecast Period	**Hybrid**	**ARIMA**	**LES**	**SES**	**RW**
2013 Jan	-0.96	-1.76	-1.38	-1.33	**-0.33**
2013 Feb	-1.21	-1.34	-1.55	-1.27	**-0.25**
2013 Mar	-0.86	-2.61	**-0.12**	-0.60	-0.36
2013 Apr	**-0.38**	-2.94	-0.73	-0.79	-0.76
2013 May	-1.21	-1.39	-2.17	-0.65	**0.05**
2013 Jun	1.84	-1.11	-1.32	-2.95	**-0.11**
2013 Jul	1.22	-3.67	-2.14	**-0.11**	0.26
2013 Aug	**-0.29**	-1.03	-1.20	-1.00	-0.59
2013 Sep	**0.42**	-1.24	-1.98	-0.91	0.96
2013 Oct	0.61	-1.99	**-0.14**	-0.34	0.22

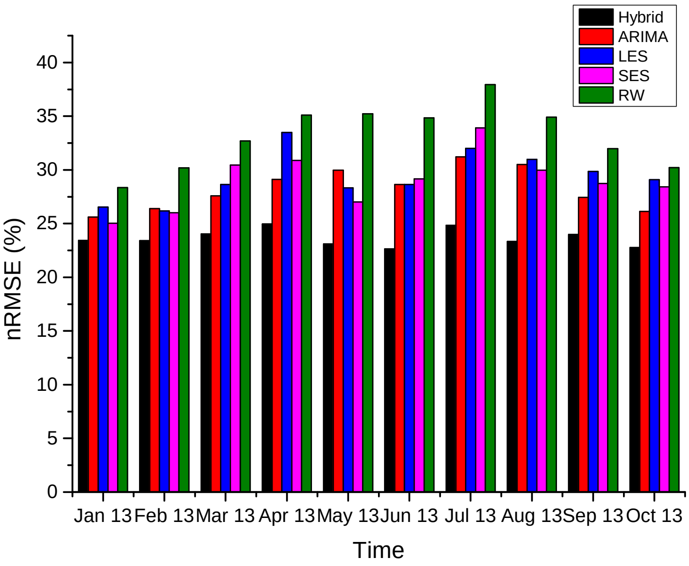

Figure 5.4: nRMSE (%) comparison among 5 forecasting methods for Colorado data

els in Colorado, USA. The best forecasting accuracy is shown in bold. It is clear that the hybrid model has better prediction accuracy than the other time series models based on nRMSE. From January 2013 to October 2013, the hybrid model consistently outperforms all other comparison models. On average the forecasting accuracy of the proposed model has 4% lower error compared with the best prediction accuracy of all other statistical time series models. It is noted that the solar irradiance variability in this area is generally low. The climate in Colorado is cool and dry which is the result of the combination of high elevation, mid latitude interior continent geography. The thin atmosphere with little clouds allows greater penetration of solar irradiance during all the seasons. However the thunderstorms often occur in the summer, which increases the solar irradiance variability. This matches our simulation result.

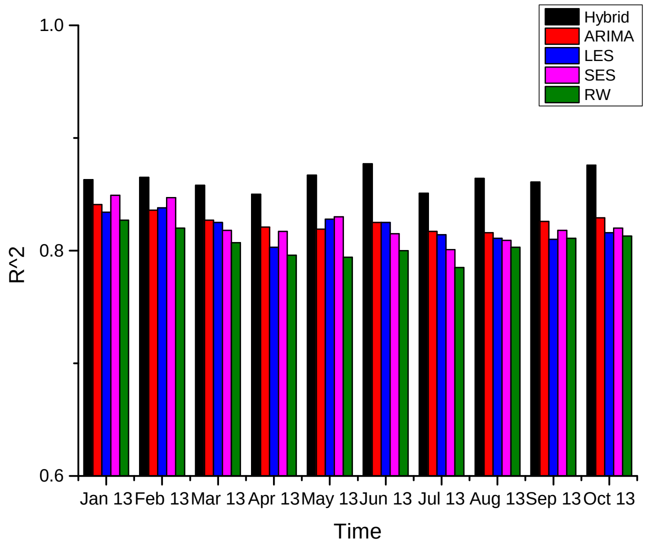

Figure 5.5: R^2 comparison among 5 forecasting methods for Colorado data

Table 5.2 and Figure 5.5 show the R^2 comparison of the hourly solar irradiance forecasting accuracy of all the models. By comparing Table 5.1 and Table 5.2 we can observe that the value of the coefficient of determination matches the result of normalized root mean squared error, which substantiate our analysis.

Table 5.3 and Figure 5.6 show the normalized mean bias error comparison of the hourly solar irradiance forecasting accuracy of all the models. The bias errors for all the models are generally less than 2% with a few exceptions. These small bias errors indicate that there is no particular bias in our forecasting models. It is expected that the benchmark RW model has the smallest bias error for most of the times since it is based on persistence.

Table 5.4 and Figure 5.7 show the normalized root mean square error comparison of the hourly solar irradiance forecasting accuracy of all the models in Singapore. The best forecasting accuracy is shown in bold. In general,

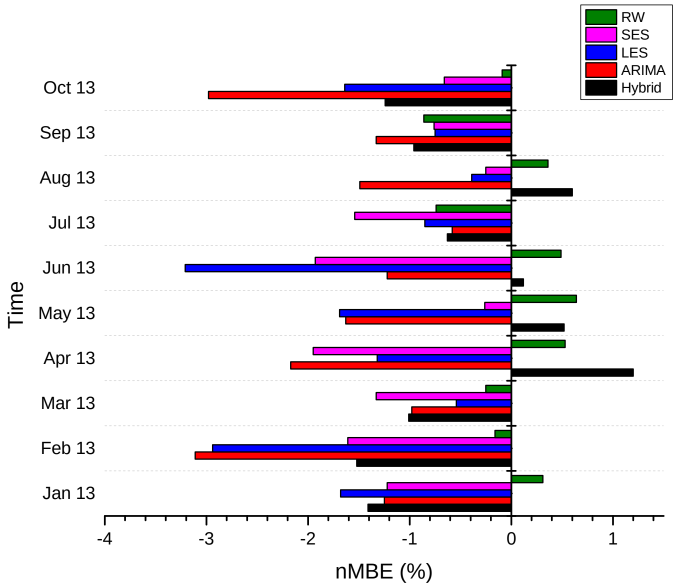

Figure 5.6: nMBE (%) comparison among 5 forecasting methods for Colorado data

the hybrid model has better prediction accuracy than the other time series models based on nRMSE. From January 2013 to October 2013, the hybrid model outperforms all other comparison models in seven out of ten months. Compared with the test in Colorado, the accuracy improvement is not very significant. There are two reasons behind this. Firstly, the solar irradiance variability in Singapore is much higher than the variability in Colorado due to the difference in climate conditions. Singapore has no clear-cut wet or dry season and rainfall is experienced in every month. Usually the rainfall occurs during the day but usually only for a short period of time. The high temperature and high humidity levels lead to high evaporation which causes frequent cloud formation and dense cloud cover. Therefore the solar irradiance variability is high in Singapore. Secondly, the training data in Singapore is only available from 2010, which is much less than the 17-year training data in Col-

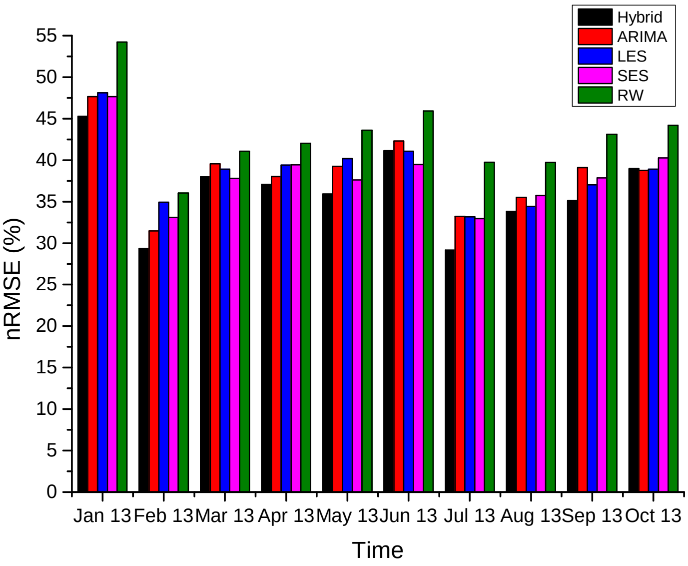

Figure 5.7: nRMSE (%) comparison among 5 forecasting methods for SERIS data

orado. The length of the training data is a crucial factor in our neural network based model. The performance of the model can be affected at different scales depends on the characteristics of the training data.

Table 5.5 and Figure 5.8 show the R^2 comparison of the hourly solar irradiance forecasting accuracy of all the models. By comparing Table 5.4 and Table 5.5 we can observe that the value of the coefficient of determination matches the result of normalized root mean squared error, which substantiate our analysis. Table 5.6 and Figure 5.9 show the normalized mean bias error comparison of the hourly solar irradiance forecasting accuracy of all the models. The bias errors for all the models are generally less than 3% with a few exceptions. These small bias errors indicate that there is no particular bias in our forecasting models.

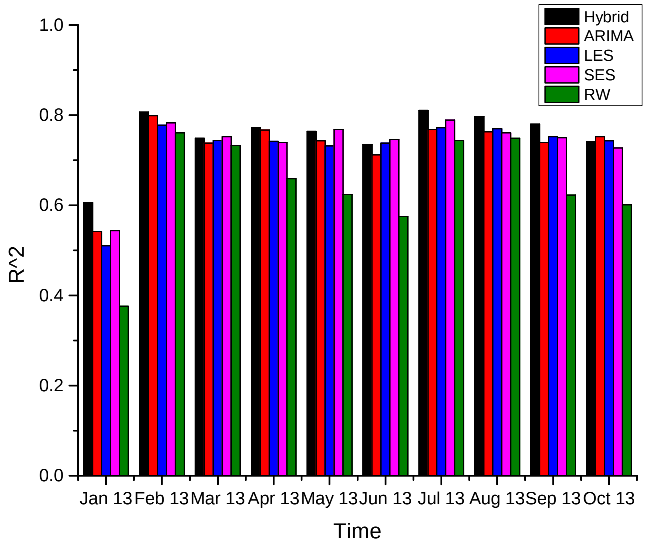

Figure 5.8: R^2 comparison among 5 forecasting methods for SERIS data

5.3.3 Computational complexity

Same as chapter 4, the hybrid model here is also implemented based on Theano library in Python. Theano is designed to define, optimize, and evaluate mathematical expressions involving multi-dimensional arrays efficiently. The parallel computational structure of Theano allows us to have fast training time even with a quad-core 3.5GHz personal computer. For one year hourly training data, the hybrid model training can be finished within 10 minutes.

5.4 Performance comparison of the medium-term forecasting models

The performances of the mid-term forecasting models are compared using hourly solar irradiance data in Singapore for the whole year of 2015. The

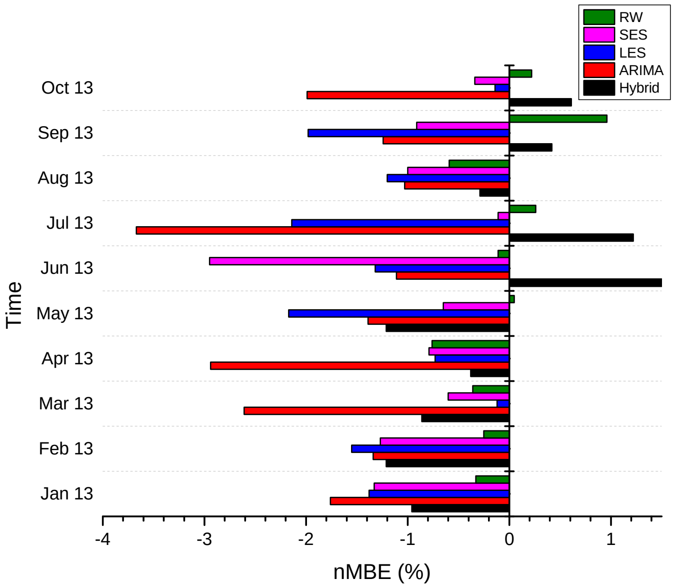

Figure 5.9: nMBE (%) comparison among 5 forecasting methods for SERIS data

nRMSE comparison is shown in Figure 5.10. The nMBE comparison is shown in Figure 5.11. Among all the models available for mid-term forecasting, the hybrid SOM-SVR-PSO model (HSVR in the figure) has the lowest error in most of the months. The hybrid SOM-SVR-PSO model is also not consistently biased to either positive or negative values.

Unfortunately, the satellite images are not available for the year of 2015. Hence we are comparing our hybrid satellite-ESSS-MLP model (HMLP in the figure) with the other 6 mid-term forecasting models using the satellite images and solar irradiance data from October 2010 to July 2011. The nRMSE comparison is shown in Figure 5.12. The nMBE comparison is shown in Figure 5.13. It is apparent that the hybrid satellite-ESSS-MLP model outperforms other models, except in the month of July 2011 which suffers from missing satellite images. Among all the models, the hybrid satellite-ESSS-MLP model

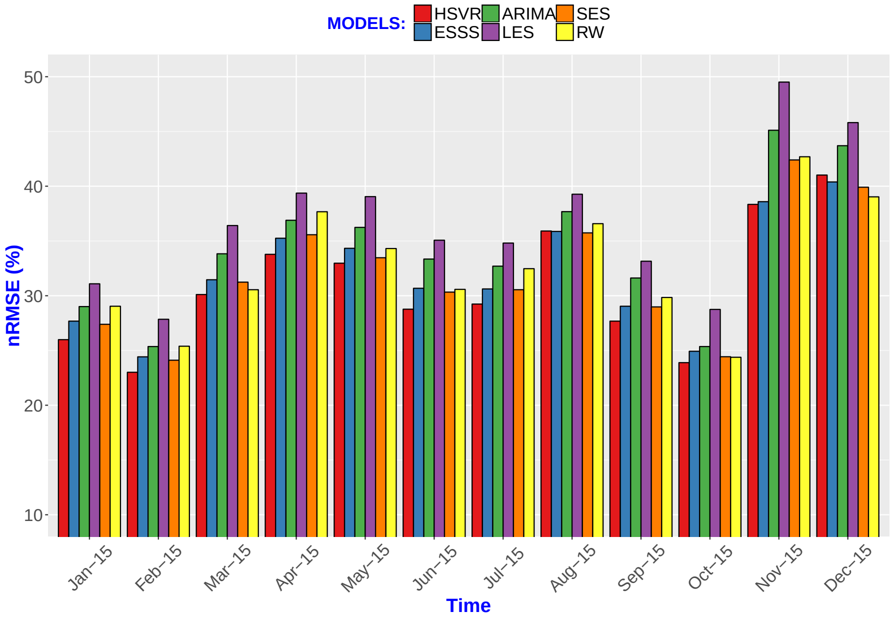

Figure 5.10: nRMSE (%) comparison of 6 forecasting methods for hourly Singapore data in 2015

is the only one with additional cloud information input derived from satellite images. The superior forecasting accuracy also demonstrates the importance of cloud condition information in solar irradiance forecasting.

The proposed novel models should also be compared with other researchers' models on some benchmark data available to the public. Measurement and Instrumentation Data Center (MIDC) of NREL has done a great job maintaining many solar irradiance monitoring stations in various states of the United States of America. Their data are available to the public and served as benchmarks for many solar irradiance forecasting researchers (Boland, David, and Lauret, 2016). Two locations are used for results comparison, namely Las Vegas, Nevada and Oahu, Hawaii. Las Vegas locates at 115.14 West Longitude, 36.17 Latitude, which has a typical sub-tropical inland climate. Oahu

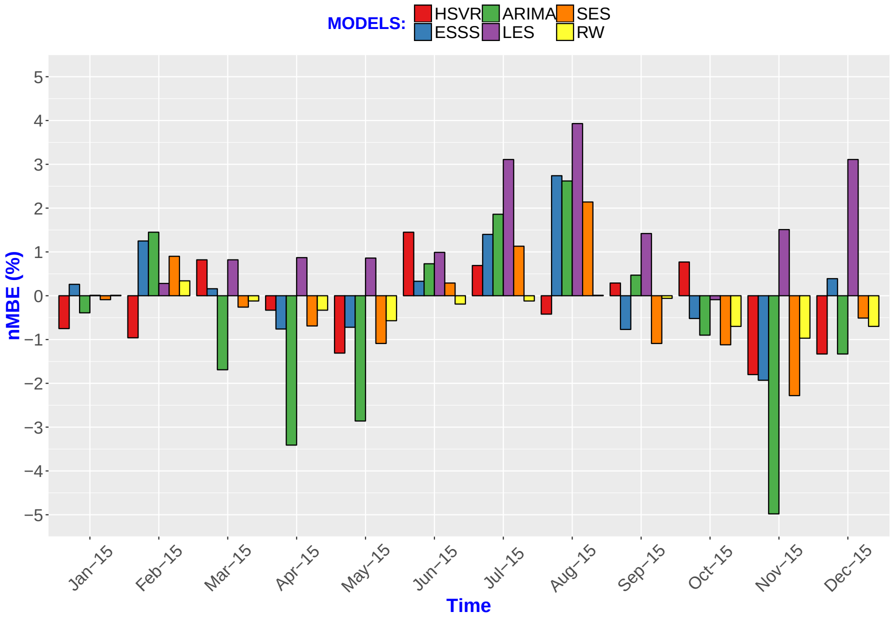

Figure 5.11: nMBE (%) comparison of 6 forecasting methods for hourly Singapore data in 2015

locates at 158.08 West Longitude, 21.31 Latitude, which has a typical subtropical island climate. One year of data in 2014 is used for training and the data in 2015 is used for testing.

Persistence is used as a benchmark model to be compared with the proposed hybrid SVM model without satellite image input and the ESSS model with Fourier trend preprocessing. Two other forecasting models proposed recently by Prof Boland are also compared (Boland, David, and Lauret, 2016). One is the artificial neural network (ANN) model and the other one is the ARMA model with Fourier trend preprocessing. The yearly average nRMSE comparison is shown in Figure 5.14. As can be seen, the proposed hybrid SVM without satellite image input outperforms all other models.

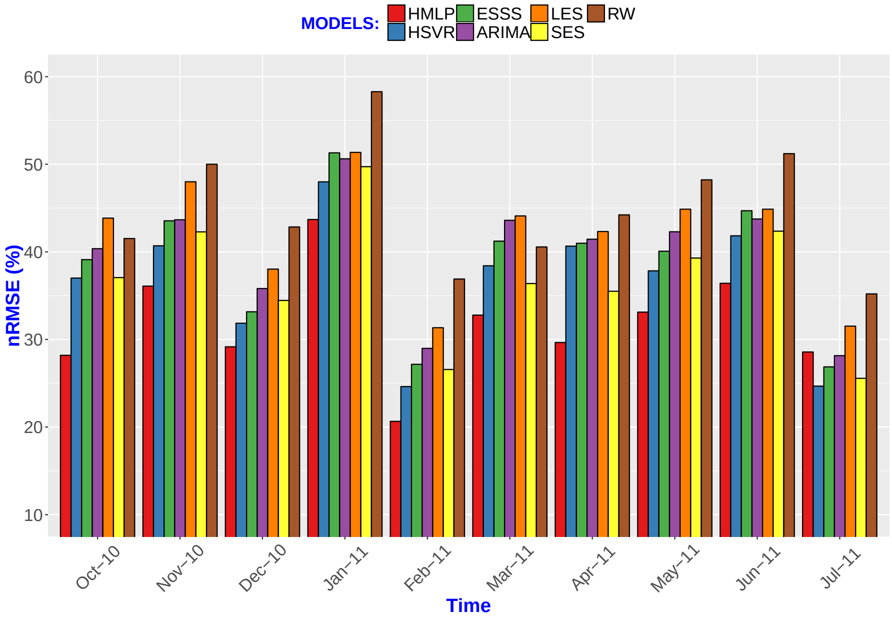

Figure 5.12: nRMSE (%) comparison of 7 forecasting methods for hourly Singapore data from Oct 2010 to Jul 2011

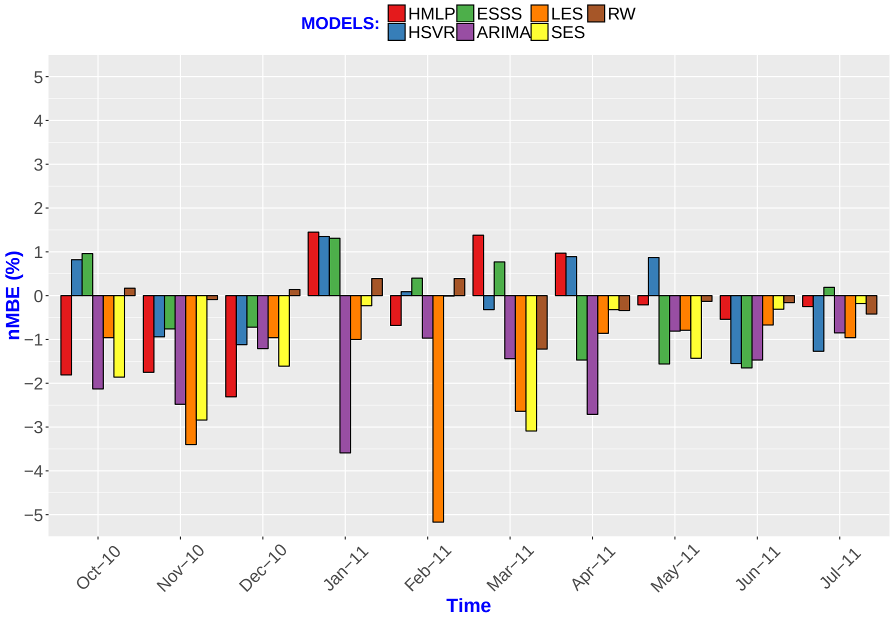

Figure 5.13: nMBE (%) comparison of 7 forecasting methods for hourly Singapore data from Oct 2010 to Jul 2011

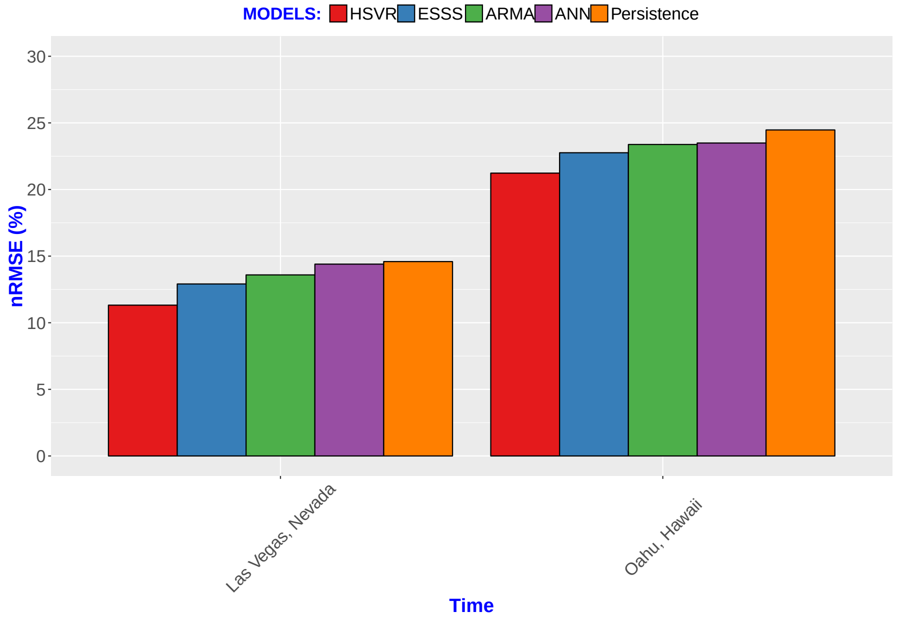

Figure 5.14: nRMSE (%) comparison of 5 forecasting methods for hourly solar irradiance data in Las Vegas and Oahu

Chapter 6

Solar irradiance forecasting using novel spatial-temporal analysis

6.1 Spatial-temporal covariance structures and time-forward kriging

Single station solar irradiance forecasts using statistical methods have been studied intensively in the past few decades. These include time series, autoregressive integrated moving average (ARIMA) analyses (Moreno-Muñoz et al., 2008; Reikard, 2009a; Martín et al., 2010), artificial neural networks (ANN) multi-layer perceptron model (Paoli et al., 2010; Mellit et al., 2010; Martín et al., 2010), k-Nearest Neighbors' algorithm (Paoli et al., 2010) and Bayesian inference (Paoli et al., 2010). Although the accuracies of these forecasting methods can be adequate, they do not provide spatial irradiance information. Thus in order to plan the electricity generation at power grid level, we require a large number of monitoring stations over the power grid area. The number of sensors is generally limited and their distribution is irregular. Thus, spatial-temporal estimation for solar irradiance is an important step towards the forecast required by renewable energy driven cities.

Temporal and spatial behaviours of solar irradiance are related through complex atmospheric mechanisms. Recent advances in space-time statistics (Cressie and Wikle, 2011; Le and Zidek, 2006; Finkenstädt, Held, and Isham, 2006) allow us to analyse such environmental processes not only in separate temporal and spatial domains but as a whole. Little work has been done on solar irradiance, although (Gueymard and Wilcox, 2011) provides a study on long term (inter-annual) variability in global radiation. Most studies employ separate modelling despite aiming to study solar irradiance across time as well as space (Glasbey, Graham, and Hunter, 2001). We aim to develop statistics that directly describe the spatial-temporal process. To facilitate our following discussion, we first introduce several statistics.

6.1.1 Some definitions

In statistics, covariance is a measure of the extent to which two random variables vary together. Very often, the covariance between two random variables can be modelled using a covariance function of space and time, the applications of which are widely seen in statistical planning and inference (Du and Ma, 2013; Hyun, Burman, and Paul, 2012).

A random field at location $\mathbf{s}_i$ and time t_i is denoted as $Z(\mathbf{s}_i, t_i)$, $Z \in \mathbf{R^d} \times \mathbf{R}$. We say the random field Z has separability if the covariance structure of Z can be separated into a purely spatial covariance structure and a purely temporal covariance structure:

$$\mathrm{cov}\{Z(\mathbf{s}_i, t_i), Z(\mathbf{s}_j, t_j)\} = \mathrm{cov}_{\mathrm{S}}\{Z(\mathbf{s}_i), Z(\mathbf{s}_j)\} \cdot \mathrm{cov}_{\mathrm{T}}\{Z(t_i), Z(t_j)\} \tag{6.1}$$

where the subscripts S and T are used to denote space and time respectively. However, most of the environmental data set can not be assumed to be separable due to the complex time and space interactions. A more general class of spatial temporal processes are the fully symmetric processes. A random field is said to be fully symmetric if:

$$\text{cov}\{Z(\mathbf{s}_i, t_i), Z(\mathbf{s}_j, t_j)\} = \text{cov}\{Z(\mathbf{s}_i, t_j), Z(\mathbf{s}_j, t_i)\} \tag{6.2}$$

Examples of the above covariance functions appear in our case studies, below. Separability is a special case of full symmetry. Therefore when the covariance matrix is not fully symmetric, it can not be separable.

Another important property of spatial-temporal data is stationarity. We say a random field exhibits temporal stationary if the covariance function $\mathbb{C}$ is only a function of time separation τ, where $\tau = t_i - t_j$. A similar definition can be applied to spatial stationarity. A random field exhibits temporal stationary if the covariance function is only a function of spatial separation $\mathbf{h}$, where $\mathbf{h} = \mathbf{s}_i - \mathbf{s}_j$. We will show later that $\mathbf{h}$ does not necessarily represent the geographical distance between two observations. In mathematical form, spatial temporal stationarity is:

$$\text{cov}\{Z(\mathbf{s}_i, t_i), Z(\mathbf{s}_j, t_j)\} = \mathbb{C}(\mathbf{h}, \tau) \tag{6.3}$$

Stationarity does not imply full symmetry nor separability. A special case of a separable stationary random field is represented by:

$$\text{cov}\{Z(\mathbf{s}_i, t_i), Z(\mathbf{s}_j, t_j)\} = \mathbb{C}_S(\mathbf{h}) \cdot \mathbb{C}_T(\tau) \tag{6.4}$$

Similarly, fullsymmetry can be defined as $\mathbb{C}(\mathbf{h}, \tau) = \mathbb{C}(\mathbf{h}, -\tau)$.

6.1.1.1 Anisotropy and time-forward kriging

The definitions introduced above indicate that using statistical prediction methods requires careful analytical description and analysis of a dataset. Properties such as stationarity, separability and isotropy are frequently overlooked.

For example, in geostatistics, 2D linear least squares estimation is often performed using kriging algorithms to construct 2D contour images, such as irradiance maps. Rehman et al. (Rehman and Ghori, 2000) plot monthly irradiance contours for Saudi Arabia; Righini et al. (Righini, Gallegos, and Raichijk, 2005) develop contours for Argentina; Bland et al. (Bland and Clayton, 1994) for Wisconsin and Bechini et al. (Bechini et al., 2000) for northern Italy. These authors first identify a suitable variogram model (variance versus distance plot) for the region and then apply weighted spatial smoothing kriging techniques to perform the spatial prediction.

Spatial resolution, an important consideration in all spatial-temporal irradiance studies, is often limited by data sparsity. In the context of solar irradiance, it has been shown that the spatial correlation between two locations converges after the threshold distance (Perez et al., 2012). The dependence metrics used in kriging, such as dispersion or correlation, must be carefully selected. Previous studies have applied kriging techniques to data from stations with large geographical separations. As a result, overestimates of the threshold distance occur, leading to information loss. Furthermore, many authors ignore the anisotropic nature of atmosphere processes by fitting isotropic variogram models. The large fitting errors typical in the literatures imply uncertainties in their following analyses that render them too inaccurate for practical applications. It is likely that no isotropic variogram model can represent the anisotropic nature of the spatial variability of solar irradiance (Sampson and Guttorp, 1992). We show that even within a small island like Singapore (41.8 km ENE-WSW and 22.5 km SSE-NNW), whatever happens in the east is unlikely to cause any variability change in the west. We therefore aim to take anisotropy into consideration in this work.

6.1.2 Temporal stationarity

We consider a time series (a sequence of observations taken sequentially in time) to be stationary if it has a constant mean level (Box, Jenkins, and Reinsel, 1970). Both stationary and non-stationary time series forecasting models have been developed, including auto-regressive (AR), moving average (MA), auto-regressive moving average (ARMA), integrated moving average (IMA), ARIMA and seasonal auto-regressive integrated moving average (SARIMA) (Box, Jenkins, and Reinsel, 1970). Among these models, AR, MA and ARMA are commonly used to forecast stationary trends. A test for stationarity is thus the first step to all time series analyses.

Wu et al.(Wu and Chan, 2011) performed the stationarity test for a typical Singapore irradiance time series using the Augmented Dickey-Fuller test (Dickey and Fuller, 1981). The time series was found to be non-stationary. Our aim at this stage is to obtain a stationary time series at each individual station without assuming spatial-temporal separability. Thus detrend methods similar to those adopted in time series analyses are considered. We note that there are other methods to achieve stationarity. The differencing technique, used frequently in ARIMA forecasts, is the transformation of the series to a new time series where the new values are the differences between consecutive values. Although appropriate for stationary transformation method for single station forecasts, the coupling between space and time in our 2D data make this technique less than optimal. Using a purely temporal analysis may not preserve the data's spatial-temporal covariance structure.

Existing detrend models include those that fit the GHI series with a Gaussian function (Baig, Achter, and Mufti, 1991), with a cosine function (Kaplanis, 2006) and with high order polynomials (Al-Sadah, Ragab, and Arshad, 1990a). These formulations describe the trend components of the irradiance time series with bell-shaped curves. There are also more sophisticated detrend procedures, for example, Yang et al.(Yang, Jirutitijaroen, and Walsh, 2012b) used local polynomial regression fitting (*LOESS*) to detrend the solar irradiance time series by first determining an additive diurnal cycle. Such techniques can provide location-specific stationary time series by finding the least squared fitted parameters. Different irradiance monitoring stations do not necessarily share the same model parameters. For our analyses, spatial-temporal structures must be preserved, and therefore we cannot invoke such techniques.

Since Singapore is located near the equator, we only consider the diurnal trend here. The extraterrestrial irradiance model, which is the level of irradiance received just outside of the atmosphere, is commonly used in irradiance modelling, and we shall apply it here. We can consider the extraterrestrial irradiance as a deterministic parameter given by:

$$E_0 I_{sc} \cos(\angle z) \tag{6.5}$$

where E_0 is the eccentricity of the Earth's orbit, I_{sc} is the solar constant and $\angle z$ is the zenith angle. The *clearness index* is defined as the ratio between global horizontal irradiance and the extraterrestrial irradiance. We thus transform our irradiance time series into a *clearness index* time series.

Trend removal via the *clearness index* as we have applied it here to diurnal phenomena cannot remove the trend completely and therefore does not make the series perfectly stationary. Therefore we perform the Kwiatkowski-Phillips-Schmidt-Shin (KPSS) test (Kwiatkowski, Phillips, and Schmidt, 1992) to assess stationarity in our detrended series. The KPSS test has a null hypothesis, H_0, to imply stationarity, and an alternative hypothesis H_1 to imply a unit root, i.e., non-stationary. The hypothesis testing is based on searching for a unit root in the time series autocorrelation model. In other words, if the observation at time t strongly depends on the observation at time $t-1$ with coefficient larger than 1 ($y_t = \mu + \phi y_{t-1}$, $\phi > 1$), the series is defined to be non-stationary or explosive. The p-value is a measure of the evidence against H_0: the smaller the p-value, the stronger evidence against H_0. The monthly time series at individual stations has a p-value greater than 0.1, which indicates strong evidence in favour of the null hypothesis (Wasserman, 2003). We note that all hypothesis tests suffer from the problem of probability of false declaration. When the number of test points increases, the probability of falsely declaring significance is likely to increase. However, we disregard this issue in this work, since we only utilize several weeks' of 2012 November data in our stationary analyses.

6.1.3 Spatial stationarity

Covariance estimation of spatial processes is fundamental for many problems of spatial interpolation and design of monitoring networks (Sampson and Guttorp, 1992). However, most environmental spatial-temporal processes (Gneiting, 2002; Luna and Genton, 2005) cannot be assumed to be stationary or isotropic. Studies of geographical data can derive additional physical information by appropriate use of spatio-temporal statistics. For instance, the conventional variogram (a function describing the spatial dependence of a random field) is a convenient tool to examine the spatial dispersion versus the geographical distance in many studies. However it is known that no isotropic variogram model will accurately reflect irradiance data (Rehman and Ghori, 2000; Sampson and Guttorp, 1992). Anisotropy is also discovered in the famous Irish wind data (Haslett and Raftery, 1989). Therefore, a forecasting method that operates on spatial covariance structures that do not assume stationarity will perform better than methods that falsely make this assumption.

6.1.3.1 G plane and D plane

Sampson and Guttorp(Sampson and Guttorp, 1992) proposed a method to estimate spatial covariance structures using a nonparametric approach. The method constructs a mapping function between locations in geographic space, where stationarity of the random field is not assumed, to locations in a new space where isotropy is assumed. Sampson and Guttorp refer to geographic space as the G plane and the dispersion space (the new space) as D plane.

The distances among stations in the D plane originate from spatial dispersion which is defined as:

$$d_{ij}^2 = v\hat{a}r(Z_{it} - Z_{jt}) \tag{6.6}$$

where $Z_{it} = Z(x_i, y_i, t)$ denotes the observation taken at location (x_i, y_i) at time t ($i = 1, 2, \cdots$, N and $t = 1, 2, \cdots, T$). Similar definitions can be used for Z_{jt} at another location j. $v\hat{a}r$ denotes the sample variance of the differenced time series. We can then determine a monotone function $\delta(d_{ij})$ to realize the D plane distance h_{ij} through multidimensional scaling (MDS), i.e.:

$$\delta(d_{ij}) \approx h_{ij} \tag{6.7}$$

δ is obtained through iterative monotonic regression.

6.1.3.2 Computation for the D plane representations

Multidimensional scaling provides a “principle components” representation of the pattern of proximities or dissimilarities (i.e., spatial dispersion) among a set of objects (in our case the *clearness index* measurements of the stations). There are two types of MDS, namely, classical MDS and nonmetric MDS. Classical MDS takes a matrix of dissimilarities (usually the Euclidean distance among the higher dimensional objects) as input, and outputs an object map in lower dimensions (usually a two dimensional Cartesian coordinate system). A good way to visualize the classical MDS is to imagine a projection of a three or higher dimensional structure onto a plane. As the dissimilarities matrix is always positive definite[1], the coordinates are given by the square root matrix of the transformed (double centering transformation) dissimilarities matrix. The method to solve for the coordinates of projection is eigendecomposition.

The nonmetric MDS methods on the other hand do not consider the dissimilarities but only their rankings. The input for nonmetric MDS is the dissimilarity ranking and the output is the stations map. In our application, this procedure finds a set of two dimensional vectors (locations of stations) in the D plane such that the matrix of proximities among them corresponds as closely as possible to a function of the input matrix (derived using classical MDS) according to the stress criterion function:

$$S = \min \sum_{i,j} \frac{[h_{ij} - \delta(d_{ij})]^2}{h_{ij}^2} \tag{6.8}$$

where h_{ij} is the Euclidean distance in the D plane, δ is a least square monotone regression function of h_{ij} on d_{ij}. $\delta(d_{ij})$ is sometimes referred to as disparities. The purpose of the stress function is to ensure that the stress is invariant under not only rigid motion (e.g. rotation, translation and reflection) but also uniform stretching[2]. At this stage, in the D plane, since the spatial dispersions are functions only of h_{ij}, we may view the D plane as a transformation of the G plane defined so that the spatial dispersion structure is both stationary and isotropic.

The stress function is minimized by method of steepest descent. For

---

[1] In linear algebra, a symmetric $n \times n$ real matrix $\mathbf{M}$ is said to be positive definite if $\mathbf{z^T M z}$ is positive, for any non-zero column vectors $\mathbf{z}$. The dissimilarity matrix is non-zero and symmetric, thus the eigenvalues are all positive.

[2] Without the denominator term in Equation (6.8), the stress is only invariant to rigid motions.

two dimensional data:

$$\mathbf{x}_{M+1} = \mathbf{x}_M - \frac{\frac{\partial S}{\partial \mathbf{x}} \times sl}{\left|\frac{\partial S}{\partial \mathbf{x}}\right|} \tag{6.9}$$

where $\mathbf{x} = (x_1, y_1, x_2, y_2, \cdots, x_N, y_N)^T$, a vector with $2N$ elements. $\mathbf{x}_M$ is the vector of coordinates at Mth iteration. sl is an iteration step length which is determined by $g(S_M, S_{M-1}, S_{M-5})$, a function of present stress S_M, the previous stress S_{M-1} and the stress 5 steps ago, S_{M-5}. The iterative method follows the proposed techniques(Kruskal, 1964a; Kruskal, 1964b). We use the standard R statistics software (R Development Core Team, 2011) implementation of the algorithm in this work. The iteration starts with the results from classical MDS. The implementation of the software is based on (Cox and Cox, 1994). We refer to nonmetric MDS as MDS hereafter.

6.1.3.3 Algebra for thin-plate spline mapping for G and D planes

Once the stations' coordinates in the G plane and the D plane have been established, we need to perform a one-to-one mapping between these two planes. Let the station coordinates in the G plane be denoted by (x_i, y_i) and those in the D plane by (x'_i, y'_i); we seek a bivariate function $f : \mathbf{R^2} \to \mathbf{R^2}$ that maps the coordinates from the G plane to the D plane:

$$\begin{pmatrix} x'_i \\ y'_i \end{pmatrix} = f \begin{pmatrix} x_i \\ y_i \end{pmatrix} \tag{6.10}$$

The algorithm determines a function by minimizing a certain roughness/smoothness criterion. For example, in one dimensional cubic spline interpolation, we minimize:

$$\int [f''(x)]^2 dx \tag{6.11}$$

subject to first and second order derivative constraints at the knots and at the boundaries. A cubic spline is a spline constructed of piecewise third-order polynomials which pass through a set of N control points (knots). The minimization constraint first considers the continuity at the knots by equating the gradients (first order derivatives) of two polynomials at each knot. The second order derivative is then minimized using the sum of the square of the derivative of the gradient (see Equation (6.11)) to ensure the fitted spline is the smoothest.

Bookstein (Bookstein, 1989) states the generalization of this measure for a two-dimensional problem:

$$J_f = \iint_{\boldsymbol{R^2}} \left[\left(\frac{\partial^2 f}{\partial x^2} \right)^2 + 2 \left(\frac{\partial^2 f}{\partial x \partial y} \right)^2 + \left(\frac{\partial^2 f}{\partial y^2} \right)^2 \right] dxdy \tag{6.12}$$

J_f is the measure of roughness/smoothness which is proportional to the bending energy of an idealized thin plate of infinite extent (Sampson and Guttorp, 1992). We show the method to determine the function f in this section.

Consider the function:

$$z(x,y) = U(r) = r^2 log(r^2) \tag{6.13}$$

where r is the distance $\sqrt{x^2+y^2}$ from the Cartesian origin. Let $P_1 = (x_1, y_1)$, $P_2 = (x_2, y_2)$, $\cdots$, $P_N = (x_N, y_N)$ be N points in G plane, we can define matrix

$$\mathbf{K} = \begin{pmatrix} 0 & U(r_{12}) & \cdots & U(r_{1N}) \\ U(r_{21}) & 0 & \cdots & U(r_{2N}) \\ \vdots & \vdots & \ddots & \vdots \\ U(r_{N1}) & U(r_{N2}) & \cdots & 0 \end{pmatrix}, \quad \in \mathbf{R^{N \times N}} \tag{6.14a}$$

$$\mathbf{P} = \begin{pmatrix} 1 & x_1 & y_1 \\ 1 & x_2 & y_2 \\ \vdots & \vdots & \vdots \\ 1 & x_N & y_N \end{pmatrix}, \quad \in \mathbf{R^{N \times 3}} \tag{6.14b}$$

$$\mathbf{L} = \left(\begin{array}{c|c} \mathbf{K} & \mathbf{P} \\ \hline \mathbf{P^T} & \mathbf{O} \end{array} \right), \quad \in \mathbf{R^{(N+3) \times (N+3)}} \tag{6.14c}$$

where $r_{ij} = |P_i - P_j|$ (Euclidean norm between the two points) and $\mathbf{O}$ is a 3×3 matrix of zeros. We can also define the matrix:

$$\mathbf{V} = \begin{pmatrix} x'_1 & x'_2 & \cdots & x'_N \\ y'_1 & y'_2 & \cdots & y'_N \end{pmatrix}, \quad \in \mathbf{R^{2\times N}} \tag{6.15a}$$

$$\mathbf{Y} = \begin{pmatrix} x'_1 & y'_1 \\ x'_2 & y'_2 \\ \vdots & \vdots \\ x'_N & y'_N \\ 0 & 0 \\ 0 & 0 \\ 0 & 0 \end{pmatrix}, \quad \in \mathbf{R^{(N+3)\times 2}} \tag{6.15b}$$

where each (x'_i, y'_i) is a station location in D plane. The elements of $\mathbf{L^{-1}Y}$ define the thin-plate spline $f(x, y)$ at an arbitrary point (x, y) (Bookstein, 1989), :

$$f(x, y) = a_1 + a_x x + a_y y + \sum_{i=1}^{N} w_i U(|P_i - (x, y)|) \tag{6.16}$$

$\mathbf{L^{-1}}$ is the pseudo inverse of $\mathbf{L}$, which is found through singular value decomposition.

Matrix $\mathbf{V}$ has two rows in our application. As such, two thin-plate splines, $f_x(x, y)$ and $f_y(x, y)$, are computed, one for $\{x'_i\}$ and one for $\{y'_i\}$. The function $f_x(x, y)$ maps arbitrary point (x, y) from the G plane to x-coordinate of the D plane, x'; while the function $f_y(x, y)$ maps arbitrary point (x, y) from G plane to the y-coordinate of the D plane, y'. A proof is shown by Kent et al.(Kent and Mardia, 1994) that Equation (6.16) minimizes roughness expression J_f in Equation (6.12).

This method maps an anisotropic random field to an isotropic random field. Together with the temporal stationarity, we obtain a spatial-temporal stationary data set. The following section describes the variance-covariance structures. We further explore the other two properties, namely, full symmetry and separability in the next sections.

6.1.4 Covariance and Kriging

After trend removal and space deformation, stationary spatial-temporal data can be obtained. We now introduce some stationary spatial-temporal variance-covariance structures (can be refer to as covariance structure for simplicity) which will be used later to forecast the *clearness index.*

6.1.4.1 Separable model

Recall that for our separable model, the covariance function describing the random field is assumed to be the product of the separated spatial and temporal covariance functions. Since fitting covariance or correlation will provide the same kriging results, here we follow the approach of Gneiting et al. (Gneiting, Genton, and Guttorp, 2007) and fit a purely temporal correlation function of the Cauchy type:

$$\rho_T(\tau) = (1 + a|\tau|^{2\alpha})^{-1} \tag{6.17}$$

where ρ stands for correlation and a, α are model parameters. For the spatial correlation function we choose an exponential model with a "nugget" effect (a term derived from from mining geostatistics):

$$\rho_S(\mathbf{h}) = (1 - \nu)\exp(-c \cdot \mathbf{h}) + \nu \mathbf{I}_{\mathbf{h}=0} \tag{6.18}$$

where ν and c are parameters to be fitted. $\mathbf{I}$ is a binary indicator function. Therefore the separable covariance function is given by:

$$\mathbb{C}_{SEP}(\mathbf{h}, \tau) = \rho_T(\tau) \cdot \rho_S(\mathbf{h}) \cdot \sqrt{\sigma_i^2}\sqrt{\sigma_j^2} \tag{6.19}$$

where $\sqrt{\sigma_i^2}$ and $\sqrt{\sigma_j^2}$ are the variance of location specified time series.

6.1.4.2 Fully symmetric model

We can construct the fully symmetric but generally non-separable correlation function using the separable model described earlier. Gneiting et al.(Gneiting, Genton, and Guttorp, 2006) state the theorem:

Theorem. *Suppose that $\varphi(r)$, $r \geq 0$, is a completely monotone function, and that $\psi(r)$, $r \geq 0$, is a positive function with a completely monotone derivative. Then*

$$\mathbb{C}(\mathbf{h}, \tau) = \frac{1}{\psi(|\tau|)^{d/2}} \varphi\left(\frac{\mathbf{h}^2}{\psi(|\tau|)}\right), \quad (\mathbf{h}, \tau) \in \mathbf{R^d} \times \mathbf{R} \tag{6.20}$$

is a stationary covariance function on $\mathbf{R^d} \times \mathbf{R}$.

As our specific choice of $\rho_T(\tau)$ and $\rho_S(\mathbf{h})$ satisfies the theorem, we can conclude that the covariance function in form shown in Equation (6.20) is stationary and fully symmetric. There are several choices in selecting $\psi(r)$, for example, $\psi_1(r) = (ar^{2\alpha} + 1)^{\beta}$, $\psi_2(r) = \ln(ar^{2\alpha} + b)/\ln(b)$ and $\psi_3(r) = (ar^{2\alpha} + b)/[b(ar^{2\alpha} + 1)]$. Consider our Cauchy type temporal correlation function, we select $\psi_1(r)$. Thus, we write parametric family:

$$\mathbb{C}_{FS}(\mathbf{h}, \tau) = \frac{1-\nu}{(1 + a|\tau|^{2\alpha})^{\beta}} \left[\exp\left(-\frac{c \cdot \mathbf{h}}{(1 + a|\tau|^{2\alpha})^{\beta/2}}\right) + \frac{\nu}{1-\nu}\mathbf{I}_{\mathbf{h}=0}\right] \cdot \sqrt{\sigma_i^2}\sqrt{\sigma_j^2} \tag{6.21}$$

Note that the parameter β has to satisfy constraint $0 \leq \beta \leq 1$ (Gneiting, 2002). β is called space-time interaction parameter. If $\beta = 0$ corresponds to a reduced separable model, we should replace the first β in Equation 6.21 by ζ and $\zeta = 1$.

6.1.4.3 Time-forward kriging

Spatial-temporal kriging technique has been applied in recent studies on high resolution spatial-temporal processes, and some studies (Inoue, Sasaki, and

Washio, 2012) have demonstrated its application to irradiance variability modelling. Inoue et al.(Inoue, Sasaki, and Washio, 2012) show that by considering time evolution, some improvements (on spatial irradiance prediction) over the traditional spatial kriging can be established using leave-one-out cross-validation on static maps.

Time-forward simple kriging is used in this study to assess the forecasting ability of the spatial-temporal structures. Kriging is used to estimate the weights of observed values $\mathbf{z}$ (from M temporal lags and N spatial points) using the known covariance structures. At each spatial location, the simple time-forward kriging point estimate $\hat{z}(\mathbf{s}, t)$ is thus given by:

$$\hat{z}(\mathbf{s}, t) = \mathbf{c_0'}\mathbf{C}^{-1}\mathbf{z} \tag{6.22}$$

where $\mathbf{C}$ is the spatial-temporal variance-covariance matrix, and $\mathbf{c_0'}\mathbf{C}^{-1}$ are the weights. $\mathbf{C}$ has dimension $\mathbf{R^{NM\times NM}}$, where N is the number of spatial locations and M is the maximum time lag under consideration:

$$\mathbf{C} = \begin{pmatrix} \mathbf{C}_0 & \mathbf{C}_1 & \cdots & \mathbf{C}_{M-1} \\ \mathbf{C}_1 & \mathbf{C}_0 & \cdots & \mathbf{C}_{M-2} \\ \vdots & \vdots & \ddots & \vdots \\ \mathbf{C}_{M-1} & \mathbf{C}_{M-2} & \cdots & \mathbf{C}_0 \end{pmatrix}, \quad \in \mathbf{R^{NM\times NM}} \tag{6.23}$$

$\mathbf{C}_{|\tau|}$ represents the spatial sub-covariance matrix at time lag $|\tau|$:

$$\mathbf{C}_{|\tau|} = \begin{pmatrix} C_{11,|\tau|} & C_{12,|\tau|} & \cdots & C_{1N,|\tau|} \\ C_{21,|\tau|} & C_{22,|\tau|} & \cdots & C_{2N,|\tau|} \\ \vdots & \vdots & \ddots & \vdots \\ C_{N1,|\tau|} & C_{N2,|\tau|} & \cdots & C_{NN,|\tau|} \end{pmatrix}, \quad \in \mathbf{R^{N\times N}} \tag{6.24}$$

where $C_{ij,|\tau|} = \text{cov}\{Z(\mathbf{s}_i, t), Z(\mathbf{s}_j, t - |\tau|)\}$. We will further illustrate the variance-covariance matrix construction in the following section. Similar to

$\mathbf{C}$, we write $\mathbf{c_0}$:

$$\mathbf{c_0} = \begin{pmatrix} \mathbf{c}_{\mathbf{0},1} & \mathbf{c}_{\mathbf{0},2} & \cdots & \mathbf{c}_{\mathbf{0},M} \end{pmatrix}', \quad \in \mathbf{R}^{\mathbf{NM}\times\mathbf{1}} \tag{6.25}$$

and

$$\mathbf{c}_{\mathbf{0},|\tau|} = \begin{pmatrix} c_{0,11,|\tau|} & c_{0,12,|\tau|} & \cdots & c_{0,1N,|\tau|} \end{pmatrix}', \quad \in \mathbf{R}^{\mathbf{N}\times\mathbf{1}} \tag{6.26}$$

with $c_{0,ij,|\tau|} = \text{cov}\{Z(\mathbf{s}_i, t), Z(\mathbf{s}_j, t - |\tau|)\}$. Lastly, $\mathbf{z}$ is the vector with the observed value from the past M steps from N locations. The arrangement of $\mathbf{z}$ must agree with the arrangement of $\mathbf{c_0}$.

Although we can use the Kronecker product to construct variance-covariance structures, this method is only applicable to separable variance-covariance structures, i.e., $\mathbf{C} = \mathbf{C_S} \otimes \mathbf{C_T}$, where $\mathbf{C_S}$ and $\mathbf{C_T}$ are separate spatial and temporal variance-covariance respectively. We note that the locations used to construct $\mathbf{c_0}$ need not to be the same as the locations used to construct $\mathbf{C}$ (since $\mathbf{c_0}$ only depends on inter-station distances and time lags). For these reasons, unlike conventional spatial-temporal forecasting methods, our method is able to forecast arbitrary points in space.

6.2 Transposition and decomposition models for conversion from tilted to horizontal surface

Accurate local solar irradiance data is required in many aspects of building design and solar thermal and photovoltaic (PV) systems planning. Increasingly, such information is also required with high precision for PV systems performance evaluation and for solar irradiance forecasting. In most solar power systems (thermal or PV), modules are installed on a fixed plane to reduce installation and operation costs compared to tracking systems. To maximize array output, the modules are installed at a tilt close to the local latitude, or at some minimum tilt to ensure self-cleaning by rain.

The output of PV systems above a certain size is generally monitored, and compared with irradiance as measured by an in-plane sensor in order to check the system's performance ratio. Thus many large PV systems measure in-plane irradiance continuously. For many purposes, such as spatial irradiance forecasting in grid integration, however, knowledge of the global horizontal irradiance (GHI) is needed, and its derivation from a tilted measurement is not trivial, owing to the non-isotropic nature of the diffuse component of irradiance. The ability to accurately convert solar irradiance components between horizontal and tilted planes then becomes a requirement for simulations, performance evaluation and forecasting of solar energy systems. Gueymard (Gueymard, 2009) has compared 10 transposition models and various direct/diffuse models for a mid-latitude site in Colorado, USA. Here we compare models against a very different dataset - that of an equatorial site located in Singapore, which exhibits very different, tropical atmospheric conditions. Design of PV systems for tropical conditions will be increasingly important in coming decades, as developing nations in the equatorial zone implement PV on large scales, in many cases also to reduce their dependency on fossil fuel imports.

Many transposition models have been proposed in the literature to convert solar irradiance on the horizontal plane to that on a tilted plane. The global irradiance, I_t, on a tilted plane of s degrees from the horizontal, can be evaluated from the standard equation:

$$I_\mathrm{t} = I_\mathrm{Dir}\cos\theta + I_\mathrm{Dif}R_\mathrm{d} + \rho I_\mathrm{Glo}R_\mathrm{r} \tag{6.27}$$

where I_Dir is the direct normal solar irradiance (DNI), I_Dif is the diffuse horizontal irradiance (DHI), I_Glo is the global horizontal irradiance (GHI), θ is the angle of incidence of the sun rays on the tilted plane, R_d is the diffuse transposition factor, ρ is the foreground's albedo, and R_r is the transposition factor for ground reflection.

It should be noted that the incidence angle θ of the sun's rays on a surface with an arbitrary tilt angle s and azimuth is purely geometric; its formulation can be found in standard texts (Duffie and Beckman, 2006). Ground reflection is considered as an isotropic process by most studies, and is characterized by R_r, which is a function of tilt angle s (Gueymard, 2009). The formulations for the diffuse transposition factor R_d can be divided into two schools, namely, isotropic[3] (Badescu, 2002; Tian et al., 2001; Koronakis, 1986; Liu and Jordan, 1962) and anisotropic (Perez et al., 1990; Reindl, Beckman, and Duffie, 1990b; Skartveit and Olseth, 1986; Temps and Coulson, 1977; Klucher, 1979; Hay, 1979). Details and mathematical formulations for R_d are summarized in the papers (Noorian, Moradi, and Kamali, 2008; Evseev and Kudish, 2009) for both types. The recent paper (David, Lauret, and Boland, 2013) evaluates the performance of various anisotropic transposition models in a tropical environment.

In order to compute the irradiance on a tilted surface, we need to know all three irradiance components on a horizontal surface, namely, GHI, DNI and DHI. The following equation describes a well-known relationship among the three components.

$$I_\mathrm{Glo} = I_\mathrm{Dir} \cos Z + I_\mathrm{Dif} \tag{6.28}$$

where Z is the zenith angle. This relationship implies that we should have at least two irradiance measurements in order to accurately predict the global solar irradiance on a tilted plane.

---

[3] Isotropic transposition usually refers to Liu and Jordan (1962) model. However, we consider the classification here helpful to distinguish the models that have no azimuthal dependence.

A pyranometer measures the total radiation arriving from all directions, including both direct and diffuse components through one or more thermopiles (Masters, 2004). By adding a shadow band to temporarily block the direct beam, the pyranometer can be used to measure just diffuse irradiance. Some pyranometer models, such as the SPN1 Sunshine Pyranometer from Delta Instruments[4], measure both global and diffuse irradiance simultaneously. Pyranometers are expensive and may require maintenance: more economic instruments such a simple photosensors which only measure GHI are very commonly deployed. When only I_{Glo} is obtained from such a photosensor, I_{Dir} and I_{Dif} must be individually estimated.

Multi-sensors approaches (Faiman, Feuermann, and Zemel, 1993) are often used to resolve this issue. When two irradiance sensors are installed at two different tilts, we can accurately solve for I_{Dir} and I_{Dif} using simultaneous equations (use Equation (6.27) twice by having two sets of parameters obtained from two tilts). Otherwise, decomposition models are used to estimate I_{Dir} and I_{Dif} from a single I_{Glo} measurement.

To separate the direct and diffuse components from I_{Glo}, many empirical relationships have been proposed. Instead of relating the irradiance components directly, most papers in the literature use the concept of transmittance or optical depth. Transmittance is a representation of fraction of extraterrestrial irradiance reaching the ground. Most approaches aim to represent diffuse horizontal transmittance K_{d} or direct normal transmittance K_{n} as a function of the effective global horizontal transmittance K_{t} (K_{t} is often referred to as the clearness index) and other predictors. Gueymard (Gueymard, 2009) suggests that the direct and diffuse separation be made dependent on zenith angle, ambient temperature and relative humidity. Some researchers (Garri-

---

[4] `http:\delta-t.co.uk`

son, 1985; Garrison and Sahami, 1995) suggest the separation should consider solar elevation, surface albedo, atmospheric precipitable water and snow cover. Reindl's various models (Reindl, Beckman, and Duffie, 1990a) include a multivariate version which suggests that solar altitude, ambient temperature, and relative humidity are the predictors for diffuse horizontal transmittance. These multivariate models are complex and the inputs measurements are not always available.

For the purposes of engineering in tropical locations, we seek simple empirical models to separate direct and diffuse components from global solar irradiance. Some papers (Erbs, Klein, and Duffie, 1982; Orgill and Hollands, 1977) used univariate approaches, namely, GHI as the only input. Maxwell (Maxwell, 1987) presented a bivariate model, which converts GHI into DNI using only GHI and zenith angle as inputs. Reindl also proposed versions of his model as both univariate and bivariate models (Reindl, Beckman, and Duffie, 1990a). Another paper (Zhang, 2006) used GHI and elevation angle (equals to $90° - Z$) as inputs, decomposition model is then constructed using the Gompertz function. Although these models are simpler, i.e., using only one or two input parameters, each correlation is developed from the measurements taken at some specific locations; therefore their accuracy must be carefully evaluated if they are applied to places different from the ones included in the databases used for their development (Padovan and Col, 2010).

As seen in Equation (6.27), GHI and DHI are required inputs for transposition models. When only GHI measurements are available, transposition models still can be used with the help of decomposition models. While these methods for converting solar irradiance from horizontal to tilted planes are well described, the reverse process, i.e. converting from tilted to horizontal, is lacking in the literature. PV array power output is often the parameter sought for practical applications, together with an estimate of the performance ratio of the PV system. Therefore, sensors are often installed in the plane of the PV array, rather than horizontally. Although this configuration is convenient for PV systems output prediction, many applications require horizontal irradiation data. For instance, in spatio-temporal forecasting analyses (Yang et al., 2013), data from various locations must be converted to horizontal irradiance in order to capture the spatio-temporal dynamics accurately. Such forecasts are of increasing importance, as variable renewable generation becomes a significant fraction of electricity generation capacity. Thus, an algorithm which converts solar irradiance on a tilted plane to horizontal irradiance is proposed in this chapter, with specific application to tropical regions being a consideration.

6.2.1 Model Selection for Tropical Regions

We first review available transposition and decomposition models and evaluate their performance of converting solar irradiance from horizontal to tilt in a tropical region. This exercise allows us to select the best model for the reverse process.

6.2.1.1 Background

We note two types of transmittance found in the literature, which link solar irradiance at the Earth's surface to extraterrestrial irradiance:

$$I_{\mathrm{Glo}} = K_{\mathrm{t}} I_{\mathrm{oh}} \tag{6.29}$$

$$I_{\mathrm{Dir}} = K_{\mathrm{n}} I_{\mathrm{o}} \tag{6.30}$$

K_{t} and K_{n} are effective global horizontal transmittance and direct normal transmittance respectively, while I_{oh} is horizontal extraterrestrial irradiance and I_o is extraterrestrial direct normal irradiance. The extraterrestrial irradiance is the function of zenith angle Z and day number D (i.e. January 1 is day 1 while December 31 is day 365 in a non-leap year, 366 in a leap year) as shown below:

$$\begin{aligned} I_\text{oh} &= (SC) \times r_\text{e} \cos Z & (6.31) \\ I_\text{o} &= (SC) \times r_\text{e} & (6.32) \end{aligned}$$

where,

$$\begin{aligned} r_\text{e} &= 1.00011 + 0.034221 \cos\xi + 0.001280 \sin\xi \\ &\quad +0.000719 \cos 2\xi + 0.000077 \sin 2\xi & (6.33) \\ \xi &= 2\pi(D-1)/365 & (6.34) \end{aligned}$$

r_e is the reciprocal of the square of the Earth radius factor as described by Maxwell (Maxwell, 1987) or the eccentricity correction factor of earth as defined in reference (Janjai, Sricharoen, and Pattarapanitchai, 2011). ξ is defined as the eccentric anomaly of the Earth in the orbit around the Sun (Maxwell, 1987) or day angle (Janjai, Sricharoen, and Pattarapanitchai, 2011). SC is the solar constant, equal to 1362 W/m^2.

We discuss the formulation for transposition factors for R_r and R_d in the following. As Singapore has a latitude of 1.3°N, the "rule-of-thumb" installation angle for fixed panels should be 1.3°. However, in practice, the installation angle in Singapore is usually chosen to be between 5° to 20° to maximize panels' output by promoting self cleaning by rain, without allowing surface-tension induced accumulation of dust at panels framed edges. A highly tilted plane introduces anisotropic features into derived R_r values (Gueymard, 2009), but this effect is not significant for slopes less than 20°. As a result, we use an isotropic approximation for R_r:

$$R_\text{r} = (1 - \cos s)/2 \tag{6.35}$$

where s is the tilt angle for the plane of incidence.

The diffuse transposition factor R_{d} may be considered isotropic if we assume that diffuse irradiance is constant over the whole sky. However, a plane of tilt s facing the (occulted) sun receives more diffuse radiation than a plane of the same tilt in the opposite direction. Both isotropic and anisotropic R_{d} models are discussed extensively in the literature. We shall compare ten models in the following section. We consider four isotropic models (Badescu, 2002; Tian et al., 2001; Koronakis, 1986; Liu and Jordan, 1962) and six anisotropic models (Perez et al., 1990; Reindl, Beckman, and Duffie, 1990b; Skartveit and Olseth, 1986; Temps and Coulson, 1977; Klucher, 1979; Hay, 1979). These ten models are provided in Appendix A.

By combining Equation (6.28) to (6.35), we rewrite Equation (6.27) using the "K" indices:

$$I_{\mathrm{t}} = K_{\mathrm{n}} I_{\mathrm{o}} \cos\theta + (K_{\mathrm{t}} - K_{\mathrm{n}}) I_{\mathrm{oh}} R_{\mathrm{d}} + \rho K_{\mathrm{t}} I_{\mathrm{oh}} [(1 - \cos s)/2] \qquad (6.36)$$

We call Equation (6.36) the target function. In order to find I_{t}, the global solar irradiance measurement on tilted plane, we need to know all the parameters on the right side of Equation (6.36). Among these parameters, θ is purely geometric and can be easily calculated. Although the foreground's albedo varies during the day for various reasons throughout the year, we assume that in tropical regions the variation is small when compared to winters at high latitude regions, owing to the total absence of snow and ice. We select a fixed value of 0.2 for ρ as suggested by Gueymard (Gueymard, 2009). As such, the only unknowns in target function are K_{t}, K_{n} and R_{d}.

We digress to reiterate the symbology used in above discussion. When we refer to solar irradiance striking a collector, usually we imply global solar irradiance (I_{t} in Equation (6.27)). Global solar irradiance can be represented by the sum of three separate components, namely, direct beam irradiance (represented by $I_{\mathrm{Dir}} \cos\theta$ term in Equation (6.27)), diffuse irradiance (represented by $I_{\mathrm{Dif}} R_{\mathrm{d}}$ term in Equation (6.27)) and reflected irradiance (represented by $\rho I_{\mathrm{Glo}} R_{\mathrm{r}}$ term in Equation (6.27)). When the collector is placed horizontally, the reflected irradiance becomes zero as R_{r} becomes zero (see Equation (6.35)), and the incidence angle θ is equal to zenith angle Z. Therefore, the direct beam irradiance is now expressed as $I_{\mathrm{Dir}} \cos Z$, and I_{Dir} is called DNI (direct normal irradiance). The anisotropic behaviour of diffuse irradiance originates from the scattering mechanism of the atmosphere. It is convenient to express the diffuse component received on a collector plane as a function of tilt and azimuth. We consider the diffuse irradiance on a horizontal plane as the reference; R_{d} in Equation (6.27) is unity under this condition. We name diffuse irradiance on a horizontal surface as DHI (diffuse horizontal irradiance). Finally, we refer to global solar irradiance on a horizontal surface as GHI (global horizontal irradiance). The relationship among GHI, DHI and DNI are expressed in Equation (6.28). Note that Equation (6.28) is a special case of Equation (6.27) when collector tilt is zero.

When all the irradiance components are known, i.e., measurements for at least two irradiance components are available, we can evaluate I_{t} directly through Equation (6.27). When only the global horizontal irradiance is known, we need decomposition models to predict direct and diffuse irradiance components. We select five models which are considered as "universal" models to formulate the relationship between K_{t} and K_{n}, namely, Erbs model (Erbs, Klein, and Duffie, 1982), Orgill model (Orgill and Hollands, 1977), Maxwell model (Maxwell, 1987), Reindl univariate model and Reindl bivariate model, both models are described by Reindl et al.(Reindl, Beckman, and Duffie, 1990a). These models are summarized in Appendix B. With the K_{t} and K_{n} relationships shown in B, together with transposition models, we can obtain I_{t} value using Equation (6.36).

6.2.1.2 Evaluation of Ten Transposition Models

We evaluate the performance of ten transposition models in this section. Knowledge of R_d is a prerequisite for use of Equation (6.27): we note that all transposition models are governed by Equation (6.27), the only difference among them being the different formulation for R_d (see Appendix A).

Figure 6.1: The first zero energy house in Singapore. Rooftop panels on the right and left have inclination of 18.3° and 6.1°; azimuth rotation (north is 0°) 66° NE and 246° SW respectively.

The irradiance data used here was obtained from the first zero energy house in Singapore, which is shown in Figure 6.1. The building aims to generate enough electricity for a six-person household using two PV arrays mounted on the metal roof (Singapore Energy Market Authority, 2011). The azimuths (north is 0°) of the PV arrays are 66° NE and 246° SW on the east and west roof respectively. The inclination angle of the east roof is 18.3° and 6.1° for the west roof.

As part of Solar Energy Research Institute of Singapore (SERIS)'s research efforts in the area of PV systems performance assessment and optimization in tropical regions, we have deployed two calibrated silicon sensors in the plane of array of each roof. The sensor facing east is named S111a and the flatter, back roof facing west is named S111b. The silicon sensors are temperature-corrected and have an accuracy of 5%. Calibration takes place every year at the Fraunhofer Institute for Solar Energy Systems (ISE) CalLab. The sampling rate of the setup is 1 Hz with logging rate at one minute. Beside these two silicon photosensor, a Delta-T SPN1 Sunshine Pyranometer is also installed horizontally on the roof, which we name S111. From the device's calibration data sheet, it has an accuracy of 5%. We log it only at five minutes interval. We average the one minute data to five minute in this section. We use the measurements from S111 as inputs to the transposition models. The model output is compared to the averaged measurements from S111a and S111b. We examine the performance of various transposition models using five-minute data from these three stations over a period of one year, namely, 2011.

We can see from Equations (6.28), (6.31) and (6.36) that the zenith angle Z and incidence angle θ for an arbitrary tilted plane are required to calculate I_{t}. We use the Solar Position Algorithm (SPA) (NREL, 2008) from National Renewable Energy Laboratory (NREL) to calculate the zenith angle and the incidence angle. The details of this algorithm can be found in the open source C program at (NREL, 2008).

We use mean bias error (MBE), relative root mean square error normalized by the mean of the measured values ($\mathrm{RMSE}_{\mathrm{rel,\ no\ bias}}$) and expanded uncertainty at 95% confidence interval (U_{95}) as our error metrics for the evaluation. We note that $\mathrm{RMSE}_{\text{rel, no bias}}$ is *not* the root mean square error; $\mathrm{RMSE}_{\text{rel, no bias}}$ is called the coefficient of variation of the root mean square error. The error calculations are shown below:

$$\mathrm{MBE} = \left[\sum_{i=1}^{N}(I_{\text{predicted,i}} - I_{\text{measured,i}})\right]/N \tag{6.37}$$

where N is number of samples.

$$\mathrm{RMSE}_{\text{rel, no bias}} = \frac{\sqrt{\frac{1}{N}\sum_{i=1}^{N}(I_{\text{predicted,i}} - \mathrm{MBE}_{\mathrm{i}} - I_{\text{measured,i}})^2}}{\frac{1}{N}\sum_{i=1}^{N} I_{\text{measured,i}}} \tag{6.38}$$

and

$$U_{95} = k \times \frac{\sqrt{\frac{1}{N}\sum_{i=1}^{N}(I_{\text{predicted,i}} - I_{\text{measured,i}})^2}}{\frac{1}{N}\sum_{i=1}^{N} I_{\text{measured,i}}} \tag{6.39}$$

where k is the coverage factor, equal to 1.96 for a 95% confidence level (note that the calculation for U_{95} follows the usual RMSE, without subtracting MBE). I_{measured} is a general notation for all the measured quantities. Table 6.1 shows the MBE, $\mathrm{RMSE}_{\text{rel, no bias}}$ and U_{95} for tilted solar irradiance prediction using ten transposition models as S111a and S111b.

The results shown in Table 6.1 are separated into all-sky condition and clear-sky conditions to further elaborate on the errors. We use two indices, namely, clearness index ε and brightness index Δ, to select data to determine the clear sky situation. Both ε and Δ are defined by Perez (Perez et al., 1990). Their formulations are shown in Appendix. We consider the sky to be clear if $\varepsilon > 5.0$ and brightness index $\Delta < 0.12$ (Robledo and Soler, 2000). We can observe from Table 6.1 that all transposition models perform better

Table 6.1: Performance of ten transposition models (converting from horizontal to tilted) over a period of one year, 2011. Horizontal irradiance components measurements from SPN1 are used as input, the output (converted global irradiance on tilted plane) is compared with silicon photosensor measurements.

Station	S111a	$s = 18.3°$	66° NE	S111b	$s = 6.1°$	246° SW
Model	MBE [Wm^{-2}]	RMSE [%]	U_{95} [%]	MBE [Wm^{-2}]	RMSE [%]	U_{95} [%]
All-sky, N=44495						
Isotropic						
Liu and Jordan	2.99	10.28	20.19	6.69	8.14	16.34
Badescu	-2.08	10.13	19.88	6.13	8.13	16.26
Tian	-13.15	10.02	20.68	0.46	8.11	15.89
Koronakis	4.78	10.34	20.40	6.88	8.14	16.37
Anisotropic						
Hay	6.78	8.55	17.09	5.47	8.17	16.27
Reindl	7.09	8.56	17.13	5.49	8.17	16.27
Temps and Coulson	25.56	10.22	23.64	26.12	9.74	23.39
Klucher	14.36	10.00	20.84	15.88	9.38	20.21
Perez	2.45	8.64	16.99	5.67	8.03	16.03
Skartveit and Olseth	6.27	8.58	17.09	5.41	8.13	16.28
Mean observed [Wm^{-2}]			398.59			369.62
Clear-sky, N=757						
Isotropic						
Liu and Jordan	-5.07	5.40	10.48	8.94	2.11	4.81
Badescu	-7.75	5.27	10.52	8.62	2.11	4.76
Tian	-13.59	5.20	10.77	5.48	2.11	4.40
Koronakis	-4.13	5.32	10.44	9.04	2.11	4.82
Anisotropic						
Hay	1.24	3.34	6.53	5.85	2.37	4.91
Reindl	1.35	3.33	6.54	5.86	2.37	4.91
Temps and Coulson	6.86	4.54	9.07	17.97	2.16	6.48
Klucher	6.54	4.56	9.10	17.75	2.16	6.43
Perez	5.54	4.12	8.21	9.45	2.11	5.04
Skartveit and Olseth	1.24	3.33	6.53	5.85	2.37	4.91
Mean observed [Wm^{-2}]			766.17			717.75

under clear-sky conditions due to a relatively isotropic sky and small diffuse components.

Some strong biases are observed for Klutcher model and Temps and Coulson model for both sky conditions. We display the scatter plots of modelled versus measured tilted irradiance at S111a and S111b in Figures 6.2 and 6.3 respectively using ten transposition models for all-sky conditions. The biases shown by the Klutcher model and the Temps and Coulson model are consistent with those reported in Table 6.1.

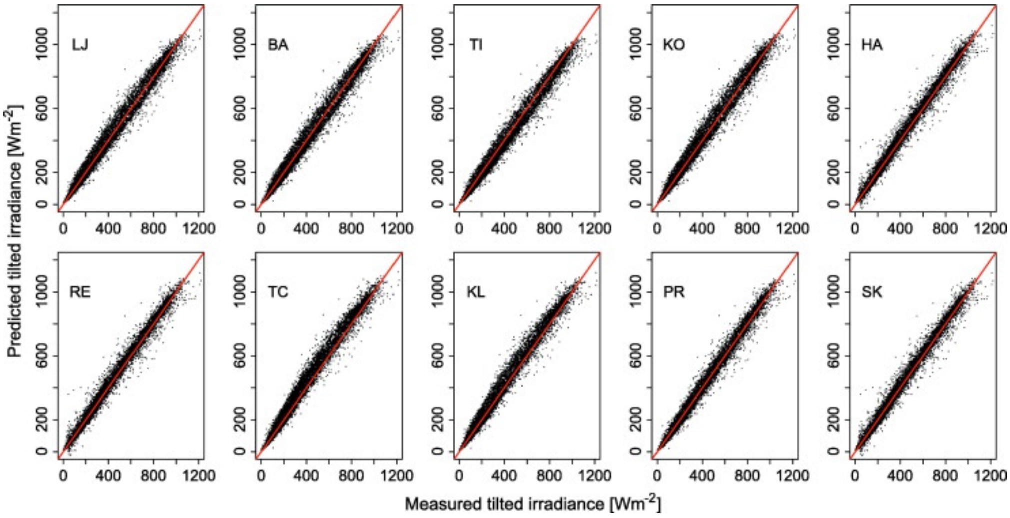

Figure 6.2: Scatter plots for modelled versus measured tilted irradiance at S111a using 10 transposition models for all-sky conditions. 2011 five minutes data are used. Abbreviations: Liu and Jordan (LJ), Badescu (BA), Tian (TI), Koronakis (KO), Hay (HA), Reindl (RE), Temps and Coulson (TC), Klucher (KL), Perez (PR) and Skartveit and Olseth (SK).

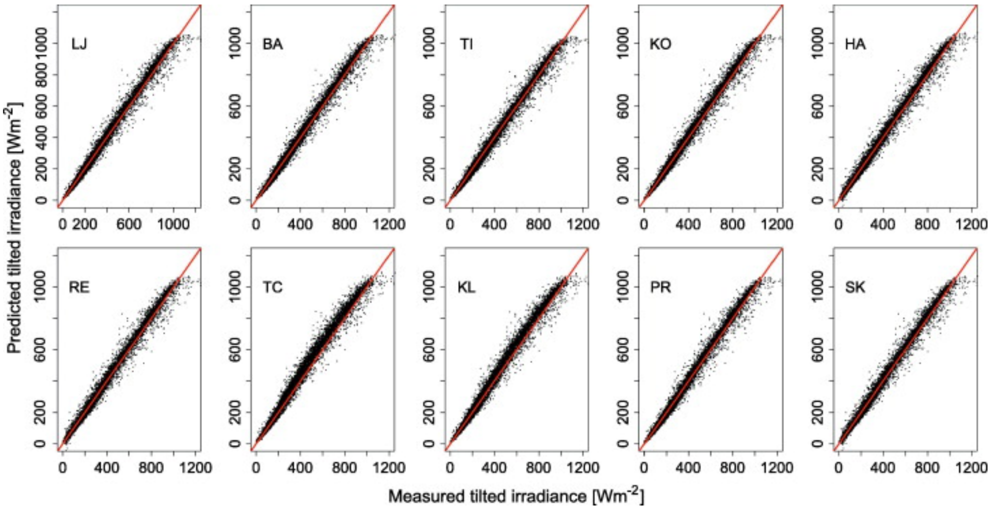

Figure 6.3: Scatter plots for modelled versus measured tilted irradiance at S111b using 10 transposition models for all-sky conditions.

6.2.1.3 Evaluation of Five Decomposition Models

We use decomposition models to predict DNI and DHI from GHI in situations when the DNI or DHI measurements are unavailable. Equation (6.28) suggests that if we know any two irradiance components, we can compute a unique value for the third component. We only show the prediction results of DHI. Table 6.2 shows the performance of five decomposition models over a period of one year, 2011. GHI measurements from the SPN1 pyranometer are used as inputs, and DNI is estimated using the various decomposition models: the output (predicted DHI) is compared with DHI measurements from the SPN1. The scatter plots of modelled versus measured DHI are shown in Figure 6.4.

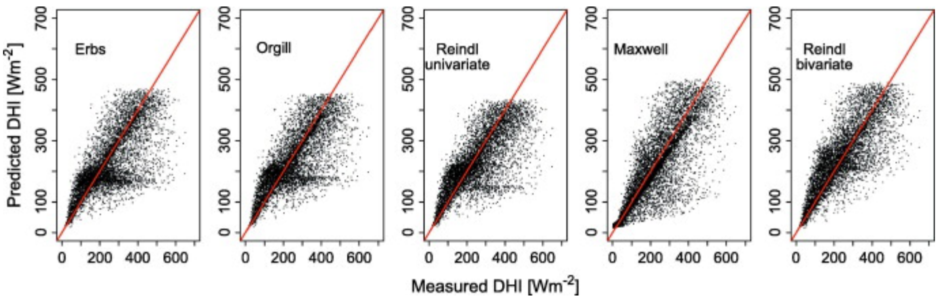

Figure 6.4: Scatter plots for modelled versus measured DHI at S111 using 5 decomposition models.

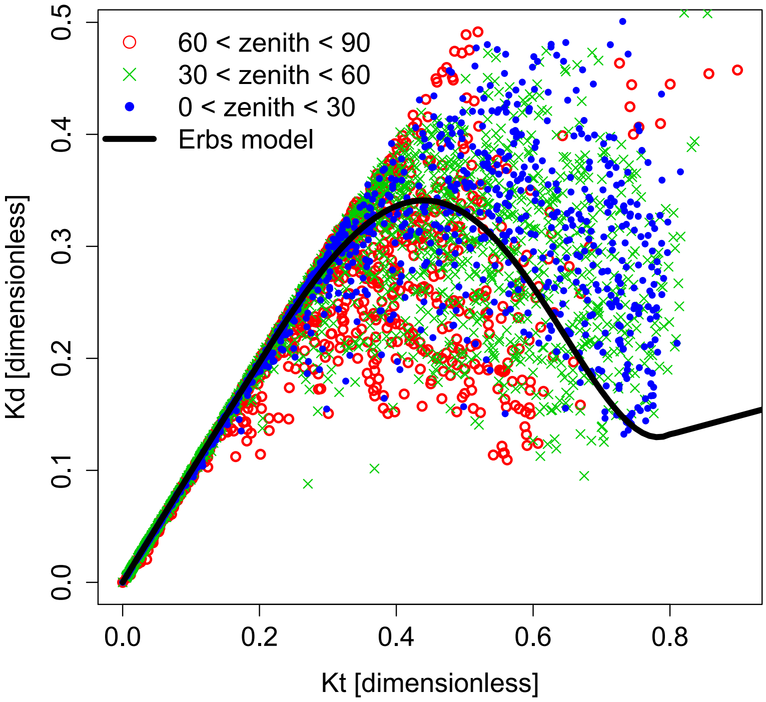

Figure 6.5: Scatter plot for K_{t}, K_{d} pairs during 2011 January under different zenith angle ranges. Erbs model is plotted to demonstrate the non-injective mapping from K_{t} to K_{d}.

Table 6.2: Performance of five decomposition models (predicting DHI from GHI in a tropical region) over a period of one year, 2011. Predicted DHI is compared to DHI measurements from SPN1 for error calculation.

Model	MBE [Wm^{-2}]	$\mathrm{RMSE}_{\mathrm{rel,\ no\ bias}}$ [%]	U_{95} [%]
All-sky, N=44495			
Erbs	-13.32	32.02	71.81
Orgill	-12.85	34.50	68.80
Reindl (univariate)	-13.74	34.71	69.37
Maxwell	-13.27	34.94	69.73
Reindl (bivariate)	0.43	31.76	62.26
Mean observed [Wm^{-2}]			195.49
Clear-sky, N=757			
Erbs	66.59	24.50	126.57
Orgill	76.26	25.89	143.37
Reindl (univariate)	85.97	22.00	157.21
Maxwell	97.36	43.29	191.07
Reindl (bivariate)	117.46	23.83	211.76
Mean observed [Wm^{-2}]			111.46

The large $\mathrm{RMSE}_{\mathrm{rel,\ no\ bias}}$ values obtained in Table 6.2 are consistent with the results from the many studies of the literature, which mostly use hourly data. The errors originate from the one-to-many mapping from GHI to DHI. Recall that GHI and DHI may also be represented using transmittance K_{t} and K_{d} (see Equation (6.29) and (6.30)). Figure 6.5 shows the scatter plot for K_{t}, K_{d} pairs during 2011 January under different zenith angle ranges. We observe that the possible range of K_{d} varies from 0.1 to 0.5 for K_{t} values greater than 0.1. The range of K_{d} is weakly dependent on zenith angle. As all the decomposition models describe a one-to-one mapping between K_{t} and K_{d}, a large $\mathrm{RMSE}_{\mathrm{rel,\ no\ bias}}$ is expected. The details of the one-to-many mapping could be found in the study by Ridley et al. (Ridley, Boland, and Lauret, 2010).

We conclude that more elaborate separation methods (e.g. Maxwell and Reindl bivariate models) do not out-perform the simpler ones (e.g. the Erbs, Orgill and Reindl univariate models). This conclusion is also observed by Gueymard in his comparison of models with mid-latitude data (Gueymard, 2009).

It is interesting to note that the decomposition models perform worse in clear sky conditions as compared to all-sky conditions. Large positive MBEs are observed for all models showing strong over-prediction. This is expected as: with the same K_t value, K_d is much smaller during a clear sky condition than cloudy conditions, i.e., clear sky conditions are very likely to be the points below the curve in Figure 6.5.

6.2.1.4 Combination of Decomposition Models and Transposition Models

We have shown in the previous section that decomposition models introduce large errors for DHI prediction. We now examine the effect of these errors on irradiance conversion by assuming DHI measurements are not available, i.e., GHI is used as the only input for conversion from horizontal to tilt in this section.

The four isotropic models used in Section 6.2.1.2 show similar accuracy for I_t prediction. Therefore we select the classic Liu and Jordan model to represent all isotropic models. As the Klucher model and the Temps model do not perform well, as shown in Table 6.1, we do not use these models in our analyses. We do not include the Hay model as it can be represented using the Skartveit and Olseth model when $\Omega = 0$ (see B). We only select three anisotropic models, namely, those of Perez, Reindl and Skartveit and Olseth.

Table 6.3 shows the MBE, RMSE and U_{95} for various combinations of transposition models and decomposition models over a period of one year,

Table 6.3: Performance of five decomposition models with four transposition models (converting from horizontal to tilted) over a period of one year, 2011. Only GHI measurements from SPN1 are used as input, DNI and DHI are estimated using various decomposition models, the output (converted global irradiance on tilted plane) is compared with silicon photosensor measurements.

Station	S111a	$s = 18.3°$	66° NE	S111b	$s = 6.1°$	246° SW
Model	MBE [Wm^{-2}]	RMSE [%]	U_{95} [%]	MBE [Wm^{-2}]	RMSE [%]	U_{95} [%]
Isotropic						
Liu and Jordan						
+ Erbs	0.86	11.25	22.05	7.18	8.25	16.60
+ Orgill	0.86	11.25	22.06	7.25	8.24	16.61
+ Reindl (univariate)	1.03	11.11	21.79	7.18	8.23	16.57
+ Maxwell	2.17	**10.48**	20.57	6.85	**8.23**	16.53
+ Reindl (bivariate)	1.41	11.30	22.16	7.49	8.25	16.66
Anisotropic						
Perez						
+ Erbs	0.91	10.02	19.65	6.29	8.17	16.36
+ Orgill	0.72	10.01	19.61	6.31	8.16	16.35
+ Reindl (univariate)	0.72	9.89	18.39	6.23	8.15	16.32
+ Maxwell	2.18	9.55	18.76	6.13	8.22	16.44
+ Reindl (bivariate)	0.70	9.93	19.47	6.41	8.16	16.35
Reindl						
+ Erbs	4.81	9.84	19.43	6.11	8.30	16.59
+ Orgill	5.12	9.79	19.36	6.16	8.31	16.61
+ Reindl (univariate)	6.27	**9.43**	18.70	6.97	7.99	16.03
+ Maxwell	8.80	10.05	20.08	6.74	8.12	16.22
+ Reindl (bivariate)	7.92	9.59	19.13	8.03	**7.90**	15.96
Skartveit and Olseth						
+ Erbs	4.02	9.85	19.41	6.04	8.31	16.59
+ Orgill	4.36	9.81	19.34	6.10	8.31	16.61
+ Reindl (univariate)	4.69	9.79	19.32	5.99	8.33	16.63
+ Maxwell	6.19	10.84	21.46	5.38	8.69	17.27
+ Reindl (bivariate)	5.47	10.13	20.03	6.22	8.42	16.83
Mean observed [Wm^{-2}]			398.59			369.62

2011. For this exercise, we use only GHI measurements from S111 as input for Equation (6.36). DHI and DNI components are estimated using decomposition models and the results (converted I_{t} values) are compared with the measurements from S111a and S111b separately.

We observe from Table 6.3, that the best performance using a combination of transposition models and decomposition models is given by Reindl plus the Reindl univariate model for S111a, Reindl plus the Reindl bivariate model for S111b. It is important to note that, for small inclination angles, for example S111b, the performance of anisotropic models is very similar to those using the isotropic approximation. We conclude that if various decomposition models are used to estimate DHI and DNI, there will be a small additional error (additional to the results from Table 6.1) in predicted I_{t} on planes.

Chapter 7

Conclusion and proposed future works

7.1 Summary

In this thesis, several novel techniques using statistical analysis and machine learning were proposed and applied to forecast solar irradiance.

In Chapter 3, a novel time series technique was applied to forecast high resolution solar irradiance data using an exponential smoothing state space (ESSS) model. To stationarize the solar irradiance data before applying linear time series models, an original Fourier trend model was proposed. The performance of the Fourier trend model was compared with other popular trend models using residual analysis and Kwiatkowski-Phillips-Schmidt-Shin (KPSS) stationary test. The KPSS values of the residual series of cosine trend and Gaussian trend were found to be higher than the critical value, indicating that the two series are not stationary. The residual series of Fourier trend and high order polynomial trend were found to be stationary, since their KPSS values are smaller than the critical value. However, the KPSS value of the residual series of Fourier trend is much smaller than that of the high order polynomial trend, which proves that the residual series of Fourier trend has a higher probability of obtaining stationarity. Therefore the Fourier trend model was used for subsequent forecasting. Using the optimized Fourier trend, the ESSS model was implemented to forecast the stationary residual series of Singapore and Colorado, USA. The climate of Colorado is temperate semi-arid, which contrasts to the humid tropical climate of Singapore. To compare the performance with other time series forecasting models, autoregressive integrated moving average (ARIMA), linear exponential smoothing (LES), simple exponential smoothing (SES) and random walk (RW) were also tested using the same data samples. The simulation results showed that the ESSS model has better performance than the other forecasting models. Finally, in order to discuss the reliability of the forecasting models in a real application, a complementary study on the forecasting 95% confidence interval and forecasting horizon of the ESSS model was performed. The ESSS model 95% confidence interval provides forecasting accuracy of around 90%, which indicates a level of accuracy useful for application by power system utilities. By comparing the forecasting horizon plots of different models, the ESSS model exhibits the widest range of low forecasting errors, which indicates the best performance when using less than 20 minute average data to predict up to 20 minutes ahead.

In Chapter 4, satellite image analysis and a novel hybrid forecasting technique were applied to forecast hourly resolution solar irradiance data using both the exponential smoothing state space (ESSS) model and the back propagation multilayer perceptron model. After analysing the satellite images, the self-organising map was used to perform the classification of cloud cover index. Using the derived cloud cover index, the ESSS model was implemented to forecast the next time step cloud cover index in Singapore and the back propagation multilayer perceptron model was applied to derive the solar irradiance from the cloud cover index forecast. To compare the performance with other time series forecasting models, ARIMA, LES, SES, and RW were also tested using the same data samples. The simulation results showed that the hybrid model has better performance than other forecasting models.

In Chapter 5, a novel hybrid forecasting technique was applied to forecast hourly resolution solar irradiance data using self-organizing maps, support vector regression and particle swarm optimization. Self-organizing maps were applied to partition the whole input space into several disjointed regions with different characteristic information on the correlation between the input and the output. Then support vector regression was used to model each disjointed region to identify the characteristic correlation. In order to reduce the performance volatility of support vector machines with different parameters, particle swarm optimization was implemented to automatically perform the parameter selection in support vector regression modelling.

In Chapter 6, techniques in spatial-temporal solar irradiance forecasting were proposed. In section 6.1, spatial-temporal covariance structures and time-forward kriging were introduced: the aim of this chapter was to devise a methodology to forecast solar irradiance over a wide area, using time series from a small number of monitoring stations as input. When the forecast irradiance is interpolated over the entire area, and combined with knowledge of PV systems located within it, short timescale PV power generation forecasts can be made. Such forecasts will soon be essential for power generation and grid management companies in Singapore, as the installed base of PV approaches a significant fraction of overall power generation.

The basis of our method lies in two transformations of the data: we first ensured temporal stationarity by detrending the data and applied a coordinate transformation to obtain spatial stationarity. After the data transformation, the predictive time-forward kriging can be investigated.

In section 6.2, a comparison of methods to convert solar irradiance measured at an arbitrary tilt to horizontal (and from horizontal to tilt) in the tropical region of Singapore was presented. Using observations, we evaluated the performance of ten transposition models and five decomposition models. Based on these results, we further developed algorithms to convert solar irradiance from tilt to horizontal.

Each PV system is likely to possess a simple irradiance measurement equipment (e.g. silicon sensor) for performance ratio and yield assessments. Very often, only data from an inclined plane are available. For good forecasts, data from various locations must be converted to horizontal irradiance in order to accurately capture the spatio-temporal dynamics. Our conversion algorithm can be used to transform tilted irradiance measurements to GHI and thus greatly increase the database for such forecasts, which will soon be essential for the management of many electricity grids.

7.2 Novel contributions

In Chapter 3, the novel contribution is the proposed ESSS model with Fourier trend preprocessing to forecast short-term solar irradiance. Compared with other popular statistical time series models like ARIMA, LES, SES and RW, the ESSS model has better forecasting accuracy in general for the forecasting horizon from 5 to 20 minutes. This timescale is one of great interest to power grid operators. Even a marginal improvement in forecasting accuracy on this timescale can represent huge cost savings in grid operation. Moreover, our novel formulation of the Fourier trend model also outperforms other similar trend models.

In Chapter 4, the novel contribution is the proposed SOM+ESSS+MLP hybrid model with satellite image preprocessing to forecast medium-term solar irradiance. Compared with other popular statistical time series models like ARIMA, LES, SES and RW, the proposed model has superior forecasting accuracy for hourly solar irradiance.

In Chapter 5, the novel contribution is the proposed SOM+SVR+PSO hybrid model to forecast medium-term solar irradiance without satellite images. To compare the performance with other time series forecasting models, the hybrid model has generally better performance than other statistical forecasting models in hourly solar irradiance forecasting.

In Chapter 6, the novel contribution is the proposed spatial-temporal solar irradiance analysis. This analysis provides a scientific way to predict solar irradiance at locations without monitoring stations. The methodology presented here was useful when high spatial resolution irradiance data are available.

7.3 Proposed future works

All the models in this thesis were developed based on the data available at different times. SERIS now has additional equipment like total sky imager (TSI) available for short-term solar irradiance forecasting. The local cloud cover information can be derived directly from the series of sky images provided by the TSI. This important additional information input will improve the forecasting accuracy from our statistical time series analysis based on the ESSS model. It is also possible to analyse local sky images from TSI together with satellite images to generate more accurate hourly cloud information and identify the pattern using machine learning models.

More solar irradiance monitoring stations have also been set up in the past 12 months.SERIS now has 25 monitoring stations all across Singapore, as shown in Figure 7.1. This enables SERIS to analyse spatial-temporal data more accurately. Even though SERIS have a solid method to achieve both spatial and temporal stationarity, the spatial-temporal forecasting methodology can still be further investigated and improved by machine learning techniques.

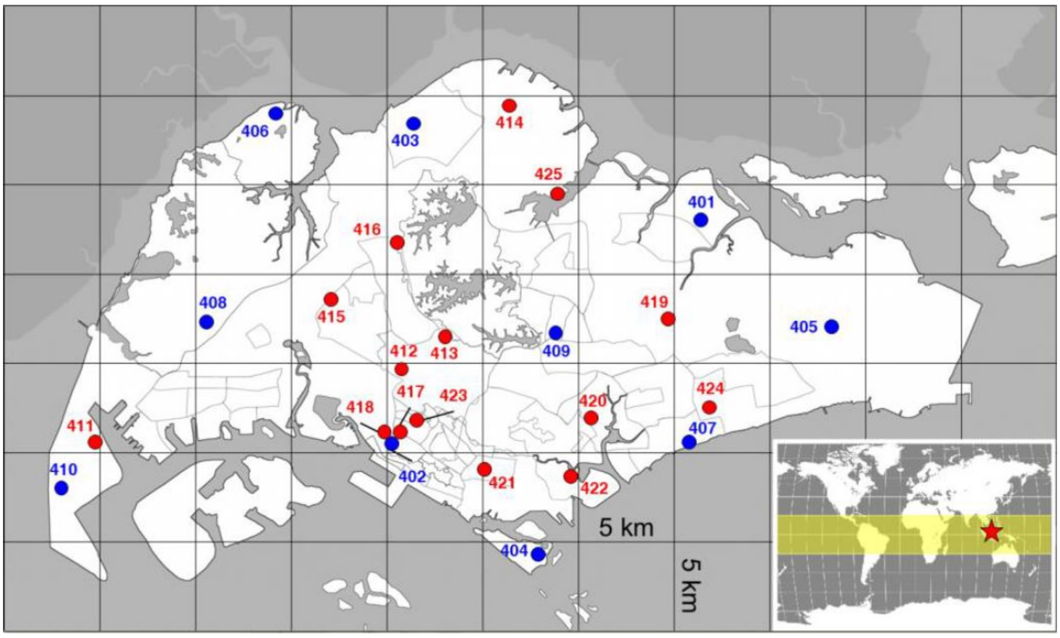

Figure 7.1: 25 solar irradiance monitoring stations in Singapore in 2015

With abundant information input and various forecasting models developed, it is also possible to investigate the stacking models. Stacking is a machine learning method to combine several different forecasting models. These models are trained with the available input data and generate corresponding forecasting outputs. The outputs are then becoming the input of a stacking learning model to make a final prediction.

References

[Abdel Hady, Schwenker, and Palm2010] Abdel Hady, Mohamed Farouk, Friedhelm Schwenker, and Ganther Palm. 2010. Semi-supervised learning for tree-structured ensembles of RBF networks with co-training. *Neural Networks*, 23(4):497–509, May.

[Abraham and Ledolter1983] Abraham, B. and J. Ledolter. 1983. *Statistical methods for forecasting.* John Wiley and Sons, New York.

[Al-Sadah, Ragab, and Arshad1990a] Al-Sadah, F. H., F. M. Ragab, and M. K. Arshad. 1990a. Hourly solar radiation over bahrain. *Energy*, 15:395.

[Al-Sadah, Ragab, and Arshad1990b] Al-Sadah, Fayez H, Farouk M Ragab, and Mirza K Arshad. 1990b. Hourly solar radiation over bahrain. *Energy*, 15(5):395 – 402.

[Amrouche and Pivert2014] Amrouche, Badia and Xavier Le Pivert. 2014. Artificial neural network based daily local forecasting for global solar radiation. *Applied Energy*, 130:333 – 341.

[Bacher, Madsen, and Nielsen2009] Bacher, Peder, Henrik Madsen, and Henrik Aalborg Nielsen. 2009. Online short-term solar power forecasting. *Solar Energy*, 83(10):1772 – 1783.

[Badescu2002] Badescu, V. 2002. 3d isotropic approximation for solar diffuse irradiance on tilted surfaces. *Renewable Energy*, 26(2):221 – 233.

[Bahadori and Nwaoha2013] Bahadori, Alireza and Chikezie Nwaoha. 2013. A review on solar energy utilisation in australia. *Renewable and Sustainable Energy Reviews*, 18:1 – 5.

[Baig, Achter, and Mufti1991] Baig, A., P. Achter, and A. Mufti. 1991. A novel approach to estimate the clear day global radiation. *Renewable Energy*, 1:119–123.

[Baig, Akhter, and Mufti1991] Baig, A., P. Akhter, and A. Mufti. 1991. A novel approach to estimate the clear day global radiation. *Renewable Energy*, 1(1):119 – 123.

[Bechini et al.2000] Bechini, Luca, Giorgio Ducco, Marcello Donatelli, and Alfred Stein. 2000. Modelling, interpolation and stochastic simulation in space and time of global solar radiation. *Agriculture, Ecosystems & Environment*, 81(1):29 – 42.

[Bernecker et al.2014] Bernecker, David, Christian Riess, Elli Angelopoulou, and Joachim Hornegger. 2014. Continuous short-term irradiance forecasts using sky images. *Solar Energy*, 110:303 – 315.

[Beyer, Costanzo, and Heinemann1996] Beyer, Hans Georg, Claudio Costanzo, and Detlev Heinemann. 1996. Modifications of the heliosat procedure for irradiance estimates from satellite images. *Solar Energy*, 56(3):207 – 212.

[Blanc et al.2014] Blanc, P., B. Espinar, N. Geuder, C. Gueymard, R. Meyer, R. Pitz-Paal, B. Reinhardt, D. Renné, M. Sengupta, L. Wald, and S. Wilbert. 2014. Direct normal irradiance related definitions and applications: The circumsolar issue. *Solar Energy*, 110:561 – 577.

[Bland and Clayton1994] Bland, W.L. and M.K. Clayton. 1994. Spatial structure of solar radiation in wisconsin. *Agricultural and Forest Meteorology*, 69:75 – 84.

[Boland, David, and Lauret2016] Boland, John, Mathieu David, and Philippe Lauret. 2016. Short term solar radiation forecasting: Island versus continental sites. *Energy*, 113:186 – 192.

[Bookstein1989] Bookstein, F.L. 1989. Principal warps: Thin-plate splines and the decomposition of deformations. *IEEE Transactions on Pattern Analysis and Machine Intelligence*, 11:567–585.

[Box, Jenkins, and Reinsel1970] Box, G. E. P., G. M. Jenkins, and G. C. Reinsel. 1970. *Time Series Analysis: Forecasting and Control.* Prentice Hall, Inc., Englewood Cliffs–New Jersey.

[Brown1959] Brown, R. G. 1959. *Statistical forecasting for inventory control.* McGraw-Hill, New York.

[Brown1963] Brown, R. G. 1963. *Smoothing, forecasting and prediction of discrete time series.* Prentice-Hall, New Jersey.

[Cano et al.1986] Cano, D., J.M. Monget, M. Albuisson, H. Guillard, N. Regas, and L. Wald. 1986. A method for the determination of the global solar radiation from meteorological satellite data. *Solar Energy*, 37(1):31 – 39.

[Chow et al.2011] Chow, Chi Wai, Bryan Urquhart, Matthew Lave, Anthony Dominguez, Jan Kleissl, Janet Shields, and Byron Washom. 2011. Intra-hour forecasting with a total sky imager at the {UC} san diego solar energy testbed. *Solar Energy*, 85(11):2881 – 2893.

[Chu, Pedro, and Coimbra2013] Chu, Yinghao, Hugo T.C. Pedro, and Carlos F.M. Coimbra. 2013. Hybrid intra-hour {DNI} forecasts with sky image processing enhanced by stochastic learning. *Solar Energy*, 98, Part C:592 – 603.

[Chu et al.2015] Chu, Yinghao, Bryan Urquhart, Seyyed M.I. Gohari, Hugo T.C. Pedro, Jan Kleissl, and Carlos F.M. Coimbra. 2015. Short-term reforecasting of power output from a 48 {MWe} solar {PV} plant. *Solar Energy*, 112:68 – 77.

[Cox and Cox1994] Cox, T. F. and M. A. A. Cox. 1994. *Multidimensional Scaling.* Chapman & Hall, Boundary Row–London.

[Cressie and Wikle2011] Cressie, N. and C.K. Wikle. 2011. *Statistics for*

Spatio-Temporal Data. Wiley Series in Probability and Statistics. Wiley.

[David, Lauret, and Boland2013] David, Mathieu, Philippe Lauret, and John Boland. 2013. Evaluating tilted plane models for solar radiation using comprehensive testing procedures, at a southern hemisphere location. *Renewable Energy*, 51(0):124 – 131.

[Diabat, Moussu, and Wald1989] Diabat, L., G. Moussu, and L. Wald. 1989. Description of an operational tool for determining global solar radiation at ground using geostationary satellite images. *Solar Energy*, 42(3):201 – 207.

[Diagne et al.2014] Diagne, Maimouna, Mathieu David, John Boland, Nicolas Schmutz, and Philippe Lauret. 2014. Post-processing of solar irradiance forecasts from {WRF} model at reunion island. *Solar Energy*, 105:99 – 108.

[Diagne et al.2013] Diagne, Maimouna, Mathieu David, Philippe Lauret, John Boland, and Nicolas Schmutz. 2013. Review of solar irradiance forecasting methods and a proposition for small-scale insular grids. *Renewable and Sustainable Energy Reviews*, 27:65 – 76.

[Dickey and Fuller1981] Dickey, D. A. and W. A. Fuller. 1981. Likelihood ratio statistics for autoregressive time series with a unit root. *Econometrica*, 49:1057–1072.

[Dorvlo, Jervase, and Al-Lawati2002] Dorvlo, Atsu S.S., Joseph A. Jervase, and Ali Al-Lawati. 2002. Solar radiation estimation using artificial neural networks. *Applied Energy*, 71(4):307 – 319.

[Du and Ma2013] Du, Juan and Chunsheng Ma. 2013. Vector random fields with compactly supported covariance matrix functions. *Journal of Statistical Planning and Inference*, 143(3):457 – 467.

[Duffie and Beckman2006] Duffie, John A. and William A. Beckman. 2006. *Solar Engineering of Thermal Processes.* John Wiley & Sons, Inc.

[Eberhart and Kennedy1995] Eberhart, R. and J. Kennedy. 1995. A new optimizer using particle swarm theory. In , *Proceedings of the Sixth International Symposium on Micro Machine and Human Science, 1995. MHS '95*, pages 39–43.

[Elizondo, Hoogenboom, and McClendon1994] Elizondo, David, Gerrit Hoogenboom, and R.W. McClendon. 1994. Development of a neural network model to predict daily solar radiation. *Agricultural and Forest Meteorology*, 71(1):115–132.

[Elminir, Areed, and Elsayed2005] Elminir, Hamdy K., Faiz F. Areed, and Tarek S. Elsayed. 2005. Estimation of solar radiation components incident on helwan site using neural networks. *Solar Energy*, 79(3):270 – 279.

[Erbs, Klein, and Duffie1982] Erbs, D. G., S. A. Klein, and J. A. Duffie. 1982. Estimation of the diffuse radiation fraction for hourly, daily and monthly-average global radiation. *Solar Energy*, 28(4):293 – 302.

[Evseev and Kudish2009] Evseev, E. G. and A. I. Kudish. 2009. The assessment of different models to predict the global solar radiation on a surface tilted to the south. *Solar Energy*, 83:377–388.

[Faiman, Feuermann, and Zemel1993] Faiman, D., D. Feuermann, and A. Zemel. 1993. Site-independent algorithm for obtaining the direct beam insolation from a multipyranometer instrument. *Solar Energy*, 50(1):53 – 57.

[Finkenstädt, Held, and Isham2006] Finkenstädt, B., L. Held, and V. Isham. 2006. *Statistical Methods for Spatio-Temporal Systems.* Monographs on Statistics and Applied Probability. Chapman & Hall/CRC.

[Gardner1985] Gardner, E. S. 1985. Exponential smoothing: The state of the art. *Journal of Forecasting*, 4:1–38.

[Garrison1985] Garrison, J. D. 1985. A study of the division of global irradiance into direct and diffuse irradiance at thirty-three u.s. sites. *Solar Energy*, 35(4):341 – 351.

[Garrison and Sahami1995] Garrison, John D. and Kamran Sahami. 1995. A study of the division of global irradiance into direct beam and diffuse irradiance at seven canadian sites. *Solar Energy*, 55(6):493 – 504.

[Gass and Harris2000] Gass, S. I. and C. M. Harris. 2000. *Encyclopedia of operations research and management science*. Kluwer, The Netherlands.

[Glasbey, Graham, and Hunter2001] Glasbey, C.A., R. Graham, and A.G.M. Hunter. 2001. Spatio-temporal variability of solar energy across a region: a statistical modelling approach. *Solar Energy*, 70(4):373 – 381.

[Gneiting2002] Gneiting, Tilmann. 2002. Nonseparable, stationary covariance functions for space-time data. *Journal of the American Statistical Association*, 97(458):pp. 590–600.

[Gneiting, Genton, and Guttorp2006] Gneiting, Tilmann, Marc Genton, and Peter Guttorp. 2006. Geostatistical space-time models, stationarity, separability, and full symmetry. In B. Finkenstadt, L. Held, and V. Isham, editors, *Statistical Methods for Spatio-Temporal Systems*. Chapman and Hall/CRC, chapter 4, pages 151–175.

[Gneiting, Genton, and Guttorp2007] Gneiting, Tilmann, Marc G. Genton, and Peter Guttorp. 2007. Geostatistical space-time models, stationarity, separability and full symmetry. Technical Report 475, Department of Statistics, University of Washington.

[Gueymard2009] Gueymard, C. A. 2009. Direct and indirect uncertainties in the prediction of tilted irradiance for solar engineering applications. *Solar Energy*, 83(3):432–444.

[Gueymard and Wilcox2011] Gueymard, Christian A. and Stephen M. Wilcox. 2011. Assessment of spatial and temporal variability in the us solar resource from radiometric measurements and predictions from models using ground-based or satellite data. *Solar Energy*, 85(5):1068 – 1084.

[Haslett and Raftery1989] Haslett, John and Adrian E. Raftery. 1989. Space-time modelling with long-memory dependence: Assessing ireland's wind power resource. *Journal of the Royal Statistical Society. Series C (Applied Statistics)*, 38(1):1–50.

[Hay1979] Hay, J. E. 1979. Calculation of monthly mean solar radiation for horizontal and inclined surfaces. *Solar Energy*, 23(4):301 – 307.

[Holt2004] Holt, C. C. 2004. Forecasting seasonals and trends by exponentially weighted moving averages. *International Journal of Forecasting*, 20:5–10.

[Hontoria, Aguilera, and Zufiria2002] Hontoria, L, J Aguilera, and P Zufiria. 2002. Generation of hourly irradiation synthetic series using the neural network multilayer perceptron. *Solar Energy*, 72(5):441 – 446.

[Hyndman et al.2002] Hyndman, R. J., A. B. Koehler, R. D. Snyder, and S. Grose. 2002. A state space framework for automatic forecasting using exponential smoothing methods. *International Journal of Forecasting*, 18:439–454.

[Hyun, Burman, and Paul2012] Hyun, Jung Won, Prabir Burman, and Debashis Paul. 2012. A regression approach for estimating the parameters of the covariance function of a stationary spatial random process. *Journal of Statistical Planning and Inference*, 142(8):2330 – 2344.

[Inman, Pedro, and Coimbra2013] Inman, Rich H., Hugo T.C. Pedro, and Carlos F.M. Coimbra. 2013. Solar forecasting methods for renewable energy integration. *Progress in Energy and Combustion Science*, 39(6):535 – 576.

[Inoue, Sasaki, and Washio2012] Inoue, Tsuyoshi, Tetsuo Sasaki, and Takashi Washio. 2012. Spatio-temporal kriging of solar radiation incorporating direction and speed of cloud movement. In *The 26th Annual Conference of the Japanese Society for Artificial Intelligence*, Yamaguchi city. `<http://kaigi.org/jsai/webprogram/2012/pdf/708.pdf>`.

[Janjai, Sricharoen, and Pattarapanitchai2011] Janjai, S., K. Sricharoen, and S. Pattarapanitchai. 2011. Semi-empirical models for the estimation of clear sky solar global and direct normal irradiances in the tropics. *Applied Energy*, 88:4749–4755.

[Jiang et al.2015] Jiang, He, Yao Dong, Jianzhou Wang, and Yuqin Li. 2015. Intelligent optimization models based on hard-ridge penalty and {RBF} for forecasting global solar radiation. *Energy Conversion and Management*, 95:42 – 58.

[Kaplanis2006] Kaplanis, S.N. 2006. New methodologies to estimate the hourly global solar radiation; comparisons with existing models. *Renewable Energy*, 31(6):781 – 790.

[KEMMOKU et al.1999] KEMMOKU, Y, S ORITA, S NAKAGAWA, and T SAKAKIBARA. 1999. Daily insolation forecasting using a multistage neural network. *Solar Energy*, 66(3):193 – 199.

[Kent and Mardia1994] Kent, J. T. and K. V. Mardia. 1994. The link between kriging and thin-plate splines. In F. P. Kelly, editor, *Probability, statistics, and optimisation : a tribute to Peter Whittle*. John Wiley & Sons, Inc., Baffins Lane–Chichester, pages 325–339.

[Klucher1979] Klucher, T. M. 1979. Evaluation of models to predict insolation on tilted surfaces. *Solar Energy*, 23:111 – 114.

[Kohonen2013] Kohonen, Teuvo. 2013. Essentials of the self-organizing map. *Neural Networks*, 37:52–65, January.

[Koronakis1986] Koronakis, P. S. 1986. On the choice of the angle of tilt for south facing solar collectors in the athens basin area. *Solar Energy*, 36(3):217 – 225.

[Kruskal1964a] Kruskal, J. 1964a. Multidimensional scaling by optimizing goodness of fit to a nonmetric hypothesis. *Psychometrika*, 29(1):1–27, March.

[Kruskal1964b] Kruskal, J. 1964b. Nonmetric multidimensional scaling: A numerical method. *Psychometrika*, 29(2):115–129, June.

[Kwiatkowski, Phillips, and Schmidt1992] Kwiatkowski, Denis, Peter C. B. Phillips, and Peter Schmidt. 1992. Testing the null hypothesis of stationarity against the alternative of a unit root: How sure are we that economic time series have a unit root? *Journal of Econometrics*, 54:159 – 178.

[Kwiatkowski et al.1992] Kwiatkowski, Denis, Peter C.B. Phillips, Peter Schmidt, and Yongcheol Shin. 1992. Testing the null hypothesis of stationarity against the alternative of a unit root: How sure are we that economic time series have a unit root? *Journal of Econometrics*, 54(13):159 – 178.

[Le and Zidek2006] Le, Nhu D. and James V. Zidek. 2006. *Statistical Analysis of Environmental Space-Time Processes*. Springer. ISBN 0-387-26209-1.

[Lentz et al.2014] Lentz, Alvaro, David Renné, Richard Perez, Thomas Hoff, John Dise, David Chalmers, and Sergey Kivalov. 2014. 2013 ises solar world congress the cost of mitigating short-term pv output variability. *Energy Procedia*, 57:755 – 762.

[Liu and Jordan1962] Liu, B. Y. H. and R. C. Jordan. 1962. Daily insolation on surfaces tilted towards the equator. *Trans ASHRAE*, 67:526–541.

[Lorenz et al.2009] Lorenz, E., J. Hurka, D. Heinemann, and H.G. Beyer. 2009. Irradiance forecasting for the power prediction of grid-connected photovoltaic systems. *Selected Topics in Applied Earth Observations and Remote Sensing, IEEE Journal of*, 2(1):2 –10, march.

[Lorenz, Kühnert, and Heinemann2014] Lorenz, Elke, Jan Kühnert, and Detlev Heinemann, 2014. *Overview of Irradiance and Photovoltaic Power Prediction*, pages 429–454. Springer New York, New York, NY.

[Luna and Genton2005] Luna, Xavier De and Marc G. Genton. 2005. Predictive spatio-temporal models for spatially sparse environmental data. `<http://www3.stat.sinica.edu.tw/statistica/oldpdf/A15n213.pdf>`. (accessed 09.01.2013).

[M. Santamouris and Asimakopoulos1999] M. Santamouris, G. Mihalakakou, B. Psiloglou G. Eftaxias and D. N. Asimakopoulos. 1999. Modeling the global solar radiation on the earth surface using atmospheric deterministic and intelligent data-driven techniques. *Journal of Climate*, 12:3105 – 3116.

[Marquez and Coimbra2011] Marquez, Ricardo and Carlos F.M. Coimbra. 2011. Forecasting of global and direct solar irradiance using stochastic learning methods, ground experiments and the NWS database. *Solar Energy*, 85(5):746–756, May.

[Martín et al.2010] Martín, L., L. F. Zarzalejo, J Polo, A. Navarro, R. Marchante, and M. Cony. 2010. Prediction of global solar irradiance based on time series analysis: Application to solar thermal power plants energy production planning. *Solar Energy*, 84:1772–1781.

[Martinez-Anido et al.2016] Martinez-Anido, Carlo Brancucci, Benjamin Botor, Anthony R. Florita, Caroline Draxl, Siyuan Lu, Hendrik F. Hamann, and Bri-Mathias Hodge. 2016. The value of day-ahead solar power forecasting improvement. *Solar Energy*, 129:192 – 203.

[Martins, Pereira, and Abreu2007] Martins, F.R., E.B. Pereira, and S.L. Abreu. 2007. Satellite-derived solar resource maps for brazil under swera project. *Solar Energy*, 81(4):517 – 528.

[Masters2004] Masters, G. M. 2004. *Renewable and Efficient Electric Power Systems*. John Wiley & Sons, Inc., Hoboken–New Jersey.

[Maxwell1987] Maxwell, E. L. 1987. Quasi-physical model for converting hourly global horizontal to direct normal insolation. `<http://www.nrel.gov/docs/leg-osti/old/3087.pdf>`. (accessed 25.01.2012).

[Measurement and Instrumentation Data Center (MIDC), NREL2012] Measurement and Instrumentation Data Center (MIDC), NREL. 2012. South park colorado solar irradiance 5-min data set. `<http://www.nrel.gov/midc/spmd/>`. (accessed 16.02.2012).

[Mellit, Benghanem, and Kalogirou2006] Mellit, A., M. Benghanem, and S.A. Kalogirou. 2006. An adaptive wavelet-network model for forecasting daily total solar-radiation. *Applied Energy*, 83(7):705 – 722.

[Mellit et al.2010] Mellit, A., H. Eleuch, M. Benghanem, C. Elaoun, and A. Massi Pavan. 2010. An adaptive model for predicting of global, direct and diffuse hourly solar irradiance. *Energy Convers. Mgmt*, 51:771–782.

[Mercer1909] Mercer, J. 1909. Functions of positive and negative type, and their connection with the theory of integral equations. *Proceedings of* *the Royal Society of London. Series A, Containing Papers of a Mathematical and Physical Character*, 83(559):69–70, November. Article-Type: research-article / Full publication date: Nov. 3, 1909 / Copyright ? 1909 The Royal Society.

[Meteorological Satellite Center (MSC), Japan Meteorological Agency (JMA)2013] Meteorological Satellite Center (MSC), Japan Meteorological Agency (JMA). 2013. Gsics mtsat navigation and calibration monitoring. `<http://mscweb.kishou.go.jp/monitoring/calibration.htm>`. (accessed 25.03.2013).

[Mihalakakou, Santamouris, and Asimakopoulos2000] Mihalakakou, G., M. Santamouris, and D. N. Asimakopoulos. 2000. The total solar radiation time series simulation in athens, using neural networks. *Theoretical and Applied Climatology*, 66(3-4):185–197.

[Moreno-Muñoz et al.2008] Moreno-Muñoz, A., J. J. G. de la Rosa, R. Posadillo, and V. Pallarés. 2008. Short term forecasting of solar radiation. In *IEEE International Symposium on Industrial Electronics*, pages 1537–1541, Cambridge.

[Muth1960] Muth, J. F. 1960. Optimal properties of exponentially weighted forecasts. *Journal of American Statistical Association*, 55:299–306.

[National Climate Change Strategy (NCCS)2014] National Climate Change Strategy (NCCS). 2014. Solar energy technology primer: A summary. `<http://www.nccs.gov.sg/>`. (accessed 14.07.2015).

[Newport2014] Newport. 2014. Introduction to solar radiation. `<http://www.newport.com/Introduction-to-Solar-Radiation/411919/1033/content.aspx>`. (accessed 01.08.2015).

[Noorian, Moradi, and Kamali2008] Noorian, Ali Mohammad, Isaac Moradi, and Gholam Ali Kamali. 2008. Evaluation of 12 models to estimate hourly diffuse irradiation on inclined surfaces. *Renewable Energy*, 33(6):1406 – 1412.

[NREL2008] NREL. 2008. Solar position algorithm, Jan.

[Ord, Koehler, and Snyder1997] Ord, JK, AB Koehler, and RD Snyder. 1997. Estimation and prediction for a class of dynamic nonlinear statistical models. *Journal of the American Statistical Association*, 92(440):1621–1629, DEC.

[Orgill and Hollands1977] Orgill, J. F. and K. G. T. Hollands. 1977. Correlation equation for hourly diffuse radiation on a horizontal surface. *Solar Energy*, 19(4):357 – 359.

[Padovan and Col2010] Padovan, Andrea and Davide Del Col. 2010. Measurement and modeling of solar irradiance components on horizontal and tilted planes. *Solar Energy*, 84(12):2068 – 2084.

[Paoli et al.2010] Paoli, C., C. Voyant, M. Muselli, and M. L. Nivet. 2010. Forecasting of preprocessed daily solar radiation time series using neural networks. *Solar Energy*, 84:2146–2160.

[Pereira et al.2000] Pereira, E.B., F.R. Martins, S.L. Abreu, P. Couto, R. Stuhlmann, and S. Colle. 2000. Effects of burning of biomass on satellite estimations of solar irradiation in brazil. *Solar Energy*, 68(1):91 – 107.

[Perez et al.2004] Perez, Richard, Pierre Ineichen, Marek Kmiecik, Kathleen Moore, David Renne, and Ray George. 2004. Producing satellite-derived irradiances in complex arid terrain. *Solar Energy*, 77(4):367 – 371. <ce:title>The American Solar Energy Society's Solar 2003 Special Issue</ce:title>.

[Perez et al.1990] Perez, Richard, Pierre Ineichen, Robert Seals, Joseph Michalsky, and Ronald Stewart. 1990. Modeling daylight availability and irradiance components from direct and global irradiance. *Solar Energy*, 44(5):271 – 289.

[Perez et al.2012] Perez, Richard, Sergey Kivalov, Jim Schlemmer, Karl Hemker Jr., and Thomas E. Hoff. 2012. Short-term irradiance variability: Preliminary estimation of station pair correlation as a function of distance. *Solar Energy*, 86(8):2170 – 2176.

[R Development Core Team2011] R Development Core Team, 2011. *R: A Language and Environment for Statistical Computing*. R Foundation for Statistical Computing, Vienna, Austria. ISBN 3-900051-07-0.

[Rehman and Ghori2000] Rehman, Shafiqur and Saleem G Ghori. 2000. Spatial estimation of global solar radiation using geostatistics. *Renewable Energy*, 21:583 – 605.

[Reikard2009a] Reikard, G. 2009a. Predicting solar radiation at high resolutions: A comparison of time series forecasts. *Solar Energy*, 83:342–349.

[Reikard2009b] Reikard, Gordon. 2009b. Predicting solar radiation at high resolutions: A comparison of time series forecasts. *Solar Energy*, 83(3):342 – 349.

[Reindl, Beckman, and Duffie1990a] Reindl, D. T., W. A. Beckman, and J. A. Duffie. 1990a. Diffuse fraction correlations. *Solar Energy*, 45(1):1 – 7.

[Reindl, Beckman, and Duffie1990b] Reindl, D. T., W. A. Beckman, and J. A. Duffie. 1990b. Evaluation of hourly tilted surface radiation models. *Solar Energy*, 45(1):9 – 17.

[Renno, Petito, and Gatto2015] Renno, C., F. Petito, and A. Gatto. 2015. Artificial neural network models for predicting the solar radiation as input of a concentrating photovoltaic system. *Energy Conversion and Management*, 106:999 – 1012.

[Ridley, Boland, and Lauret2010] Ridley, Barbara, John Boland, and Philippe Lauret. 2010. Modelling of diffuse solar fraction with multiple predictors. *Renewable Energy*, 35(2):478 – 483.

[Righini, Gallegos, and Raichijk2005] Righini, R., H. Grossi Gallegos, and C. Raichijk. 2005. Approach to drawing new global solar irradiation contour maps for argentina. *Renewable Energy*, 30(8):1241 – 1255.

[Rigollier, Lefvre, and Wald2004] Rigollier, C, M Lefvre, and L Wald. 2004. The method heliosat-2 for deriving shortwave solar radiation from satellite images. *Solar Energy*, 77(2):159 – 169.

[Rigollier, Bauer, and Wald2000] Rigollier, Christelle, Olivier Bauer, and Lucien Wald. 2000. On the clear sky model of the esra (european solar radiation atlas) with respect to the heliosat method. *Solar Energy*, 68(1):33 – 48.

[Robaa2008] Robaa, S.M. 2008. Evaluation of sunshine duration from cloud data in egypt. *Energy*, 33(5):785–795, May.

[Roberts1982] Roberts, S. A. 1982. A general class of holt-winters type forecasting models. *Management Science*, 28:808–820.

[Robledo and Soler2000] Robledo, L. and A. Soler. 2000. Luminous efficacy of global solar radiation for clear skies. *Energy Conversion and Management*, 41:1769–1779.

[Sampson and Guttorp1992] Sampson, Paul D. and Peter Guttorp. 1992. Nonparametric estimation of nonstationary spatial covariance structure. *Journal of the American Statistical Association*, 87(417):108 – 119.

[Sfetsos and Coonick2000] Sfetsos, A. and A.H. Coonick. 2000. Univariate and multivariate forecasting of hourly solar radiation with artificial intelligence techniques. *Solar Energy*, 68(2):169 – 178.

[Sharma et al.2016] Sharma, Vishal, Dazhi Yang, Wilfred Walsh, and Thomas Reindl. 2016. Short term solar irradiance forecasting using a mixed wavelet neural network. *Renewable Energy*, 90:481 – 492.

[Simpson and Clifton2016] Simpson, Genevieve and Julian Clifton. 2016. Subsidies for residential solar photovoltaic energy systems in western australia: Distributional, procedural and outcome justice. *Renewable and Sustainable Energy Reviews*, 65:262 – 273.

[Singapore Energy Market Authority2011] Singapore Energy Market Authority. 2011. Handbook for solar photovoltaic (pv) systems. `<http://www.ema.gov.sg/images/files/EMA%20Solar%20Handbook_Apr%202011.pdf>`, apr. (accessed 02.02.2012).

[Skartveit and Olseth1986] Skartveit, Arvid and Jan Asle Olseth. 1986. Modelling slope irradiance at high latitudes. *Solar Energy*, 36(4):333 – 344.

[Smola and Scholkopf2004] Smola, Alex J. and Bernhard Scholkopf. 2004. A tutorial on support vector regression. *Statistics and Computing*, 14(3):199–222, August.

[SPE2015] SPE. 2015. Solarpower europe. `<http://www.solarpowereurope.org>`. (accessed 01.07.2015).

[Temps and Coulson1977] Temps, R. C. and K. L. Coulson. 1977. Solar radiation incident upon slopes of different orientations. *Solar Energy*, 19(2):179 – 184.

[Tian et al.2001] Tian, Y.Q., R.J. Davies-Colley, P. Gong, and B.W. Thorrold. 2001. Estimating solar radiation on slopes of arbitrary aspect. *Agricultural and Forest Meteorology*, 109(1):67 – 74.

[Voyant et al.2014] Voyant, Cyril, Christophe Darras, Marc Muselli, Christophe Paoli, Marie-Laure Nivet, and Philippe Poggi. 2014.

Bayesian rules and stochastic models for high accuracy prediction of solar radiation. *Applied Energy*, 114:218 – 226.

[Wasserman2003] Wasserman, Larry. 2003. *All of Statistics: A Concise Course in Statistical Inference (Springer Texts in Statistics)*. Springer, December.

[West et al.2014] West, Samuel R., Daniel Rowe, Saad Sayeef, and Adam Berry. 2014. Short-term irradiance forecasting using skycams: Motivation and development. *Solar Energy*, 110:188 – 207.

[Winters1960] Winters, P. R. 1960. Forecasting sales by exponentially weighted moving averages. *Management Science*, 6:324–342.

[World Radiation Centre (WRC)2014] World Radiation Centre (WRC). 2014. Solar constant. `<http://www.pmodwrc.ch/pmod.php?topic=tsi/composite/SolarConstant>`. (accessed 01.08.2015).

[Wu and Chan2011] Wu, Ji and Chee Keong Chan. 2011. Prediction of hourly solar radiation using a novel hybrid model of arma and tdnn. *Solar Energy*, 85:808–817.

[Yang et al.2013] Yang, Dazhi, Chaojun Gu, Zibo Dong, Panida Jirutitijaroen, Nan Chen, and Wilfred M. Walsh. 2013. Solar irradiance forecasting using spatial-temporal covariance structures and time-forward kriging. *Renewable Energy*, 60(0):235 – 245.

[Yang, Jirutitijaroen, and Walsh2012a] Yang, Dazhi, Panida Jirutitijaroen, and Wilfred M. Walsh. 2012a. Hourly solar irradiance time series forecasting using cloud cover index. *Solar Energy*, 86(12):3531 – 3543. <ce:title>Solar Resources</ce:title>.

[Yang, Jirutitijaroen, and Walsh2012b] Yang, Dazhi, Panida Jirutitijaroen, and Wilfred M. Walsh. 2012b. Hourly solar irradiance time series forecasting using cloud cover index. *Solar Energy*, 86(12):3531 – 3543.

[Yang et al.2013] Yang, Dazhi, Wilfred M. Walsh, Zibo Dong, Panida Jirutitijaroen, and Thomas G. Reindl. 2013. Block matching algorithms: Their applications and limitations in solar irradiance forecasting. *Energy Procedia*, 33:335–342.

[Yang et al.2014] Yang, Handa, Ben Kurtz, Dung Nguyen, Bryan Urquhart, Chi Wai Chow, Mohamed Ghonima, and Jan Kleissl. 2014. Solar irradiance forecasting using a ground-based sky imager developed at {UC} san diego. *Solar Energy*, 103:502 – 524.

[Yann LeCun and Hinton2015] Yann LeCun, Yoshua Bengio and Geoffrey Hinton. 2015. Deep learning. *Nature*, 521:436–444.

[Zhang2006] Zhang, Qingyuan. 2006. Development of the typical meteorological database for chinese locations. *Energy and Buildings*, 38(11):1320 – 1326.

Appendix A

Transposition Models

A.1 Isotropic Models

Four isotropic models are accessed in this work. In isotropic approximation, we assume the diffuse radiance were ideally constant over the whole sky hemisphere. Tilt angle s is the only input to these models.

A.1.1 Badescu

$$R_{\mathrm{d}} = [3 + \cos(2s)]/4 \tag{A.1}$$

A.1.2 Koronakis

$$R_{\mathrm{d}} = (2 + \cos s)/3 \tag{A.2}$$

A.1.3 Liu and Jordan

$$R_{\mathrm{d}} = (1 + \cos s)/2 = \cos^2(s/2) \tag{A.3}$$

A.1.4 Tian

$$R_{\mathrm{d}} = 1 - s/180 \tag{A.4}$$

A.2 Anisotropic Models

In reality, a plane of tilt s facing the sun receives more diffuse radiation than a plane of same tilt in the opposite direction. Various parameters such as irradiance components and zenith angle are considered in the models.

A.2.1 Hay

$$R_{\mathrm{d}} = \frac{I_{\mathrm{Dif}}}{I_{\mathrm{oh}}} R_{\mathrm{b}} + \left(1 - \frac{I_{\mathrm{Dif}}}{I_{\mathrm{oh}}}\right) [(1 + \cos s)/2] \tag{A.5}$$

where R_{b} is beam irradiance transposition factor, it is given by $\cos\theta/\cos Z$.

A.2.2 Klucher

$$R_{\mathrm{d}} = \cos^2(s/2)[1 + F' \sin^3(s/2)][1 + F' \cos^2\theta \sin^3 Z] \tag{A.6}$$

where F' is Klucher's modulating function defined as $(1 - I_{\mathrm{Dif}}/I_{\mathrm{Glo}})$.

A.2.3 Perez

The sky's clearness ε is first defined by Perez:

$$\varepsilon = \left[\left(I_{\mathrm{Dif}} + I_{\mathrm{Dir}} \frac{\cos Z}{\cos\theta}\right) \frac{1}{I_{\mathrm{Dif}}} + \kappa \left(\frac{Z \times \pi}{180}\right)^3\right] \div \left[1 + \kappa \left(\frac{Z \times \pi}{180}\right)^3\right] \tag{A.7}$$

where κ is constant 1.041 for Z in degrees. The sky's brightness Δ is give by:

$$\Delta = I_{\mathrm{Dif}} \times AM/I_{\mathrm{o}} \tag{A.8}$$

The circumsolar brightening coefficient F_1 and horizon brightening coefficient F_2 is given by:

$$F_1 = F_{11} + F_{12} \times \Delta + F_{13} \times \left(\frac{Z \times \pi}{180}\right) \tag{A.9}$$

$$F_2 = F_{21} + F_{22} \times \Delta + F_{23} \times \left(\frac{Z \times \pi}{180}\right) \tag{A.10}$$

where F_{11}, F_{12}, F_{13}, F_{21}, F_{22} and F_{23} are given according to various ε bins by table:

ε	F_{11}	F_{12}	F_{13}	F_{21}	F_{22}	F_{23}
$[1, 1.065)$	-0.0083	0.5877	-0.0621	-0.0596	0.0721	-0.022
$[1.065, 1.23)$	0.1299	0.6826	-0.1514	-0.0189	0.066	-0.0289
$[1.23, 1.5)$	0.3297	0.4869	-0.2211	0.0554	-0.064	-0.0261
$[1.5, 1.95)$	0.5682	0.1875	-0.2951	0.1089	-0.1519	-0.014
$[1.95, 2.8)$	0.873	-0.392	-0.3616	0.2256	-0.462	0.0012
$[2.8, 4.5)$	1.1326	-1.2367	-0.4118	0.2878	-0.823	0.0559
$[4.5, 6.2)$	1.0602	-1.5999	-0.3589	0.2642	-1.1272	0.1311
$[6.2, +\infty)$	0.6777	-0.3273	-0.2504	0.1516	-1.3765	0.2506

Finally the diffuse transposition factor is given by:

$$R_{\mathrm{d}} = (1 - F_1) \times (1 + \cos s)/2 + F_1 \times a/b + F_2 \times \sin s \tag{A.11}$$

where $a = \max(0, \cos\theta)$ and $b = \max(0.087, \cos Z)$.

A.2.4 Reindl Transposition Model

$$R_{\mathrm{d}} = \frac{I_{\mathrm{Dif}}}{I_{\mathrm{oh}}} R_{\mathrm{b}} + \left(1 - \frac{I_{\mathrm{Dif}}}{I_{\mathrm{oh}}}\right) [(1 + \cos s)/2] \left[1 + \sqrt{\frac{I_{\mathrm{Dif}}}{I_{\mathrm{Glo}}}} \sin^3(s/2)\right] \tag{A.12}$$

where R_{b} is defined earlier in Hay model.

A.2.5 Skartveit and Olseth

$$R_\mathrm{d} = \frac{I_\mathrm{Dif}}{I_\mathrm{oh}} R_\mathrm{b} + \Omega \cos s + \left(1 - \frac{I_\mathrm{Dif}}{I_\mathrm{oh}} - \Omega\right) [(1 + \cos s)/2] \tag{A.13}$$

where $\Omega = \max\,[0, (0.3 - 2I_\mathrm{Dif}/I_\mathrm{oh})]$

A.2.6 Temps and Coulson

$$R_\mathrm{d} = \cos^2(s/2)[1 + \sin^3(s/2)][1 + \cos^2\theta \sin^3 Z] \tag{A.14}$$

Appendix B

Empirical Models to Relate Various Transmittance

B.1 Erbs Model

We define diffuse horizontal transmittance K_{d} as:

$$I_{\mathrm{Dif}} = K_{\mathrm{d}} I_{\mathrm{oh}} \tag{B.1}$$

Combine the above equation with Equation (6.28) to (6.32), we have:

$$K_{\mathrm{d}} = K_{\mathrm{t}} - K_{\mathrm{n}} \tag{B.2}$$

together with the correlation which Erbs developed in reference (Erbs, Klein, and Duffie, 1982; **?**):

$$\begin{aligned}
\frac{K_{\mathrm{d}}}{K_{\mathrm{t}}} &= 1.0 - 0.09 K_{\mathrm{t}} \ \text{ for } \ K_{\mathrm{t}} \leq 0.22 && \text{(B.3)} \\
\frac{K_{\mathrm{d}}}{K_{\mathrm{t}}} &= 0.9511 - 0.1604 K_{\mathrm{t}} + 4.388 K_{\mathrm{t}}^2 - 16.638 K_{\mathrm{t}}^3 \\
&\quad +12.336 K_{\mathrm{t}}^4 \ \text{ for } \ 0.22 < K_{\mathrm{t}} \leq 0.80 && \text{(B.4)} \\
\frac{K_{\mathrm{d}}}{K_{\mathrm{t}}} &= 0.165 \ \text{ for } \ K_{\mathrm{t}} > 0.80 && \text{(B.5)}
\end{aligned}$$

B.2 Orgill Model

$$\frac{K_{\mathrm{d}}}{K_{\mathrm{t}}} = 1.0 - 0.249K_{\mathrm{t}} \ \text{ for } \ K_{\mathrm{t}} \leq 0.35 \tag{B.6}$$

$$\frac{K_{\mathrm{d}}}{K_{\mathrm{t}}} = 1.557 - 1.84K_{\mathrm{t}} \ \text{ for } \ 0.35 < K_{\mathrm{t}} \leq 0.75 \tag{B.7}$$

$$\frac{K_{\mathrm{d}}}{K_{\mathrm{t}}} = 0.177 \ \text{ for } \ K_{\mathrm{t}} > 0.75 \tag{B.8}$$

B.3 Maxwell Model

$$K_{\mathrm{n}} = K_{\mathrm{nc}} - \Delta K_{\mathrm{n}} \tag{B.9}$$

$$\begin{aligned} K_{\mathrm{nc}} &= 0.866 - 0.122(AM) - 0.0121(AM)^2 \\ &\quad -0.000653(AM)^3 + 0.000014(AM)^4 \end{aligned} \tag{B.10}$$

$$\Delta K_{\mathrm{n}} = a + b \times \exp\left[c \times (AM)\right] \tag{B.11}$$

$$AM = [\cos Z + 0.15(93.885 - Z)^{-1.253}]^{-1} \tag{B.12}$$

K_{nc} is clear-sky direct normal transmittance, AM is air mass. a, b and c are parameters used to calculate the change in direct normal transmittance ΔK_{n} under various values of K_{t}. a, b and c are related to K_{t} by a piecewise function:

For $K_{\mathrm{t}} \leq 0.6$,

$$a = 0.512 - 1.56K_{\mathrm{t}} + 2.286K_{\mathrm{t}}^2 - 2.222K_{\mathrm{t}}^3 \tag{B.13}$$

$$b = 0.370 + 0.962K_{\mathrm{t}} \tag{B.14}$$

$$c = -0.280 + 0.932K_{\mathrm{t}} - 2.048K_{\mathrm{t}}^2 \tag{B.15}$$

For $K_{\mathrm{t}} > 0.6$,

$$a = -5.743 + 21.77K_{\mathrm{t}} - 27.49K_{\mathrm{t}}^2 + 11.56K_{\mathrm{t}}^3 \tag{B.16}$$

$$b = 41.40 - 118.5K_{\mathrm{t}} - 66.05K_{\mathrm{t}}^2 + 31.90K_{\mathrm{t}}^3 \tag{B.17}$$

$$c = -47.01 + 184.2K_{\mathrm{t}} - 222.0K_{\mathrm{t}}^2 + 73.81K_{\mathrm{t}}^3 \tag{B.18}$$

B.4 Reindl Model (Univariate)

$$\frac{K_\mathrm{d}}{K_\mathrm{t}} = 1.020 - 0.248 K_\mathrm{t} \ \text{ for } \ K_\mathrm{t} \leq 0.3 \tag{B.19}$$

$$\frac{K_\mathrm{d}}{K_\mathrm{t}} = 1.45 - 1.67 K_\mathrm{t} \ \text{ for } \ 0.3 < K_\mathrm{t} \leq 0.78 \tag{B.20}$$

$$\frac{K_\mathrm{d}}{K_\mathrm{t}} = 0.147 \ \text{ for } \ K_\mathrm{t} > 0.78 \tag{B.21}$$

B.5 Reindl Model (Bivariate)

$$\begin{aligned} \frac{K_\mathrm{d}}{K_\mathrm{t}} &= 1.020 - 0.254 K_\mathrm{t} + 0.0123 \sin(\alpha) \\ &\quad \text{for } \ K_\mathrm{t} \leq 0.3 \end{aligned} \tag{B.22}$$

$$\begin{aligned} \frac{K_\mathrm{d}}{K_\mathrm{t}} &= 1.400 - 1.749 K_\mathrm{t} + 0.177 \sin(\alpha) \\ &\quad \text{for } \ 0.3 < K_\mathrm{t} \leq 0.78, \\ &K_\mathrm{d}/K_\mathrm{t} < 0.97 \ \text{ and } \ K_\mathrm{d}/K_\mathrm{t} > 0.1 \end{aligned} \tag{B.23}$$

$$\begin{aligned} \frac{K_\mathrm{d}}{K_\mathrm{t}} &= 0.486 K_\mathrm{t} - 0.182 \sin(\alpha) \\ &\quad \text{for } \ K_\mathrm{t} > 0.78 \ \text{ and } \ K_\mathrm{d}/K_\mathrm{t} > 0.1 \end{aligned} \tag{B.24}$$

where α is the solar elevation angle. It is given by $90° - Z$ in degrees.